University of Ninevah
College of Electronics
Electronic Department

Modeling and Electrical Characterization of Tandem Solar Cells

Noor Alhuda Saad Abbas Al-Jamaas

A Thesis in
Electronic Engineering
(Solid State)

Supervised by

Dr. Qais Thanon Algwari

1442 AH 2020 AD

Modeling and Electrical Characterization of Tandem Solar Cells

A Thesis Submitted by

Noor Alhuda Saad Abbas Al-Jamaas

To
The Council of the College of Electronics Engineering
University of Ninevah
As a Partial Fulfillment of the Requirements
For the Degree of Master of Science
In
Electronic Engineering
(Solid State)

Supervised by

Dr. Qais Thanon Algwari

1442 AH **2020 AD**

ACKNOWLEDGEMENTS

First and foremost, I am grateful to Allah, the most gracious and compassionate, for helping me to make my dream come true, by giving me strength and patience to overcome all the handicaps that faced my journey of studying, and without Almighty Allah blessing I could never achieve my goal.

I would like from the depths of my soul and heart to thank Professor Dr. Qais Thanon, my respected supervisor, for the unconditional guidance and inspiration that he granted me, for his genuine assistance and precious information and for his great support that helped me to finish this work. He was the one who keep on encouraging me, giving me hope and faith whenever I become disappointed, and made me strongly trusted in my abilities. I also appreciate his efforts that he spent for reviewing the draft version of this dissertation.

I gratefully acknowledge the support of the Electronics Engineering College and especially the Electronic department and I would also like to thank all my teachers and friends who have supported me through the years of study.

I would like to dedicate this dissertation to my sincere, generous, and great father and to my kind, loving, and wonderful mother, who encouraged and assisted me at each and every stage of my life and longed to see this achievement come true. I am indebted to my parents and my beloved brothers for their moral support throughout my studying. I am truly grateful to my husband and my mother in law for supporting me during this period. Without their amazing support and love, I would not have achieved the goals and I am so pleased to dedicate this work to them.

Special thanks for my daughter Shams and my son Ahmed for being in my life.

I would like to dedicate this work to my family, my teachers, and my friends. I appreciate your love, kindness, support, and generosity.

ABSTRACT

In this study, an identified analysis was carried on a 3C-SiC PIN thin-film solar cell. This cell is constructed from Al-doped p-(3C-SiC) as the absorber layer with a band gap of 1.454 eV, un-doped i-(3C-SiC) with a band gap of 2.39 eV. A double n-layers as the buffer which consists of n layer of 3C-SiC and a layer of Cr-doped n-3C-SiC with band gaps of (2.39 and 1.139 eV) respectively, and a window layer of SnO_2 material with 3.6 eV band gap was used as anti-reflecting material.

The study was accomplished by using the computer simulation software SCAPS-1D. This software is designed to simulate and study the properties of thin-film solar cells.

A parametric study was achieved on the reference cell, which based on initial values of the cell parameters (doping density and thickness) for each layer of the cell. The initial carrier concentration values are: for the p-Al (3C-SiC) is $N_a=10^{13}$ cm^{-3}, for n-Cr (3C-SiC) is $N_d=10^{13}cm^{-3}$, for n^+(3C-SiC) is $N_d=10^{19}$ cm^{-3}, for n-(SnO_2) is $N_d=10^{12}$ cm^{-3}, and intrinsic carrier concentration of 10^{10} cm^{-3} for the i-(3C-SiC). The initial thickness values are (1, 1, 0.05, 0.05, and 0.1 μm) for the layers: p-Al (3C-SiC), i-(3C-SiC), n-Cr (3C-SiC), n^+ (3C-SiC), and n-(SnO_2) respectively. The output parameters of the reference cell were: (V_{OC} = 0.2524 V, J_{SC}=34.66 mA.cm^{-2}, FF = 41.21% and η = 3.61%).

The impact of the carrier concentration of each layer on the performance of the reference cell was investigated. It was proved that the efficiency of the reference cell was increased from 0.87 to 18.73 % when the doping density of the absorber layer changed from 10^{10} to 10^{15} cm^{-3}, also the efficiency of the cell increases from 16.84 to 21.52% as the carrier concentration in the buffer n^+ layer increases from 10^{18} to 10^{22} cm^{-3}. On the other hand increasing the carrier concentration in the n-Cr (3C-SiC) buffer layer from 10^{13} to 10^{15} cm^{-3} does not effect on the efficiency

of the cell, due to the sever recombination in the interface that occurred because of the donors are less than the acceptors. Thus, additional increment in the doping density was made in this layer up to 10^{19} cm^{-3} and the cell efficiency was increased from 21.44 to 22.69 %. The carrier concentration variation in the i-(3C-SiC) and the SnO_2 layer does not have a high impact on cell performance and the optimum carrier concentration for the i-(3C-SiC) is 10^{15} cm^{-3} and for the SnO_2 is $N_d=10^{18}$ cm^{-3} that produce a power conversion efficiency of 22.78 %.

The second part of the study was performed on the thickness of the cell layers, the thickness of the absorber was changed from 1 to 3 µm and the efficiency was increased from 22.78 to 24.14 %, and this results from the increment in the collection of photo-generated carriers before recombination. The thickness of the intrinsic layer was changed from 1 to 2.5 µm which increases the efficiency of the cell from 24.14 to 34.45%, and this ensures the significant role of the intrinsic layer thickness on the performance of the cell. Increasing the thickness of the window layer from 0.1 to 0.2 µm reduces the efficiency of the cell from 34.45 to 31.93 %, also increasing the n^+ layer thickness from 0.05 to 0.1 µm degrades the efficiency from 31.93 to 30.32 %. However, increasing the thickness of these layers has a beneficial effect in reducing the high value of the short-circuit current of the cell from 54.27 to 47.69 $mA.cm^{-2}$. On the other hand changing the thickness of the n-Cr (3C-SiC) layer does not have a noticeable effect on cell performance. Thus taking a thin layer of 100 nm is better to reduce the cell resistance, which produces a power conversion efficiency of 30.27 %.

Also the present study examined the impact of the main environmental conditions (Illumination and Temperature) on the optimum structure. It was proved that the produced current of the PV cells is proportion directly to the illumination, as the intensity of the light increases from 250 to 1200 $W.m^{-2}$ the short-circuit current increases from 11.924 to 57.149 $mA.cm^{-2}$ due to higher absorption of photons which increases the carrier generation and therefore a J_{SC}. It was noticed that the efficiency of the cell reduced with higher irradiation intensity (I_o>500 $W.m^{-2}$) from 30.34 to 30.20 %, due to the effect of the high series resistance. The temperature effect on the optimum cell was studied, it was found that as the temperature increases from 300 to 400 K the open-circuit voltage reduces from 0.768 to 0.516 V, which leads to a reduction in the efficiency of the cell from 30.27 to 18.10 %. V_{OC} considerably decreases due to the decrement in current of saturation that reduces directly with an increase in temperature.

The obtained results are discussed and conclusions have been given, suggestions are given for further work in this field.

Contents

List of tables

List of Figures

LIST OF ABBREVIATIONS

ABBREVIATION	DESCRIPTION
A	Area
AC	Alternating current
Al	Aluminum
AM	Air Mass
a-Si	Amorphous Silicon
BSF	Back Surface Field
CB	Conduction Band
C-F	Capacitance Frequency Characteristics
CHCC	Electron from the CB recombine with a hole from the VB and the result is an exited electron remains in the CB
CHHH	Electron from the CB recombine with a hole from the VB and the result is an exited hole remains in the VB
Cr	Chromium
C-Si	Crystalline Silicon
C-V	Capacitance Voltage Characteristics
DBR	Distributed Bragg reflector
DC	Direct Current
DH	Double Hetero
EHP	Electron Hole Pairs
HJ-IBC	Heterojunction Interdigitated Back Contact
HP	High Performance
IB	Inter mediate Band
IBC	Interdigitated Back Contact
IR	Infra Red

J-V	Current Density-Voltage Characteristics
Mc-Si	Micro crystalline silicon
MJ SCs	Multi-Junction Solar Cells
MS	Mechanically Stacked
PL	Photo-Luminescence (PL)
POLO	polycrystalline silicon (poly-Si) on oxide
PV	Photovoltaic
SCAPS-1D	Solar Cell Capacitance Simulator-One Dimension
SiC	Silicon Carbide
SRH	Shockley Red-Hall
TCO	Transparent Conducting Oxide
UV	Ultra Violet
VB	Valance Band

LIST OF SYMBOLS

SYMBOL	DESCRIPTION
C	Speed of light in the Vacuum
C_{dep}	Depletion region’s capacitance
D_n	Electron’s Diffusion Coefficient
D_p	Hole’s Diffusion Coefficient
E	Electric Field Intensity
E_c	Conduction Band
E_{fn}	Fermi Level of n-type
E_{fp}	Fermi Level of p-type
E_i	Fermi Level of intrinsic semiconductor
E_m	Maximum Electric Field at the Junction
EQE	External Quantum Efficiency
eV	Electron Volt
E_v	Valence Band
FF%	Fill Factor
G	Generation Rate
g(x)	The function of generation
h	Blank’s Constant
hv	Optical Power
$I_0^{\prime}$	Intensity of the Light
I_0	Reverse Saturation Current
I_{ph}	Photo Generated Current
IQE	Internal Quantum Efficiency
J	Current Density
J_0	Reverse Saturation Current Density
J_n	Total Electrons Current Density
$J_{n/diff}$	Electrons Current Density Resulting from Diffusion

$J_{n/drift}$	Electrons Current Density Resulting from Drift
J_p	Total Holes Current Density
$J_{p/diff}$	Holes Current Density Resulting from Diffusion
$J_{p/drift}$	Holes Current Density Resulting from Drift
J_{SC}	Short Circuit Current Density
K	Boltizman coefficient
n	Concentration of Electrons at no Equilibrium
ń	Diode Ideality Factor
N_a	Concentration of Acceptors Atoms
N_c	Density of States in the Conduction Band
N_d	Concentration of Donor Atoms
n_o	Concentration of the Electrons at thermal Equilibrium
N_v	Density of States in the Valence Band
p	Concentration of Holes ay No-Equilibrium
P_{in}	Power of the Incident Light at the Surface of the Solar Cell
P_m	Maximum Power Output from the Solar Cell
p_o	Concentration of the Holes at thermal Equilibrium
q	Electron Charge
QE	The Quantum Efficiency
R	Recombination Rate at no Equilibrium
R_S	Series Resistance
R_{Sh}	Shunt Resistance
V_a	Applied Voltage
V_{bi}	Built in Potential
V_{OC}	Open Circuit Voltage
V_R	Reverse Applied Voltage
V_{th}	Thermal Velocity
W	Space Charge Region Width

X_l	The Length of the SCR Extended to the n-Type Region
X_r	The Length of the SCR Extended to the p-Type Region
α	Absorption Coefficient
ε	Permittivity
$\eta\%$	efficiency
θ	The Angle of the Incident Light
λ_c	Cut off Wavelength
μ_n	Electron’s Mobility
μ_p	Hole’s Mobility
υ	Optical Frequency
υ_d	Drift Velocity
ψ	Electrostatic Potential
Φ_m	Metal Work Function

CHAPTER ONE
INTRODUCTION AND LITERATURE REVIEW

1.1 INTRODUCTION

The need for renewable energy to overcome CO_2 emissions and avoid the use of conventional energy fossil fuels such as coal and petroleum is increasing nowadays. Besides that, these resources are environmentally harmful to human beings, and will be exhausted within the next century as well, the advancement of the use of other energy supplies is vital [1]. The development of renewable energy sources such as solar, geothermal or wind energy and the desire for a healthy environment have attracted researchers to look for alternative renewable energy conversion devices [2]. Innovative solutions to more efficient sunlight incident photon extraction are the most effective option to meet world demand for clean energy. One significant method of converting solar energy into electricity is through the photovoltaic effect that was discovered by the French physicist Becquerel in 1839 [3], it is generally defined as the creation of an electrical voltage between two electrodes attached to a liquid or solid system when the light is shining on the system. Basically, all photovoltaic devices contain a PN junction that generates the photo-voltage directly, these apparatuses are also known as solar cells [4]. Adams and Day, in 1877, described the effect in much more detail. They noticed that selenium electrodes were exposed to radiation and produced an electrical voltage [5], enabling them to generate current. The effect was then postponed till transistors were discovered and Shockley [6] explained the physics of the PN junction and Bardeen and Brattain [7] in 1949, that year marked the start of a semiconductor era. Then, in 1954, Chapin et a1[8] established the very first crystalline silicon-based solar cell at the bell labs in the United States of America, that had an efficiency of 6%, which was considerable at that time. Within a few years, this efficiency has been increased to 10 %. The first workable use of solar cells was in the supply of satellite power. Photovoltaics is demonstrated to be persuasive in this application. The early problem of high-efficiency degradation by cosmic radiation has now largely been resolved [9]. Figure (1.1) shows the Cross-section of a typical solar cell [10]. In addition to silicon, which is now used almost exclusively for the generation of solar systems, investigations have been carried out in numerous institutions into other semiconductor materials. They were effective in the growth of amorphous silicon (a-Si)-silicon hydrogen compound [11]. This material conquered the global market (e.g. clocks, pocket calculators).

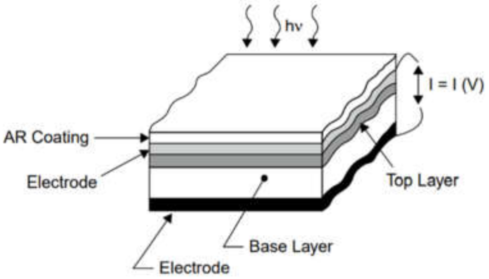

Fig. (1.1) Cross-section of a typical solar cell [10].

Copper-Indium-Diselenide (CIS) has been at the forefront of all the other materials made of III-V or II-VI semiconductors or hetero-compounds [12]. The main benefit of this material is the adequate long-term stability of solar cell parameters and the accomplishment of a relatively high degree of productivity. Such-called tandem cells represent a further sphere of work in which solar cells with different absorption ranges are optically connected in series to make better use of the solar spectrum [9]. In the early 1980s, it was recognized that improved performance in solar cells was of high significance for the reducing costs of the entire system. From this point on, research and development have largely focused on achieving high levels of efficiency.

1.2 SEMICONDUCTOR MATERIALS USED FOR SOLAR CELLS

In utilized solar cells presently, photon absorption, that outcomes in the generation of charge carriers, and photo-generated charge carriers, separation occurs in semiconductor materials. Consequently, the most important parts of the solar cell are the semiconductor layers; they establish the heart of the solar cells. There are several semiconductor materials appropriate for the transformation of photon energy into electrical energy, and each has advantages and drawbacks [13].

The most common, highly used and the first successful solar cell was C-Si. The major factors that can be used to determine the design and performance of the cell are [14]:

- Concentration levels of doping atoms that decide the width of the space-charge region of the junction.
- Mobility and diffusion coefficient (μ, D) of the carriers that describe the transport of the carriers due to drift and diffusion.
- Lifetime, τ and diffusion length, L, of the excess carrier that defines the process of generation-recombination.
- Band-gap energy, E_g, absorption coefficient, α, and refractive index, n, which describes the ability of the semiconductor to absorb visible and other radiations.

Up to date, developed PV cells can be grouped into four types called generations according to the materials used [15]:

1. First-generation: It is based on both mono and polycrystalline silicon technologies.
2. Second-generation: includes the amorphous silicon (a-Si) and microcrystalline silicon (c-Si) thin films solar cells, cadmium

telluride/cadmium sulfide (CdTe/CdS) and copper indium gallium selenide (CIGS) solar cells.

3. Third-generation: involves technologies that are based on new combinations including films of nanocrystalline, active quantum dots, tandem or stacked multilayers of inorganics based on III–V materials, such as GaAs/GaInP, organic (polymer)-based solar cells, dye-sensitized solar cells, etc.
4. Fourth-generation: that is known as “inorganics-in-organics”.

The following part shows the developments in the solar cells field of the commonly used materials for the recent years.

1.2.1 FIRST GENERATION SOLAR CELL:

Mono crystalline-Si

- In (2011) a tandem solar cell with 3-terminal Si-Si:Ge enhanced the long-wavelength light absorption to improve the power conversion efficiency [16].
- The effect of the spectral response on the monocrystalline-Silicon solar cell was studied in (2015). It was found that the external quantum efficiency increased with wavelength, reached the maximum at a wavelength of 590 nm [17].
- The photovoltaic parameters of mono crystalline-Si solar cell analyzed in (2015) by changing the cell temperature, (η) increased with cell temperature from (9.023%) to (11.417%) [18].
- In (2017) research made about front emitter with diffused boron and full-area passivating rear contact on n-type (high-performance multicrystalline silicon) HP mc silicon to have a high-efficiency of 21.9% [19].
- Within the year of (2018) a new corrugation architecture designed to allow ultra-flexible (140 mm bending radius) with high

performance (17.2 % efficiency) compared to rigid Interdigitated Back Contact (IBC) efficiency [20].

- Co-doped mono-Si PERC solar cells (passivated emitter and rear cell) are used to evaluate defect kinetics at high-levels of light intensity and varying temperatures during the year (2020) [21].

Polycrystalline-Si

- Module temperature impacted on the photovoltaic parameters was evaluated in (2015), for poly-crystalline silicon the maximum power reduced by 17 % with a rise in temperature from 15 to 60 ° C. The maximum current increased linearly with an increase in light intensity. [22].
- C-Si, $CH_3NH_3PbI_3$, and TiO_2 were used in Si-perovskite tandem solar cell, the highest recorded efficiency performance of 27.29 % was obtained in (2017) [23].
- POLO contacts were used in (2017) for both polarities and a 25.0% efficiency for silicon solar cells was recorded [24].
- An improvement in the efficiency up to 26.6% with 0.3% absolute (1.16% relative) from the previous recorded (26.3%) using HJ-IBC solar cell [25].
- New research in (2019), concluded that 27% efficiency is possible by using a surface passivation technology for c-Si by amorphous Si layer [26].
- The texturization performance of multi-crystalline silicon (mc-Si) wafers has been improved by adding MnO_2 particles to conventional wet acid etching. ($HF/HNO_3/H_2O$) system, for the AM1.5G sun spectrum in (2019) [27].

1.2.2 SECOND GENERATION SOLAR CELL:

Thin films solar cell

I. **CdTe (Cadmium Telluride)**

- A structure of CdTe-based solar cells was grown on commercial SnO_2: F/SnO_2 coated substrate using CdSe window layers had achieved a photocurrent enhancement. An efficiency of 15.2 % was recorded for this cell in 2015 [28].
- A V_2O_5 thin film buffer layer was used to form low-barrier back contact for the production of CdTe solar cells in 2016, with a relatively high efficiency of 14.0 % compared to CdTe solar cells with a traditional Cu/Au back electrode [29].
- A heterojunction of CdS/CdTe solar cell with ZnTe BSF layer was analyzed with a recorded conversion efficiency of (24.66%) in 2017 which was increased about 4.03% in comparison with the reference cell (16.42%) [30].
- The ZnO transparent buffer layer directly impacted on the performance of CdZnS solar cells in 2019 has achieved up to 1.8 % improvement in conversion efficiency compared to the corresponding devices without the ZnO buffer layer [31].
- The impact on the photoelectric conversion efficiency of the window layer CdTe solar cell band-gap and the conduction band offset between the window layer CdTe could have a significant effect, over 18 % CdTe conversion efficiency could be achieved for high-quality ZMO films with extremely low donor densities [32].
- CdTe thin films and CdS/CdTe heterojunctions have been deposited on glass substrates with various technological parameters using PVD thermal evaporation technique. The optimum thickness of the CdS layer for the best CdS/CdTe heterojunction efficiency

values of 15.8 % was configured for simulation of optical parameters in the SCAPS software in the year of 2019 [33].

- Effective materials are chosen in the CdT solar cell (in 2019) for each layer after the comparison of various materials to improve cell performance, TiO_2 was the preferred design for the window layer and ZnS was the main formula for the buffer layer. Also, the BSF made of ZnSe and multiple DBR layers made of Si/Al_2O_3 are added to the final refined cell to further improve the efficiency: η=23.94% [34].

II. **CIGS (Copper Indium Gallium Diselenide**)

- The performance of a double junction CGS/CIGS tandem solar cell with the CGS as top-cell and the GIGS as bottom-cell was enhanced, and a power-conversion efficiency of 25.11% was achieved in 2015 [35].
- The CdS buffer layer is substituted by other materials such as Zinc Sulphide (ZnS) and Zinc Selenide (ZnSe), ZnS could be used as an alternative material to CdS by changing the thickness of the absorber layer (and buffer layer) and the defect density of the p-CIGS layer and the n-ZnS layer. The optimized solar cell has an efficiency of more than 22 % under the AM1.5 G spectrum and one sun [36].
- Glass-ceramics using industrial waste have been established, proving that they are appropriate as a membrane for CIGS thin-film solar cells. The method allows both usability and energy savings during the production process [37].
- CIGS thin-film solar cell utilizing Molybdenum as back contact had an optimal conversion efficiency of 21.35 % to 24.21 % with slimmer absorber thickness at an energy band-gap of 1.15 eV and doping concentration of about 10^{17} cm^{-3}. Moreover, the thickness

of CdS buffer layer should be greater than 40 nm and less than 60 nm to maintain the remarkable overall solar cell performance [38].

- High performance of the ultra-thin CIGS solar cell was assessed at the year 2020 using the band-gap grading and the Au plasmonic nanoparticle array, a remarkable increment in cell efficiency of around 19 % [39].

1.2.3 THIRD GENERATION SOLAR CELL:

III–V Technique

- In the year of 2003, a 3-junction solar cells InGaP/InGaAs/Ge with a new recording efficiency of 31.7 % at AM1.5 (1-sun) have been achieved using Ge substrates by the advancement of the lattice-matching and AlGaAs/InGaP DH tunnel structure junction with the AlInP barriers. InGaP/GaAs/InGaAs MS 3-junction cells with world-record efficiency of 33.3 % were also manufactured [40].
- Efficiency of 40.7 % has been evaluated and independently verified in 2007 for a metamorphic three-junction GaInP/GaInAs/Ge cell under the standard spectrum for terrestrial concentrator solar cells at 240 suns [41].
- A multi-junction cell with visible and IR wavelength absorption abilities is proposed in 2011. The suggested structured cell is a 1cm^2 cell and consists of two sub-cells: the bottom unit is a 20-period GaAs-Ge super lattice embedded in a GaAs/Ge bulk solar cell. At the top of this cell, the AlAs/AlGaAs/GaAs cell is proposed, suitable for short wavelengths. Both parts are linked in series through a standard tunnel junction, collection efficiency is predicted to surpass the current threshold of 42 % (one sun conditions) [42].

- An InGaP/GaAs/InGaAs inverted triple-junction solar cells have been developed at the year of 2013 for a concentrator application with an efficiency of more than 37% [43].
- The InGaAsN (Sb) PIN junction structure is developed in 2016 to improve the power conversion efficiency of the germanium-based 4J solar cell, The performance of the subcell is modeled using drift-diffusion simulations using cross light Apsys [44].
- The MJSCs are modeled and implemented using the TCAD SILVACO tool in 2018. InGaP/GaAs/Ge and InGaP/GaAs/InGaAs TJ solar cells are evaluated and the results acquired are compared. The efficiency of the optimized InGaP/GaAs/Ge TJ solar cell is 39.61%, compared to 42.01% for the proposed InGaP/GaAs/InGaAs cell [45].

- The photovoltaic behavior of p-InGaN/n-InGaN single-junction solar cells has been studied numerically (2019). The simulation is performed using the SCAPS (Solar Cell Capacity Simulator) software. The ideal conversion efficiency of 15.32 % was confirmed at a band-gap of 1.32 eV corresponding to 64 % of the Indium compositions [46].

1.3 LITERATURE REVIEW

The very first silicon solar cell has been confirmed in 1941 by Russel S. Ohl [47], The objective of the study was to provide an improved light-sensitive electrical device. The Photo-E. M. F cell consists of a part of the silicon ingot that is supplied with conductive terminals, which had an energy conversion rate of less than 1%.

Many improvements have been made in silicon solar cell performance. Standardization of past measurements shows there has been a 42% improvement between 1983 and 1991 [48].

In recent years, more attempts have been devoted to enhance the efficiencies of silicon solar cells, such as interdigitated back contact crystalline silicon solar cells at 2015 by Hele Savina [49]. A conformal aluminum film solved the problem of surface recombination in black silicon solar cells by offering great chemical and electrical passivation. Efficiencies above 22 % could be achieved even in thick interdigitated back-contacted cells [49].

In 2017, industrially suitable processes were used by K. Yoshikawa et al [50] for the manufacture of large-area silicon solar cells incorporating interdigitated back contact and amorphous silicon/crystalline heterojunction. The efficiency was more than 26 % that is an enhancement of 2.7 % compared to the previous record rate of 25.6 %.

Light trapping technique is very significant for improving the performance of solar cells. This technique was confirmed by Dennis M. Callahan, J. N. Munday, and H. A. Atwater in 2012 [51]. The best approach to surpassing the standard ray optic or so-called ergodic light trapping constrain is to construct an increased local optical state density (LDOS) for the absorber [51]. In the same field another achievement by H. Heidarzadeh and three others in 2015 [52] showed that the simulation results of a 50 μm cell with a surface pyramid length of about 10 μm provides an efficiency of more than 24 %. Also, a backside filter analysis showed that it is possible to have a high efficiency cell with a thickness of less than 10 μm.

Plasmonic concepts is another technique that improves the efficiency. R. khan and others showed in the year of 2017 [53] that absorption can be improved by the embodiment of metal nano particles into the structure of the cell. Another study at the same year proved that light trapping of textured silicon solar cell based on light scattering and angle of incident light of plasmonics indium nanoparticles (In NPs) [54].

Perovskite solar cell is among the new types of solar cells which have lately been regarded because of its distinctive properties, such as high conversion efficiency, comfortable construction and low cost such what was achieved by M. Liu in 2013 [55] and H. Heidarzadeh in 2018 [56].

On the other hand wide band-gap semiconductors have advanced electrical characteristics compared to silicon (Si) that helps to overcome the limitations that occurs due to using silicon, the 3C-SiC has specific important advantages that make it extremely desirable, the major benefit of the cubic SiC polytype is the lower cost of manufacturing [57].

Initially pioneering work in SiC as a semiconductor material could be ascribed to Marconi in 1907 [58]. An early attempt to use 3C-SiC for enhanced boron doping carrier generation was described in 2003 by B. S. Richards, but the composite material of 3C-SiC was not adequate at that period [59].

In 2011 structural stability, together with the electronic and optical properties of 3C-SiC and Ni-doped 3C-SiC, have been analyzed by Y. Dou [60]. Some new energy levels of impurity occur in the Ni-doped 3C-SiC band-gap that could enhance the conductivity of 3C-SiC, Doping with Ni can increase the efficiency of 3C-SiC photo-absorption.

The 3C-SiC/Si tandem solar cell was investigated in 2014 by Heidarzadeh [61]. The full crystalline tandem cell has accomplished an efficiency of more than 26%. This assessment showed that 3C-SiC is an excellent choice for the top cell of the crystalline tandem silicon solar cell.

In an attempt to demonstrate the ability of 3C-SiC/Si by M. Toure [62] to develop high-voltage solar cells which was the first approach with a simple heterojunction structure. It is evident that the recombination interface is a degradation mechanism and that the electrical quality of the junction should also be enhanced to gain the best photovoltaic parameters.

In 2014 a research by P. Zhou, S. Zheng and others [63] provided evidence to support the view that co-doping is an effective way to improve the PL features of 3C-SiC results of the combined function of band-gap and light absorption.

New intermediate band materials based on Cr doped 3C-SiC for high-efficiency application of solar cells have been simulated in 2015 by M. Eskandari, H. Heidarzadeh [64]. The simulation has also demonstrated that 3C-SiC is an attractive prospect for an intermediate solar band with an efficiency of almost 60 %.

In 2016 the electronic structure and the optical properties of pure 3C-SiC were computed and the actual impact of Ti or Fe doped 3C-SiC has also been investigated by M. Houmad [2]. When Si atoms are substituted by Ti or Fe atoms. The 3C-SiC band-gap had become direct when doped with Ti or Fe and the optical coefficient and conductivity enhanced with titanium and iron doping and it was found that the Fe doped 3C-SiC has a higher optical conductivity than Ti-doped 3C-SiC.

In 2016 J. W. Sun [65] showed that absorption and room temperature photoluminescence in boron-doped 3C-SiC demonstrates a depth of ~0.7 eV above the valence band. This implies that boron-doped 3C-SiC is a good choice for intermediate band photovoltaic material.

Various solar cell formations PN and PIN based on 3C-SiC were investigated by H. Zerfaoui, D. Dib, and B. Kadem in the year of 2018 [66] and the influences of the irradiance level on the electrical properties of these solar cells have been investigated. The results showed that the maximum electrical conversion efficiency for PN and PIN junctions was approximately 23.24 % and 23.41% respectively, making the two proposed structures appropriate for photovoltaic solar cell applications.

Intermediate band (IB) was formed in 3C-SiC in a research by H. Heidarzadeh in 2019 [67] by substituting cobalt (Co) atoms inside the supercell structures. Metallic narrow IB is created within the forbidden 3C-SiC band energy when Co atoms are placed inside it. Maximum conversion rates of around 60 % and 55 % are achieved under the AM1.5 and AM0 spectra respectively.

Recently in March of 2020 and also by Heidarzadeh [68] a single-junction solar cell based on 3C-SiC is assessed using a two-dimensional finite element model. Impacts of n^+ and p^+ thicknesses and operating temperatures on the performance of n^+pp^+3C-SiC solar cells are modeled to determine their true efficiency. The efficiencies of a 5 μm cell were 12.52 %, 11.2 %, 10.3 % and 8.8 % for (n^+) and (p^+) layer thicknesses of 0.2 μm, 0.3 μm, 0.4 μm and 0.5 μm, respectively. Then the performance of silicon and 3C-SiC solar cells at the high temperatures is investigated and the results suggested that for high-temperature applications, the 3C-SiC solar cells are better than the silicon solar cells.

1.4 AIM OF THE WORK

The current work aims at studying and simulating the 3C-SiC thin-film solar cell. The effect of the thickness and doping density of each layer, the environment conditions (temperature and illumination) on the performance of the cell will be investigated.

1.5 ORGANIZATION OF THE THESIS

The thesis is comprised of six chapters. The chapters' outline is summarized below:

Chapter Two contains the theoretical study, which necessary to explain and describe solar cells in general.

Chapter Three characterizes with the proposed model of 3C-SiC and the properties of the used materials.

Chapter Four provides a little information on how the user can use the simulation software, it also includes the input data and a parametric study on the reference cell, and finally discusses the results of the study.

Chapter Five deals with the simulation results about the impact of the physical characteristics on the optimized structure.

And finally, Chapter Six discusses the conclusions and recommendations for future studies.

A part of this work has been published in a “Solid State Technology journal [69].

CHAPTER TWO

THEORY OF PHOTOVOLTAIC

2.1 INTRODUCTION

Solar cells can generate electricity when illuminated by sunlight or artificial light. They directly transform the energy from solar radiation which is based on the photovoltaic effect into electrical power [18], which can be converted easily to other forms for the benefit of the world. Typically, the solar cell-structure is based on semiconductor material, which has the capability to absorb the incident light with energy that is greater than the band-gap of this material. This type of solar cell is made of a PN junction. When the semiconductor is under illumination, the photovoltaic process occurs. This process can be summarized as when the photons with high energies are absorbed inside the semiconductor that leads to the creation of EPH (electron-hole pairs). When a material absorbs the light, the photons start losing their energy to excite the electrons to higher levels of energy. The excited electrons decay slowly to their ground state. These excited electrons are harvested and fed into an external circuit before they can relax in their ground condition. These generated carriers must be collected efficiently in order to be able to contribute to the generation of photocurrents and therefore to the generation of electricity [70].

2.2 SOLAR SPECTRUM

The sun emits electromagnetic radiation as a black body with a surface temperature of 6000 K. This is due to the nuclear reactions happening in the sun. The nuclear fusion processes are wherein helium created from hydrogen [71]. This process makes the temperature of the sun’s core and surface to be 1.57x10^7 K and ~ 5578 K, respectively. Nuclear activity generates huge amounts of radiation in turn this radiation produces energy of light called photons. Photons do not have a physical mass of their own but carry huge amounts of energy and momentum. Different photons have different wavelengths of light. Some of them will carry non-visible light (IR infrared and UV ultra-violet), whilst others will carry visible light (white light) [72]. Figure (2.1) shows the electromagnetic spectrum of solar radiation [73].

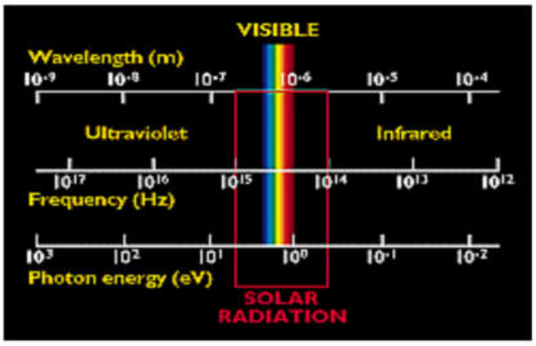

Fig. (2.1) Electromagnetic spectrum [73].

The solar spectrum and the correlating solar intensity that reaches the earth's surface are different from the spectrum that reaches outer space. The air mass coefficients (AM) have been defined for comparing the solar module performance, air mass can be described mostly as a parameter that focuses on the effect of the allocation of wavelength on the photon flow [74], which varies depending on weather conditions such as water vapor and dust [75]. The solar power intensity without the effect of the atmosphere or ground surface is called the Air Mass Zero AMO = 135.3 mW.cm^{-2} [71]. The AM1 solar radiation spectrum identifies the sun's rays on the earth's surface when the sun is at its zenith angle. Total incident power of sunlight 92.5 mW.cm^{-2} under condition AM1. AM1.5 G (global) is the basic spectrum on the surface of the earth. Figure (2.2) shows AM0, AM1, AM1.5, and AM2 [73].

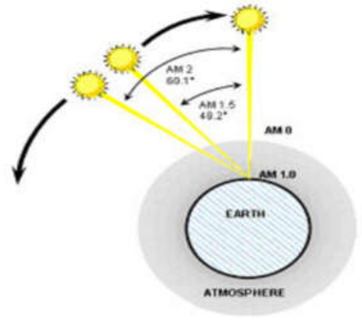

Fig. (2.2) AM0, AM1, AM1.5, and AM2 [73].

The AM1.5 G spectrum (θ = 48.2 °) has indeed been standardized to be 100 mW.cm^{-2} [76], figure (2.3) shows the solar spectrum at different AM conditions [77]. The most suitable incident solar irradiance for calculating solar cell power conversion efficiency is the AM1.5 G spectrum.

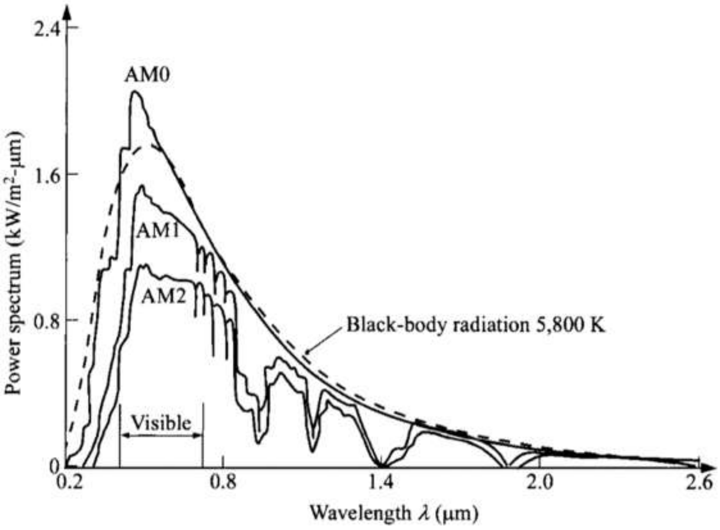

Fig. (2.3) Solar spectrum at different air-mass conditions [77].

2.3 THE OPTICAL ABSORPTION AND CHARGE CARRIERS GENERATION IN THE SEMICONDUCTOR MATERIAL

2.3.1 OPTICAL ABSORPTION

The photon incident on the semiconductor surface will either be reflected from the top surface or penetrate and absorbed inside the material. In the absence of either of the above two processes, transmitted through the material [73]. Reflection and transmission of photovoltaic devices are generally considered loss mechanisms because unabsorbed photons will not contribute in power generation. If the photon is absorbed, it has the possibility of exciting an electron from the valence band to the conduction band. A key factor in determining if a photon is absorbed or transmitted is the energy of the photon. The photons falling on the semiconductor material can be classified into three types based on their energy compared to the semiconductor band-gap [78]:

- If the energy of the photon E_{ph} is less than the energy gap of the band E_g, interacts only weakly with the semiconductor, passing through as though it were transparent. Photons with energy smaller than E_g will not be absorbed and the semiconductor is transparent for light with wavelengths longer than the cut-off wavelength (λ_c). Photons can be categorized by their frequency ν and by their wavelength λ [78]:

$$\lambda = c/v \qquad (2.1)$$

- If the energy of the photon E_{ph} is equal to the energy gap E_g, Just have enough energy to create an electron-hole pair and absorb it efficiently.
- Photons with higher energy than the band-gap are strongly absorbed. However, the photon energy greater than the band-gap

is wasted for photovoltaic applications, as electrons rapidly thermalize back down to the edges of the conduction band.

Photons can also be characterized by their energy E:

$$E = \ \ v = \frac{c}{\lambda} \qquad (2.2)$$

h is the constant of blank = 4.1357×10^{-15} eV s .

c is the light's speed in vacuum = 3×10^{8} m.s^{-1}.

E is the energy in eV and λ is the wavelength in nm.

A useful relationship is given which enables a fast calculation of the energy for wavelengths, and vice versa [78]:

$$E = \frac{1{,}240}{\lambda} \qquad (2.3)$$

For solar cells, the most important optical constant is the optical absorption coefficient α. The absorption coefficient is a measure of the distance a light wave travels into the material before it is absorbed [79]. Figure (2.4) shows the absorption coefficient of several semiconductor materials [78]. The absorption of photons in a solar cell to create carrier pairs and thus a photocurrent is dependent on the absorption coefficient α (cm^{-3}). The absorption coefficient determines the luminous penetration depth 1 / α in the semiconductor material according to Lambert–Beer's law [78]:

$$\mathrm{I(x)} = \mathrm{I_0}\ \exp(\ \ \alpha\, \mathrm{x}) \qquad (2.4)$$

I_0 is the radiation intensity falling on a semiconductor surface.

I(x) is the intensity that remains after the light penetrated to a distance (x).

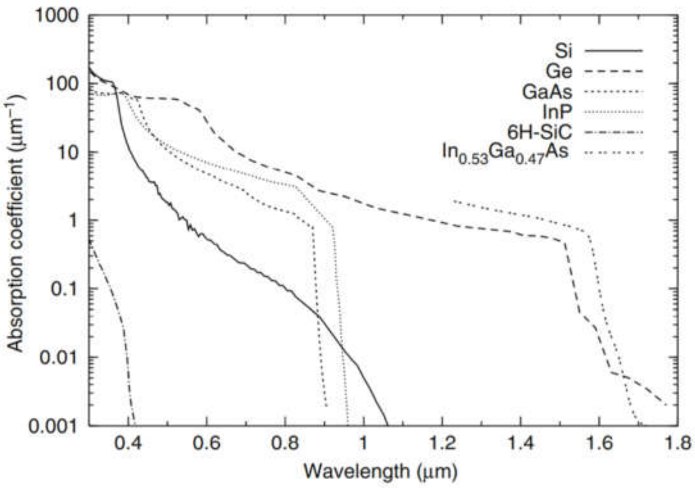

Fig. (2.4) Absorption coefficients of important semiconductor materials versus wavelength [78].

2.3.2 GENERATION OF CHARGE CARRIERS

- Band-to-Band Transitions

The primary means of generating carriers in solar cells is the absorption of light. For a planar slab figure (2.5) a photon that entering the semiconductor generates δx electron-hole pairs in a thin layer at depth (x+δx). The function of generation g(x) is given by [80]:

$$g(x) = \alpha(\lambda)\ \exp\{\ \ \alpha(\lambda)x\} \qquad (2.5)$$

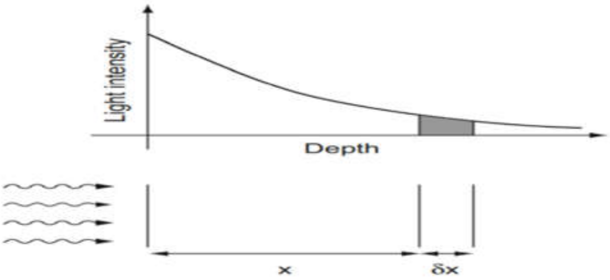

Figure (2.5) physics used to discuss the absorption of light in semiconductors [80].

Where α (λ) is the absorption coefficient. The generation rate G per unit volume is related to the generation function g in equation (2.5) by G=g/A, where A is the illuminated area of the sample.

- Free-Carrier Absorption

In high-carrier regions (due to doping or strong lighting), photon absorption could also occur by electron transitions within the same band, with initial and final states. This absorption by free carriers does not generate pairs of electron-hole and competes with transitions from band to band that generate the photo-generated current, which has been debated above [80]. Free-carrier absorption may be important for photon energies close to the band-gap, and should not be included in the coefficient of absorption (α) before exponential in equation (2.5).

2.4 THE PN JUNCTION

PN junction semiconductor is produced by doping impurities p-type and n-type on a wafer, as shown in figure (2.6) [76]. The interface plane at the boundary where two semiconductor regions meet is called a junction. Theoretically, the density of donors and acceptors is equal in the junction plane [76]. A grain boundary is introduced if it is constructed from two different parts so that PN junctions are created in the single crystal of semiconductor by a doping process. Following three phenomena take place at the junction [76]:

- The space-charge region or depletion region or transition region shall be established all over the junction.
- A potential barrier is formed across the PN junction.
- The existence of the depletion layer gives rise to junction and diffusion capacitances.

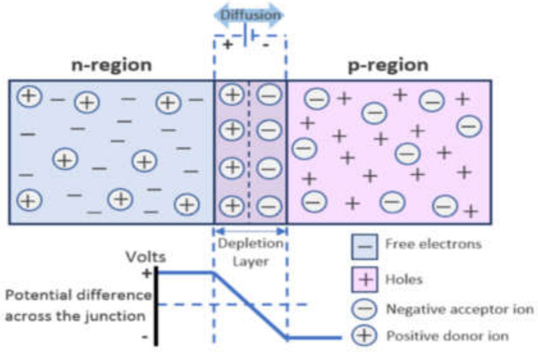

Fig. (2.6) PN junction semiconductor diode [76].

2.5 DEPLETION REGION ELECTRICAL CHARACTERISTICS

If there were two separate pieces of semiconductor material. The doping concentrations in both pieces are constant, and equal to in the n-type region, and in the p-type region, a PN junction is at thermodynamic equilibrium [79].

$E_{Fn} \quad E_i = KTln\left(\frac{N_d}{n_i}\right)$ (2.6) in the n-type region

$E_i \quad E_{Fp} = KTln\left(\frac{N_a}{n_i}\right)$ (2.7) in the p-type region

Where E_f of (n,p,i) is the fermi level for (n-type, p-type and intrinsic semiconductors). KT is the product of the Boltzmann constant and the temperature, N_d is the donors carrier concentration, N_a is the acceptors carrier concentration, and n_i is the intrinsic carrier concentration. When these two pieces are attached together, the surface where the contact is made is called the "metallurgical junction" figure (2.7), electrons instantly diffuse from the electron-rich n-type region into the electron-poor p-type region, and holes from the p-type material diffuse into the n-type region. As a result of the charge displacement an internal built-in potential called junction potential, Φ_0 is formed at the junction. Within a multiplication factor-q the junction potential is equal to the curvature of the energy bands, q is an electronic charge [79]:

$$E_{Fn} \quad E_{Fp} = q\Phi_0 = KTln\left(\frac{N_d}{n_i}\right) + KTln\left(\frac{N_a}{n_i}\right) = KTln\left(\frac{N_d\,N_a}{n_i^2}\right) \qquad (2.8)$$

$$\Phi o = \frac{KT}{q}ln\left(\frac{N_d\,N_a}{n_i^2}\right) \qquad (2.9)$$

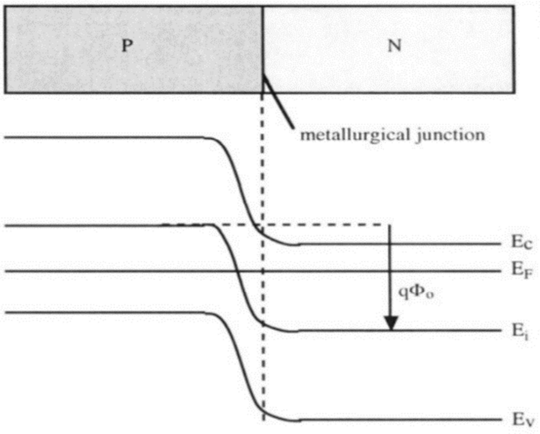

Fig. (2.7) PN junction and corresponding band diagram [79].

When electrons diffuse from the n-type region into the p-type material, they "leave behind" the ionized donor atoms they originated from. These atoms occupy substitutional sites in the crystal lattice and cannot move within the crystal. The region where these positively charged ions are located constitutes a space-charge region called a "depletion region" because it is depleted of electrons. The positive charge in the depletion region attracts electrons in such a way as to equilibrium, the diffusion force which pushes electrons into the p-type region is precisely balanced by the force of the built-in electric field that recalls the electrons back into the n-type region. Likewise, the diffusion of p-type holes into the n-type region results in a depletion region in type p material. The positive charge in the depletion region attracts electrons such that at equilibrium, the force of diffusion pushing electrons into the p-type region is exactly balanced by the force of the built-in electric field that "recalls" the electrons back into the n-type region. Similarly, the diffusion of holes from the p-type into the n-type region gives rise to a depletion region in the p-type material. This region is depleted of holes and bears a negative charge because of the presence of negatively charged acceptor ionized atoms. There are several names for the depletion region located around the metallurgical junction; it may be called the "depletion region", the "space-charge region" or the "transition region" [79], Figure (2.8) illustrates the creation of depletion regions by the diffusion of electrons and holes [79].

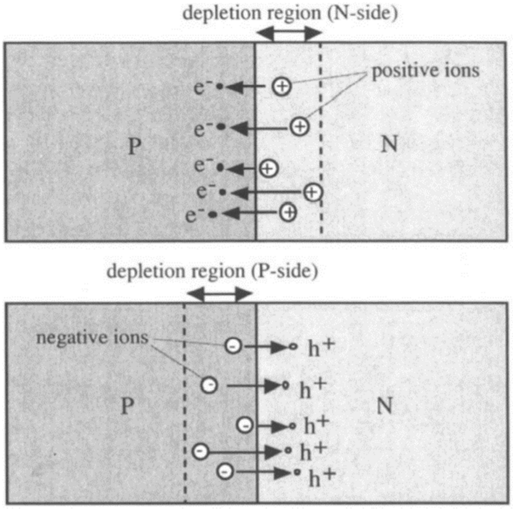

Fig. (2.8) creation of depletion regions by the diffusion of electrons and holes [79].

Use the Poisson equation to calculate the electric field and the potential variation in the space-charge region [79]:

$$\frac{dE}{dx} = \frac{d^2\Phi(\mathrm{x})}{dx^2} = \quad \frac{q}{\varepsilon}(p \quad n + N_d^+ \quad N_a^-) \qquad (2.10)$$

Where, ε is the permittivity, p is a concentration of holes, n is a concentration of electrons, N_a^- ionized acceptor doping carrier concentration, and $N_d^+$is an ionized donor doping carrier concentration. Using Boltzmann Relationships:

$$\frac{d^2\Phi(\mathrm{x})}{dx^2} = \quad \frac{q}{\varepsilon}\left\{p_o \exp\left[\quad\frac{q\Phi(\mathrm{x})}{KT}\right] \quad n_o \exp\left[\frac{q\Phi(x)}{KT}\right] + N_d^+ \quad N_a^-\right\} \quad (2.11)$$

Where p_o is the intrinsic holes concentration and n_o is the intrinsic electrons concentration. The last equation cannot be solved analytically and a close-form solution for the potential cannot be found. It can, however, be simplified by using the "depletion approximation". Accordingly, in the situation of the abrupt PN junction observed here and under the given concentrations, the concentrations of n and p compared to the fixed charges may be ignored at room temperature [81]. In the region $x_l < x < 0$, the volume charge density is determined solely by the N_a^- acceptors and, similarly, in the region n, $0 < x < x_l$ the volume charge density is determined by the N_d^+ donor concentration. The concentrations of the respective charging carriers are constant in the other regions $x < x_l$ and $x > x_r$. On the p side of the space-charge region [81]:

$$\frac{dE}{dx} = \quad \frac{q}{\varepsilon} N_a^- \qquad (2.12)$$

And for the n side:

$$\frac{dE}{dx} = \quad \frac{q}{\varepsilon} N_d^+ \qquad (2.13)$$

Outside these zones $\frac{dE}{dx} = 0$

By integrating-and taking into consideration the boundary conditions $E_{x=l} = 0$ and $E_{x=r} = 0$, we derive the following pathways for the electrical field [81].

$$E(x) = \quad \frac{qN_a^-}{\varepsilon}(x \quad x_1) \quad (2.14)$$

And in the n region of the depletion region:

$$E(x) = \quad \frac{qN_d^+}{\varepsilon}(x_r \quad x) \quad (2.15)$$

The field path is thus linear and always negative with the positional coordinates. Where x = 0 the field strength is at its maximum and both values must be of equal magnitude. Then it maintains that

$$N_a^- x_1 = N_d^+ x_r \qquad (2.16)$$

In order to determine the potential space-charge region distribution equations (2.14) and (2.15) has to be integrated with the following boundary condition [81]:

$$\frac{d\Phi}{dx} = 0 \qquad \text{for x= x}_r \text{ and x= x}_l\text{:}$$

$$\Phi(\mathrm{x}) = \frac{qN_a}{\varepsilon}\,\frac{1}{2}(x_1 \quad x)^2$$

$$+\,D \qquad (2.17)\ \text{n region of the depletion layer}$$

$$\Phi(\mathrm{x}) = \quad \frac{qN_d}{\varepsilon}\,\frac{1}{2}(x_r \quad x)^2$$

$$+\,C \qquad (2.18)\ \text{p region of the depletion layer}$$

The origin point for voltage is chosen, so that $\Phi_{x=0} = 0$. This leads to determine the constants C and D. thus the potential in the space-charge region is [81]:

$$\Phi_{x^-} = \quad \frac{qN_a^-}{\varepsilon}\,[x_1^2 \quad (x_1 + x)^2] \qquad (2.19)\ \text{p region}$$

$$\Phi_{x^+} = +\frac{qN_d^+}{\varepsilon}\,[x_r^2 \quad (x_r + x)^2] \qquad (2.20)\ \text{n region}$$

Distribution of field strength and voltage is shown in figure (2.9).

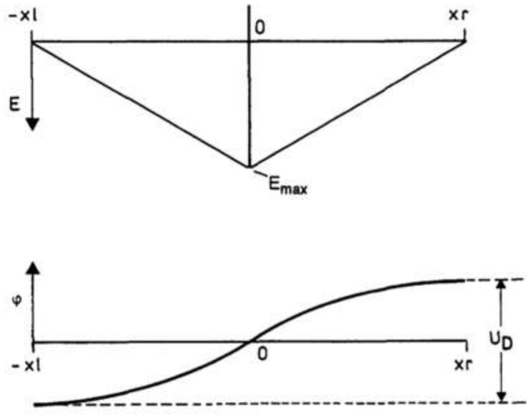

Fig. (2.9) Field and potential distribution in a PN junction [81].

Outside the depletion region the potential is as follows:

$$\Phi_{x^-} = \quad \frac{qN_a^-}{\varepsilon}\,x_1^2 \qquad (2.21)\ \text{p region}$$

$$\Phi_{x^+} = +\frac{qN_d^+}{\varepsilon}\,x_r^2 \qquad (2.22)\ \text{n region}$$

Space-charge region width and capacitance are significant equations and must to be considered. The built-in potential barrier (V_{bi}) for the PN junction is given by [81]:

$$V_{bi} = \frac{kT}{q} ln\left(\frac{N_d N_a}{n_i^2}\right) = \frac{q}{2\varepsilon}(N_d x_r^2 + N_a x_1^2)$$

$$= \frac{q}{2\varepsilon}(N_d x_r^2 + N_a x_1^2) \quad (2.23)$$

And because of $N_d x_n = N_a x_p$, the values of x_r and x_1 are [81]:

$$x_r = \sqrt{\frac{2\varepsilon(V_{bi}+V_R)}{q}\left\{\frac{N_a}{N_d}\left(\frac{1}{N_d+N_a}\right)\right\}} \quad (2.24)$$

V_R is the reverse applied biasing voltage.

$$x_1 = \sqrt{\frac{2\varepsilon(V_{bi}+V_R)}{q}\left\{\frac{N_d}{N_a}\left(\frac{1}{N_d+N_a}\right)\right\}} \quad (2.25)$$

The total depletion region width W is the sum of the two components given as:

$$W = x_r + x_1 = \sqrt{\frac{2\varepsilon(V_{bi}+V_R)}{q}\left\{\left(\frac{N_d+N_a}{N_d N_a}\right)\right\}} \quad (2.26)$$

The maximum electric field at the junction is:

$$E_m = \sqrt{\frac{2q(V_{bi}+V_R)}{\varepsilon}\frac{N_d N_a}{N_a+N_d}} \quad (2.27)$$

Since there will be a separation of positive and negative charges in the space-charge region, the capacitance is correlated with the PN junction. The depletion region capacitance can be written as [81]:

$$C_{dep} = qN_d \frac{dx_r}{dV_R} \quad (2.28)$$

$$C_{dep} = \sqrt{\frac{q\varepsilon N_d N_a}{2(V_{bi} + V_R)(N_d + N_a)}} \qquad (2.29)$$

2.6 BASIC SEMICONDUCTOR EQUATIONS

To evaluate the Solar Cell performance, basic semiconductor equations got to be solved, these equations play a real-valued role. The governing equation is the Poisson equation that relates the charge to electrostatic potential. The Poisson Electrostatic Potential equation is given in equation (2.30) [76].

$$\frac{d^2E}{dx^2} = \frac{\rho}{\varepsilon} \qquad (2.30)$$

Where and ρ is the density of charge ($C.cm^{-3}$) and from charge neutrality equation ρ can be expressed as given in equation (2.31) [76] with an assumption that dopant is fully ionized.

$$\rho = q(p \quad n + N_d^+ + N_a^-) \quad (2.31)$$

By putting equation (2.31) in equation (2.30), it becomes equation (2.32) [76].

$$\frac{d^2E}{dx^2} = \frac{q(p - n + N_d^+ + N_a^-)}{\varepsilon} \qquad (2.32)$$

The second equation is an equation of continuity, the reason the equation of continuity is called governing equation because drift, diffusion, generation and recombination are analyzed concurrently. Equation (2.33) and (2.34) represent continuity equation for concentration change in electron and hole [76].

$$\frac{\partial n}{\partial t} = \frac{1}{q}\,\frac{\partial J_n}{\partial x} + (G_n \quad R_n) \qquad (2.33)$$

$$\frac{\partial p}{\partial t} = \frac{1}{q}\,\frac{\partial J_p}{\partial x} + \left(G_p \quad R_p\right) \qquad (2.34)$$

Where J_n is the electrons current density, J_p is the holes current density, G_n, G_p is the generation rate for electrons and holes, and R_n, R_p is the recombination rate for electrons and holes respectively. To calculate the current and characteristics of a solar cell simulator must be capable of solving the drift-diffusion equation for current in a solar cell.

2.7 TRANSPORT PROPERTIES

Unlike the conditions of equilibrium, a net electrical power under operating conditions current flows through the device. The electric currents are produced in a semiconductor because electrons and holes transport the charge from place to place. In a semiconductor, two basic transport mechanisms are drift and diffusion [14].

- **Drift**

Drift is the motion of charged particles in proportional to the electric field. Due to collisions with thermally vibrating lattice atoms and ionized impurity atoms, the carrier's acceleration is often disturbed. The resulting motion of electrons and holes can be described by mean drift velocity v_{dn} and v_{dp} for electrons and holes, respectively. In the case of low electrical field, the average drift velocity is directly proportional to the electrical field as demonstrated by the equations (2.35) and (2.36). The proportionality factor is called mobility μ. Mobility is a measure of how easily the charged particles can move through a semiconductor material and is a primary parameter that characterizes the transport of electrons and holes due to drift[14].

$$v_{dn} = \mu_n E \quad (2.35)$$

$$v_{dp} = \mu_p E \quad (2.36)$$

Where μ_n and μ_p are the mobility of electron and hole respectively. Even though the electrons flow in the reverse direction to the electric field, since an electron's charge is negative, the resulting electron drift current is in the same direction as the electric field and this illustrates in figure (2.10)[14].

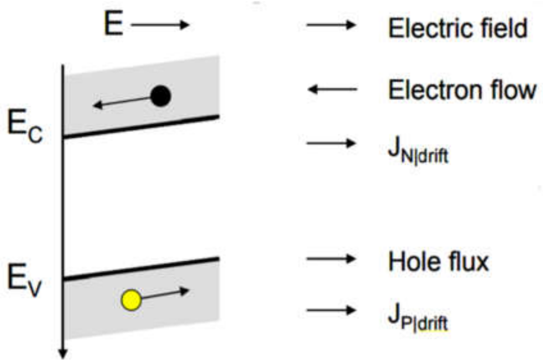

Fig. (2.10) Visualization of carrier drift using the band diagram [14].

The electron and hole drift-current densities $J_{n\,drift}$, $J_{p\,drift}$ are defined by equations (2.37), (2.38) and the total drift current by equation (2.39).

$$J_{n\,drift} = q\,n\,v_{dn} = q\,n\,\mu_n\,E \qquad (2.37)$$

$$J_{p\,drift} = q\,p\,v_{dp} = q\,p\,\mu_p\,E \qquad (2.38)$$

$$J_{drift} = q(p\,\mu_p + n\,\mu_n)\,E \qquad (2.39)$$

- **Diffusion**

Diffusion is a process by which particles tend to spread from high particle concentration regions to low particle concentration regions as a result of irregular thermal motion. The gradient in the concentration of the particles in the semiconductor is the driving force for the transmission of the particles associated with the diffusion. Contrary to the mechanism of drift transport, the particles do not need to be charged to participate in the diffusion process. Currents resulting from diffusion are proportional to the particle concentration gradient and expressed through equations (2.40) and (2.41) and total diffusion current through equation (2.42) [14]. The total current due to both drift and diffusion expressed by equation (2.43) [14].

$$J_{n\,diff} = q\,D_n\,\nabla n \qquad (2.40)$$

$$J_{p\,diff} = q\,D_p\,\nabla p \qquad (2.41)$$

$$\mathrm{J}_{\mathrm{diff}} = \mathrm{q}(\, D_n \nabla \mathrm{n} \quad D_p \nabla \mathrm{p}\,) \quad (2.42)$$

$$\mathrm{J} = \mathrm{J}_{\mathrm{drift}} + \mathrm{J}_{\mathrm{diff}} = q\left(p\, \mu_p + n\, \mu_n\right) \mathrm{E} + \mathrm{q}(\, D_n \nabla \mathrm{n} \quad D_p \nabla \mathrm{p}\,) \quad (2.43)$$

Proportionality constants, D_n and D_p, are referred to as electron and hole diffusion coefficients, respectively, the electron and hole diffusion-current densities are $J_{n\ \mathrm{diff}}$, $J_{p\ \mathrm{diff}}$. The diffusion coefficients of electrons and holes are linked by the Einstein relationship, which is expressed by equations (2.44) and (2.45), to the mobilities of the corresponding charge carriers.

$$\frac{D_n}{\mu_n} = \frac{KT}{q} \qquad (2.44)$$

$$\frac{D_p}{\mu_p} = \frac{KT}{q} \qquad (2.45)$$

Figure (2.11) [14] shows the visual representation of the diffusion process and the resulting directions of particle fluxes and current.

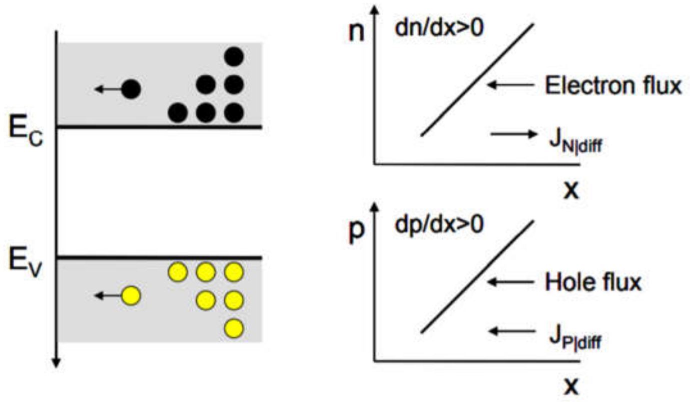

Fig. (2.11) Visualization of carrier diffusion using the band diagram [14].

2.8 RECOMBINATION PROCESSES

Some of the generated electrons and holes are annihilated in a reaction known as recombination. From the energy freed in this reaction, either photons or phonons are created, or both are produced simultaneously [82]. Nature is conservative, because it always offers several mechanisms able to bring the system back to balance. In the case of electron-hole pairs, these are generation-recombination mechanisms. Each process needs an associated interaction. The interaction with the electromagnetic field allows for the radiative recombination in which the photon is emitted, while the absorption of the photon corresponds to the electron-hole pair generative process [83].

Non-radiative generation-Recombination mechanisms are often nuisance optoelectronics as they proceed in parallel and competition with radiative processes. It is therefore important to recognize them in order to assess the performance and limitations of optoelectronic devices. The two major processes are as follows [83]:

- Shockley-Read-Recombination hall, in which impurities play a key role. At first, an electron and then a hole is stuck in the same impurity center, removing a single electron-hole pair. Figure (2.12) illustrates the SRH recombination process.

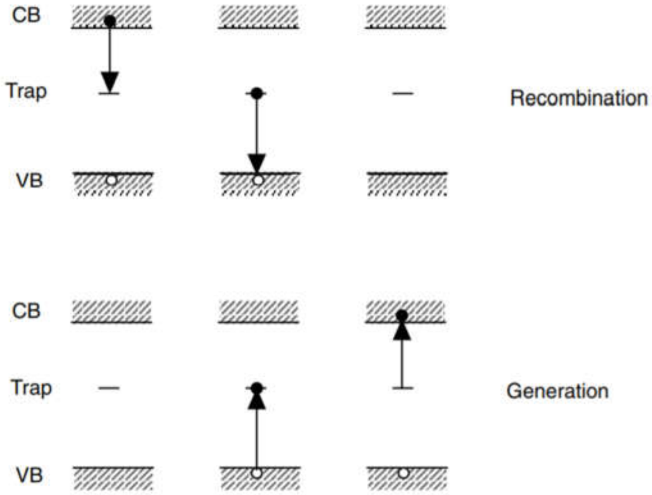

Fig. (2.12) Shockley-Read-Hall recombination and generation processes [83].

- Auger recombination resulting from electron-electron interaction, by which the electron recombines with a hole and transfers the resulting energy from recombination to another electron (or hole) in the form of kinetic energy figure (2.13) shows the auger recombination process [83]. This is an intrinsic process and is not dependent on the participation of centers of defects or impurities. In this case, the respective process of generation is impact ionization, where an electron with appropriate kinetic energy could develop an electron-hole pair by transporting its energy in the valence band to an electron and promoting it to the conduction band [83].

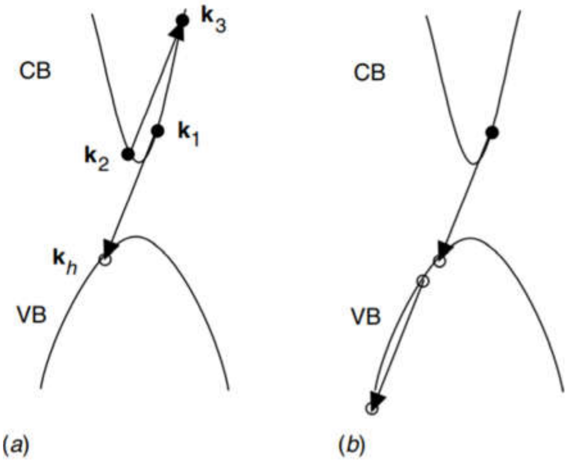

Fig. (2.13) Two possible Auger recombination processes:(a) an electron with momentum k_1 recombines with a hole k_h and another electron at k_2 receives the liberated energy and is promoted to k_3 (CHCC); (b) a similar process involving two holes and a single electron at the outset (CHHH) [83].

2.9 DEFECTS

The existence of prohibited energy bands results from the periodicity of the crystal potential. Any deviation from this periodicity will thus introduce additional, allowable levels of energy to the electron in the band-gap [83]. A crystal defect occurs by altering the perfect crystal in such a way that it does not reproduce the original crystal. Defects can generally be classified as point defects, line and surface defects, and dislocations. Defects can lead to band-gap states. Some defects have favorable impacts, such as doping [84], figure (2.14) shows the defects in one-dimensional periodic potential [83].

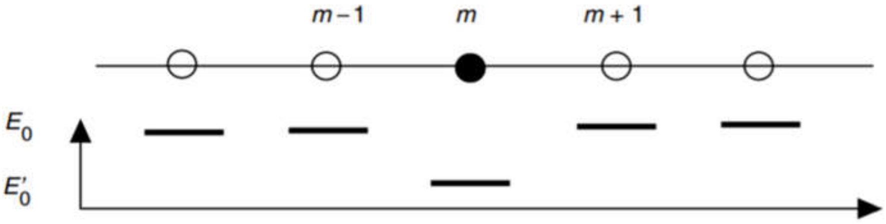

Fig. (2.14) Representation of a defect in a one-dimensional periodic potential [83].

Defects that create states close to the center of the band-gap tend to function as recombination centers. If conduction carriers are lost to these recombination centers, the carrier population must reduce and the conductivity must be weaker than without defects [84]. Point defects may be divided up into impurity and native point defects. Impurities refer to the random placement of foreign atoms in the crystal. Some impurities, including doping, have a beneficial effect. However, other impurities and defects of the native point aim to lower conduction and emission efficiency. Point defects may extend over several nuclear lattice sites [84].

2.10 THE EQUIVALENT CIRCUIT OF THE SOLAR CELLL

As shown in the figure (2.15) [80] an ideal solar cell can be represented by a current source connected in parallel with a rectifying diode. This model is the equivalent circuit diagram of the PV system and is called the "four parameters model" which consists of a current source, a diode, a series resistance, and parallel resistance. The current source symbolizes the light produced by the solar cell, the diode represents the nonlinear impedance of the PN junction, the resistance of the series R_S

represents the internal electrical losses and the resistance of the shunt R_{Sh} corresponds to the current of leakage to the ground. The respective JV characteristic is defined in the solar cell equation of Shockley (2.46) [80]:

$$I = I_{ph} \quad I_0\left(\exp\left(\frac{qV}{KT}\right) \quad 1\right) \quad (2.46)$$

Keeping in mind that a solar cell in the dark is simply a semiconductor current rectifier or diode. I_0 is the saturation current, the photo generated current I_{ph} is closely related to the photon flux incident on the cell, and its dependence on the wavelength of light [80].

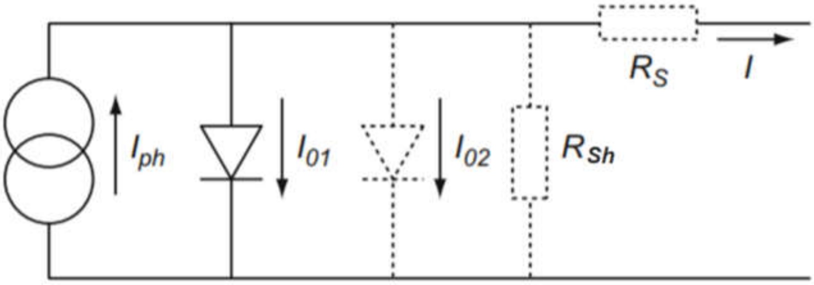

Figure (2.15) The equivalent circuit of the optimal solar cell (full line). The non-ideal components are shown by the dotted line [80].

The JV characteristics of an ideal solar cell comply with the superposition principle: the functional dependence can be obtained from the corresponding characteristic of a diode in the dark by shifting the diode characteristic along the current axis by $I_{ph,}$ figure (2.16) [80].

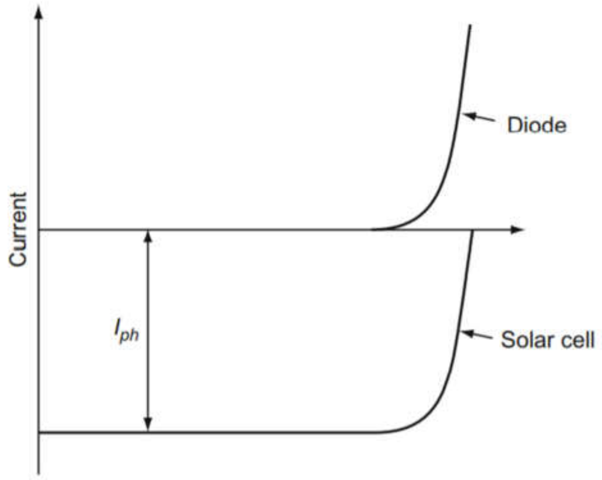

Figure (2.16) The superposition principle for solar cells [80].

In practice, the JV characteristic of a solar cell usually differs to some degree from the ideal characteristic. A two-diode model is often used to fit the observed curve, with a second diode containing an 'ideality factor' of two in the denominator of the exponential term argument. Solar cells (or circuits) also may have series (R_S) and parallel (or shunt, R_{Sh}) resistances, resulting in greater resistance [80].

$$I = I_{ph} \quad I_{0_1}\left(\exp\left(\frac{V + IR_S}{KT}\right)\right) \quad I_{0_2}\left(\exp\left(\frac{V + IR_S}{2KT}\right) \quad 1\right)$$
$$\frac{V + IR_S}{R_{Sh}} \quad (2.47)$$

2.10.1 PARASITIC RESISTANCES

- **Series resistance R_S:**

This resistance has the following components: a contact resistance metal-semiconductor, ohmic resistance in the metal contacts, ohmic resistance in the semiconductor material. Figure (2.17) indicates the effects of series resistance [81]. It mainly affects the fill factor that is influenced by increasing resistance. Only at high (usually not possible) values does the short-circuit current drop off. To achieve the highest possible efficiency, the series resistance must be kept as low as possible (equal or less than 0.5 $\Omega.cm^2$) [81].

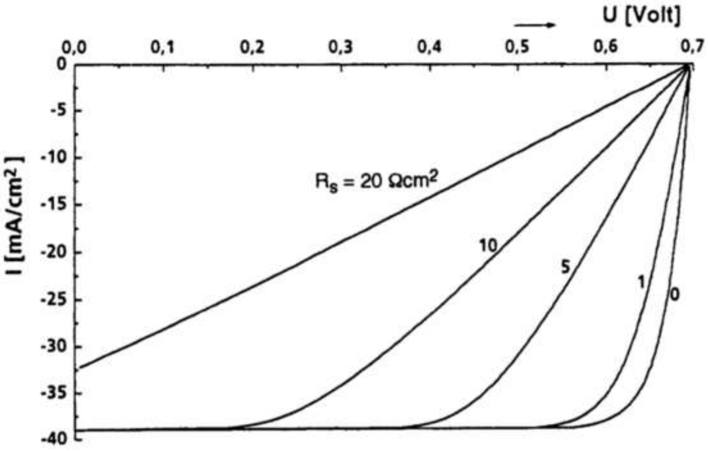

Figure (2.17) The influence of series resistance on solar cell parameters [81].

Series resistance R_S, can be calculated accurately by using both light and dark measurements. In order to measure the dark current, a higher voltage (V_a) than the open-circuit voltage (V_{OC}) is required to obtain a current having the same value as the short-circuit current, because the additional voltage drop at the series resistance must be overcome. The series resistance can be determined from the difference between the two voltages [81]:

$$V_a \quad V_{OC} = R_S\, I_{SC} \qquad (2.48)$$

- **Shunt resistance R_{Sh}:**

The value of this resistance is evaluated by the leakage of currents along the edges of the solar cell. Point defects in the PN junction also can result in low parallel resistance. Such defects may be PN junction interruptions, which arise during the diffusion of the n emitter, impurity particles at certain points have hindered diffusion. The base material can also be in electrical contact with the finger structure at a certain points, generating a short-circuit (if only a small one) [81]. Figure (2.18) displays the impact of shunt or parallel resistance. With lowering resistance the fill factor FF reduces in the first estimation and only at very small values (below 100 Ω.cm^2) the open-circuit voltage also lessens [81], short-circuit current is not influenced by parallel resistance.

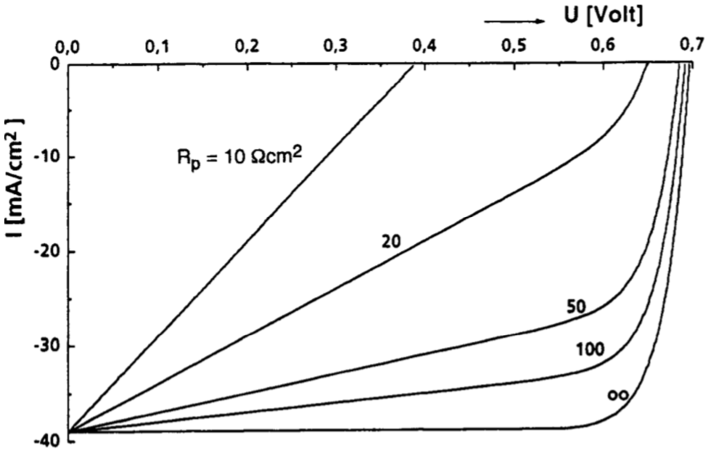

Figure (2.18) The influence of shunt resistance on solar cell parameters [81].

2.11 BASIC PHOTOVOLTAIC PARAMETERS

1. Short-circuit current

Short-circuit current (I_{SC}) is the maximum current flow through the solar cell at zero load condition (i.e. the short-circuited solar cell). The maximum I_{SC} voltage value across the solar cell will be zero. Short-circuit current flows due to generation and collection of light-generated carriers. It depends mainly on the number of incident photons and their spectrum, the optical properties, collection probability and the area of a solar cell [85]. The graphical representation of the short-circuit current is given in figure (2.19) [76].

2. Open-circuit voltage

The open-circuit voltage (V_{OC}) is the maximum voltage from the solar cell. When the solar cell is open-circuit, there is no connection in the charges across the solar cell, then the current will be at its minimum (zero) value, while the voltage will be at the highest value. By establishing the net current to zero in the solar cell equation (2.49) [85], V_{OC} can be derived.

$$V_{OC} = \frac{nkT}{q} \ln\left(\frac{I_{ph}}{I_0} + 1\right) \text{at } I = 0 \quad (2.49)$$

The open-circuit voltage (V_{OC}) varies depending on the light generated (I_{ph}) and the saturation current (I_0) from the above formula. I_0 relies on the recombination of the solar cell. So, V_{OC} is a measure of the amount of recombination of the solar cell. The graphical representation of V_{OC} is illustrated in figure (2.19) [76].

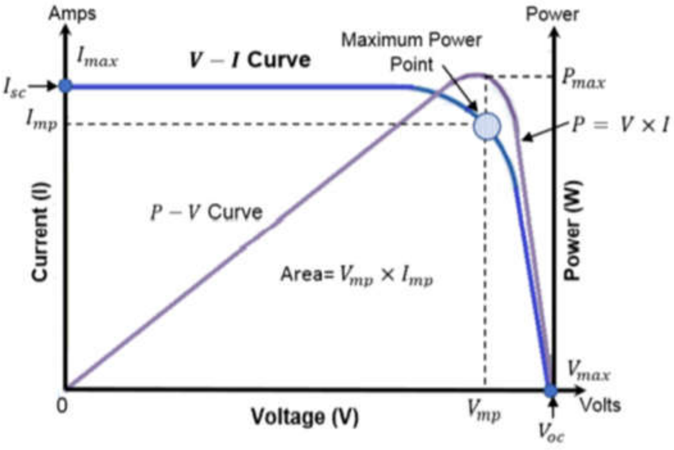

Figure (2.19) I_{SC} and V_{OC} representation in J-V cure [76].

3. Fill Factor and maximum power

The fill factor, indicated by FF in figure (2.20) [86], is a graphical tool that provides a ratio that defines the quality of a power cell. Generally, a less rounded JV characteristic curve would provide a higher fill factor and a high-quality solar cell. The fill factor is characterized as [86]:

$$FF = \frac{I_{mPP} V_{mPP}}{I_{SC} V_{OC}} = \frac{P_{mpp}}{I_{SC} V_{OC}} \quad (2.50)$$

Where:

P_{mpp} is the power at the maximum power point, V_{mpp} is the maximum voltage, I_{mpp} is the maximum current, V_{OC} is open-circuit voltage, I_{sc} is short-circuit current.

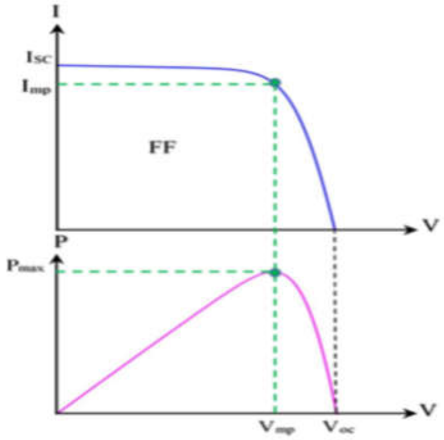

Figure (2.20) Characteristic curves of a solar cell diode [86].

4. Efficiency

Solar cell efficiency provides the means of quantifying the power output of a PV cell as a percentage-ratio of the input of the sun. A low-efficiency cell requires more power generation, needs more natural resources, and will have a higher relative cost of manufacturing compared to a more efficient cell [86].

$$\eta = \frac{P_{mpp}}{P_{in}} = \frac{I_{SC} V_{OC}\, FF}{(\frac{\text{Area(mm2)}}{1000})} . 100 \qquad (2.51)$$

Where:

P_{in} is the solar cell input power, FF is the fill factor, and Area is the surface area of the solar cell.

5. Quantum Efficacy

Spectral response provides important data on the spectral reliance of the photocurrent which is used to identify the factors involved for the short-circuit current reduction. Quantum efficiency is closely linked to the spectral response. External Quantum Efficiency (EQE) is the ratio of the number of carriers collected to the number of incident photons of a given energy. The EQE includes the impact of photons that are transmitted and reflected. However, it is more necessary to assess the efficiency of the carrier's collection by investigating Internal Quantum Efficiency (IQE). The IQE refers to the quantum efficiency that could be produced by photons which are not reflected and transmitted. The IQE can be calculated by the equation [87]:

$$IQE(\lambda) = \frac{EQE(\lambda)}{1-R(\lambda)-T(\lambda)} \quad (2.52)$$

Where, R is the Reflectance, and T is the Transmittance.

CHAPTER THREE

3C-SiC SOLAR CELL

3.1 INTRODUCTION

Photovoltaic solar cells have become widely accepted for the production of clean, renewable energy. This was premised on more than 40 years of research that has profited from the revolution in silicon electronics and compound semiconductors in optoelectronics [88]. The challenge is to gain maximum amount of electrical power from the energy of the sun. In addition to the restrictions of the basic science of such devices, the formulation of materials presents a serious challenge. The latter became more prevalent in the need to lower the cost of photovoltaic modules manufacturing as it joins popular power generation [88].

Two basic specifications that constrain the efficiency of the cell: the portion of solar photons absorbed in the cell and the electric power generated per photon [88]. The first factor is determined by integrating the suitable AM quantity over the solar spectrum as well as the cut-off wavelength of the semiconductor absorber layer, the second efficiency factor implies that not all photon energy would be transformed to electric power and this process is related to the energy gap of the semiconductor.

Other factors that may affect the option of solar cells materials have included the following [88]:

- Absorption coefficient
- Contact resistance
- The abundance of raw materials
- Toxicity of materials
- Stability of materials and junctions

- Radiation resistance

These factors were considered when selecting different photovoltaic systems to evaluate the merits of various materials. Indeed, there is not one best choice, but different applications could even make one material more desirable than the other.

3.2 THE DEVICE STRUCTURE OF PIN 3C-SiC SOLAR CELL:

Figure (3.1) depicts a schematic representation of a PIN 3C-SiC solar cell which is proposed in the current work. The simulation of the current cell structure is based on the deposition of a p-type layer which is a 3C-SiC doped with Al with a band-gap of 1.139 eV, followed by a layer of intrinsic (3C-SiC) with a band-gap of 2.39 eV. The following layer is the buffer which consists of two layers the first is n-type 3C-SiC layer with a band-gap of 2.39 eV and the other is n-type layer of Cr-doped in 3C-SiC with a band-gap of 1.454 eV and finally the anti-reflection coating material that is SnO_2 n-type window layer with a band-gap of 3.6 eV.

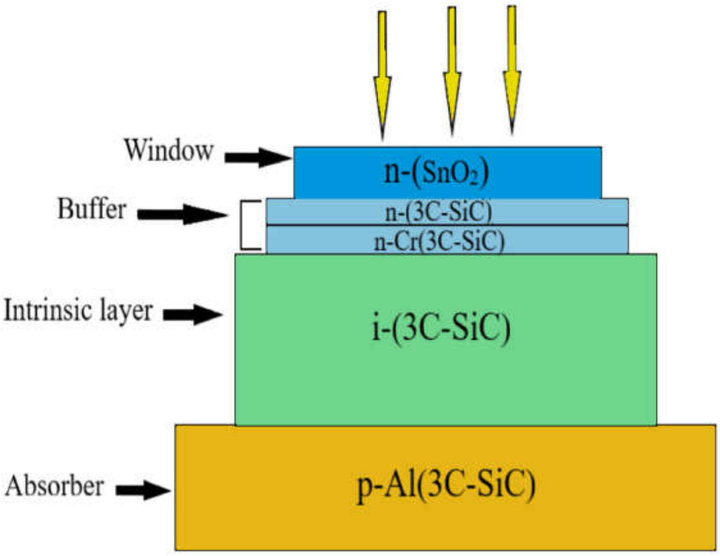

Fig. (3.1) PIN 3C-SiC solar cell structure.

3.2.1 THE SILICON CARBIDE (3C-SiC) MATERIAL

Silicon (Si) is the most widely used material in electronic devices, due to its elementary features that are optimal in a wide range of circumstances. Even so, there are restrictions with Si, such as the miniaturization process may demonstrate to make silicon unreliable to high temperatures. The potential to handle the required operating conditions was a major concern. This implies that devices that use silicon are not advantageous for operation at temperatures exceeding 250 ^{o}C. However, it can be possible to operate beyond this temperature with SiC due to its large band-gap [89].

Silicon carbide (SiC) is a wide band-gap semiconductor material that maintains excellent characteristics, including a wide band-gap (more than 2 eV), elevated breakdown voltage (3.0 mV/cm), high thermal conductivity (3.7 W/cm ^{o}C), lower carrier concentration and good oxide structure capability [89].

3.2.2 STRUCTURE OF SILICON CARBIDE (SiC)

SiC crystal is a compound of Si and carbon (C) with good bonding energy. This enables a quite strong tetrahedral covalent bond to be formed. Four atoms of silicon are combined with one carbon atom to form a SiC compound and the silicon-silicon, silicon-carbon spacing is 3.04 Å and 1.89 Å, respectively [90]. Silicon Carbide is available in 250 crystal structures recognized as polytypes, and the difference between them is the stacking. The most commonly used polytypes are 3C, 4H, 6H, 15R, the numbers 3, 4, 6, 15 indicating the layers necessary to form atomic topology (periodicity) and cubic (C), hexagonal (H), rhomboedral (R) representing a crystallographic categorization [89].

3C-SiC or β-SiC has a cubic phase zinc blend structure. The configuration of the 3C-SiC crystal, shown in figure (3.2). Si atoms occupy the vertex and face centers of the cubic lattice, while C atoms occupy the inner tetrahedral positions [91], whereas 4H, 6H, 15H has a wurtzite structure (hexagonal) [89].

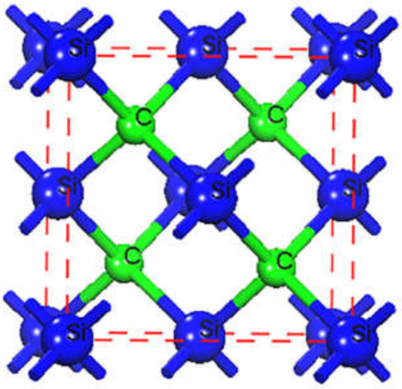

Fig. (3.2) 3C-SiC crystal structure [91].

3.2.3 PROPERTIES OF SILICON CARBIDE

Silicon carbide (SiC) is an indirect and wide band-gap material with quite excellent electrical properties such as high electron mobility and drift velocity saturation [92], in addition to high strength and durability, good chemical resistance, excellent thermal conductivity, and high thermal stability. These characteristics make it the perfect material for electrical devices used in high-power, high-temperature, and high-frequency environments [63]. The 3C-SiC However has specific important advantages that also make it extremely desirable for power devices. The major benefit of the cubic SiC polytype is the lower cost of manufacturing [57]. Due to the non-sensitivity of the SiC to long wavelengths of light ranging from most visible to infrared regions of the optical spectrum as a result of its indirect and wide band-gap [93]. It is therefore very necessary to find an effective method for improving its luminous efficiency. Doping has known to be an efficient technique of modifying the properties of SiC material. Table (3.1) illustrates the parameters of the 3C-SiC material.

Table (3.1) 3C–SiC parameter set [94].

Parameter	3C-SiC
α (eV K ^{1})	$0.66 \times 10\ ^{3}$
β (K)	1335
Electron affinity (eV)	3.83
Dielectric permittivity (relative)	9.720
N_C (300 K) (cm ^{3})	1.5536×10^{19}
N_V (300 K) (cm ^{3})	1.1639×10^{19}
μ_n electron mobility ($cm^2.V^{-1}\ s^{-1}$)	$6.500*10^{2}$
μ_h hole mobility ($cm^2.V^{-1}\ s^{-1}$)	4.000*10
Electron thermal velocity ($cm.s^{-1}$)	$1.000*10^{7}$
Hole thermal velocity ($cm.s^{-1}$)	$1.000*10^{7}$

3.3 AL-DOPED 3C-SiC ABSORBER LAYER

The absorber layer of the current cell is a 3C-SiC doped with Al to have p-type properties based on what was done by Lu in 2019 [91]. As for Al impurities in 3C-SiC, the band-gap is smaller than the un-doped system. The Al-doped 3C-SiC fermi energy level enters the valence band region figure (3.3), indicating that its metallicity rises, and the conductivity of the doped system increases with a massive rise in carrier concentration [95]. The number of valence bands levels increases dramatically and the band-gap slightly increasing to 1.454 eV [91]. Due to the smaller band-gap, the host peaks of the doped systems are moving in the direction of low energy, which means that a red-shift phenomenon occurs [91].

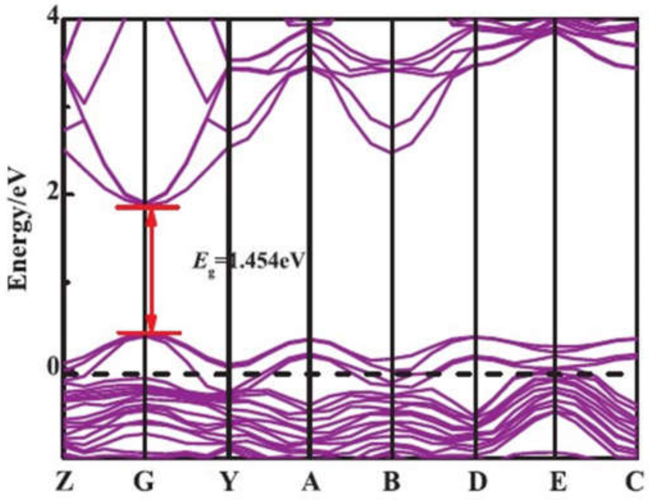

Fig. (3.3) Band structures of Al-doped 3C-SiC [91].

3.4 3C-SiC INTRINSIC LAYER

The main design of the cell is a PIN structure, quite common for inorganic optoelectronic devices [96], which is typically defined by an intrinsic (i) semiconductor layer, sandwiched between the p-doped and the n-doped semiconductor layer. Involving an intrinsic semiconductor as a central photoactive layer, providing the driving force for the separation of charges [96]. On the other hand, i-layer placement between p and n layers has to lead to higher wavelength response compared with PN junction [66]. The primary advantage of using PIN configuration over PN configuration is a better response of long-wavelength [66]. Photons enter deeply into the cell in the case of long-wavelength irradiation. However, only those electron-hole pairs that have been produced near the depletion region are contributing in the current generation. The depletion region of the PIN structure stretches throughout the intrinsic region and allows the pairs to be created profoundly inside the device; this enhances the quantum efficiency of the cell and therefore increases the J_{SC} [66]. In the present work, the intrinsic layer inserted between the absorber and the buffer is a 3C-SiC un-doped material with a band-gap of 2.39 eV, figure (3.4) shows the band structure of i-(3C-SiC). Moreover, the un-doped system has high absorption and reflectivity in ultraviolet regions (80–390 nm) and introduces the "Barrier Type" property, however, in a visible region (390–780 nm) the system utilizes low absorption coefficients and reflectivity, introducing the "Transparent Type" [91].

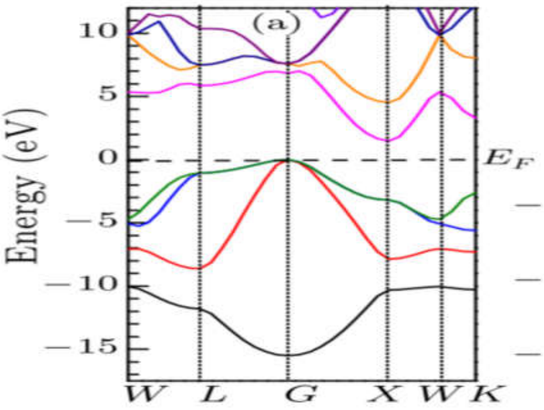

Fig. (3.4) Band structure of i-(3C-SiC) [97].

3.5 Cr-DOPED 3C-SiC AND n^+-(3C-SiC) BUFFER LAYERS

The buffer layer of the current cell consists of two thin layers of n-type 3C-SiC with a band-gap of 2.39 eV which is heavily doped to produce n^+ layer and 3C-SiC doped with Cr to have n-type properties based on what was done by Lu in 2019 [91]. The Cr-doped 3C-SiC band structure is shown in figure (3.5). It must be indicated that the fermi level enters the conduction band after doping, and then the Cr-doped 3C-SiC system shows a strong metallic property [91]. The Cr doping system has a relatively higher level of energy, that is, the amount of electron occupying energy is rising and the concentration of the carrier is increasing. Particularly in comparison to un-doped 3C-SiC, the Cr-doped 3C-SiC band-gap decreased to a certain extent (E_g=1.139 eV) [91]. The Cr doping system's band-gap lessens because the CB's shifting distance is larger than VB. The band-gap of the Cr-doped systems is lowered, which reduces the energy needed for the electrons from the excitation band to the conduction band, and the absorption band moves to a lower energy state relative to the Al-doped 3C-SiC system, i.e. the ability to respond to visible light is much higher than that of the Al-doped system [91].

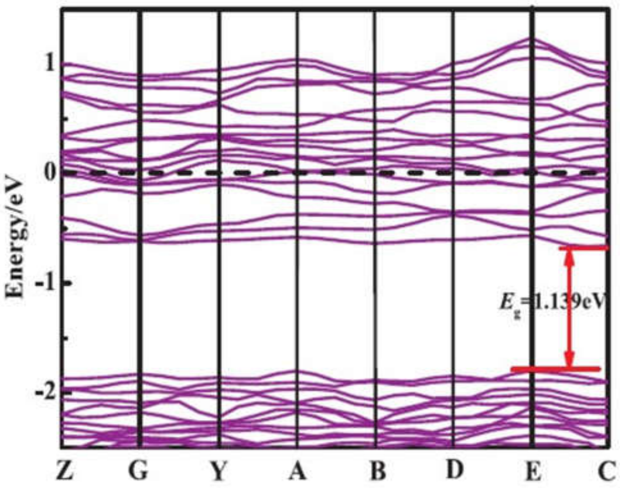

Fig. (3.5) Band structure of Cr-doped 3C-SiC [91].

3.6 WINDOW LAYER n-(SnO_2)

The top contact of the solar cell is recommended to be electrically conductive and transparent to allow solar radiation to flow through, a Transparent Conducting Oxide (TCO) was therefore used [98]. Electrical contacts are also needed to extract the current generated in the cell. Tin Oxide is the most widely utilized Transparent Conducting Oxide (TCO) for thin film solar cells, owing to its high conductivity, low reflectance, wide band-gap, and low sheet resistance [73]. It offers a high degree of conductivity and transmission. Another considerable attraction is its compatibility with low cost and mass production [98]. Figure (3.6) shows the structure of SnO_2, figure (3.7) is the energy band structure of SnO_2. The parameters set of SnO_2 is illustrated in the table (3.2).

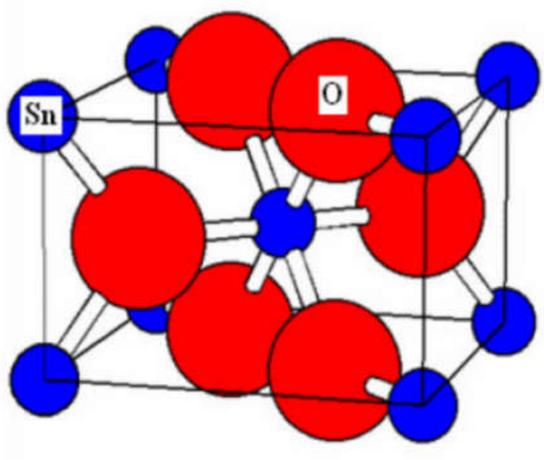

Fig. (3.6) SnO_2 Structure [73].

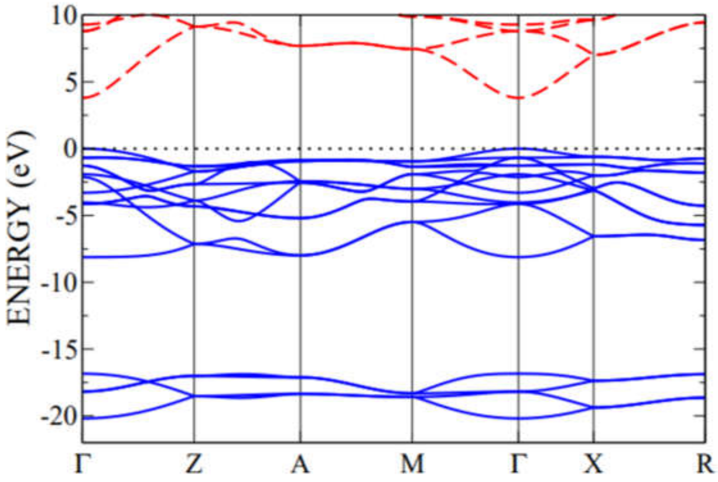

Fig. (3.7) energy band structure of bulk SnO_2 [99].

Table (3.2) n-SnO_2 parameters [100].

Parameters	n-SnO_2
E_g (eV)	3.6
Electron affinity (eV)	4.5
Dielectric permittivity (relative)	9
N_C (cm ^{3})	$2.2*10^{18}$
N_V (cm ^{3})	$1.8*10^{19}$
μ_n electron mobility ($cm^2.V^{-1}\ s^{-1}$)	100
μ_h hole mobility ($cm^2.V^{-1}\ s^{-1}$)	25
Electron thermal velocity ($cm.s^{-1}$)	$1*10^7$
Hole thermal velocity ($cm.s^{-1}$)	$1*10^7$

CHAPTER FOUR

RESULTS AND DISCUSSION

4.1 INTRODUCTION

The performance of solar cells relies on their design, material characteristics and manufacturing technology. Photovoltaic (PV) studies investigate enhanced cells over time, although the total process is complicated, expensive, and time-consuming. Numerical simulation is the best method for solar cell researchers, which helps to identify an optimized structure with decent parameters. As a result manufacturing difficulty, time and expense greatly decreased [101]. Simulation software is progressively used to offer knowledge into the details of the physical functioning of thin-film solar cells. Numerous modeling tools particular to PV devices were grown over the years. A number of these tools have reached maturity and are obtainable and free to the PV community.

4.2 SCAPS-1D SIMULATION SOFTWARE

The electrical solar cell simulation software SCAPS (Solar Cell Capacitance Simulator) is a development of the University of Gent by Prof. M. Burgelman et al. in the Department of Electronics and Information Systems and is available to the photovoltaic research community, it is a computer-based window application software written in C code [102]. In recent years, its abilities have been improved, such as band-gap grading and all other semiconductor properties [103]. SCAPS work on the use of basic semiconductor equations such as the Poisson equation, and Continuity equation for both of electrons, and holes. SCAPS computes the different profiles of the defined architectures, such as steady-state band diagram, carrier transport, and recombination, and bulk defects [102]. SCAPS can manage steady-state illumination by monochromatic light or through standard spectrum light (defaults are AM1.5 G and AM1.5D), figure (4.1) shows the SCAPS user interface.

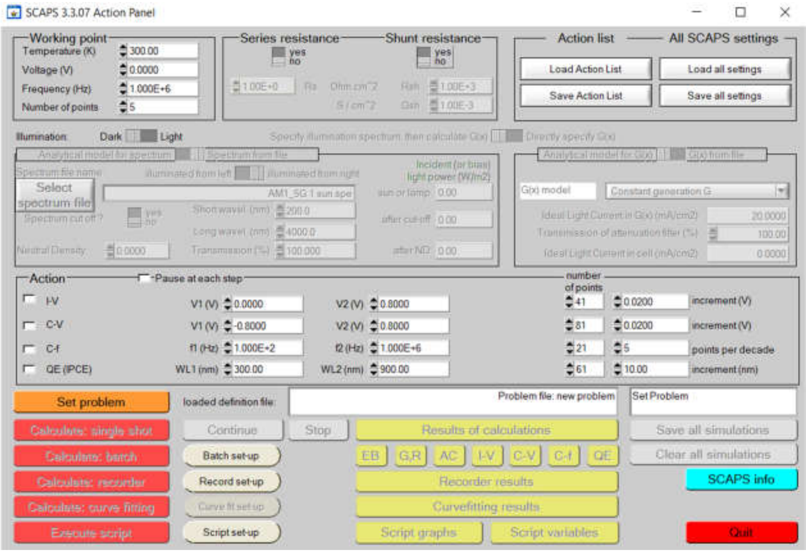

SCAPS 3.3.07 Action Panel

Working point
Temperature (K) 300.00
Voltage (V) 0.0000
Frequency (Hz) 1.000E+6
Number of points 5

Series resistance: yes / no; 1.00E+0 Rs Ohm.cm^2
Shunt resistance: yes / no; Rsh 1.00E+3 Ohm.cm^2; Gsh 1.00E-3 S/cm^2

Illumination: Dark / Light
Spectrum file name: AM1_5G 1 sun.spe
Spectrum cut off ? yes / no
Short wavel. (nm) 200.0
Long wavel. (nm) 4000.0
Neutral Density 0.0000
Transmission (%) 100.000
Incident (or bias) light power (W/m2): sun or lamp 0.00; after cut-off 0.00; after ND 0.00
G(x) model: Constant generation G
Ideal Light Current in G(x) (mA/cm2) 20.0000
Transmission of attenuation filter (%) 100.00
Ideal Light Current in cell (mA/cm2) 0.0000

Action ☐ Pause at each step

Action					number of points		
☐ I-V	V1 (V)	0.0000	V2 (V)	0.8000	41	0.0200	increment (V)
☐ C-V	V1 (V)	-0.8000	V2 (V)	0.8000	81	0.0200	increment (V)
☐ C-f	f1 (Hz)	1.000E+2	f2 (Hz)	1.000E+6	21	5	points per decade
☐ QE (IPCE)	WL1 (nm)	300.00	WL2 (nm)	900.00	61	10.00	increment (nm)

loaded definition file: Problem file: new problem
Set Problem

Fig. (4.1) The SCAPS user interface.

4.2.1 BASIC PRINCIPLE OF SOLAR CELL CAPACITANCE SIMULATOR (SCAPS) - 1D SCAPS

1-D SCAP discretized device with length L into N intervals and N+1 main grid points which would not be uniform as seen in figure (4.2) and solve numerically utilizing Poisson equations and continuity equations for each grid point with appropriate boundary conditions [102]. Three variables Ψ, E_{Fn}, and E_{Fp} are then solving at every grid point (node) from 1 to N+1, defined by solid lines under the light, voltage, and temperature conditions, and other variables such as electric field, carrier concentration, or trapped charges are defined, the recombination profiles, electron and hole current densities, as well as other data on transport, maybe gained [102]. Then the overall characteristic of the JV could then be acquired from $J(x) = J_n(x) + J_p(x)$. These are not just the JV characteristics, as well as the spectral response, QE, and the capacitance measurements CV and CF [102].

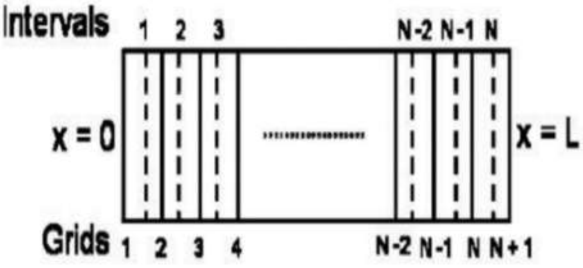

Fig. (4.2) Intervals and grids used in the numerical method. There are N intervals (dashed lines) and N +1 major grid points (solid lines) [102].

This software has been designed to effectively simulate the electrical properties (DC or AC) of thin-film solar heterojunction cells. The problem of solar cell simulation is stored in an ASCII file that can be read and entirely modified by the SCAPS graphical user interface [102]. This software is organized in several panels (or windows) where the user can select variables or show the results. It opens via an action panel in which the user can set an operating point (temperature, voltage, frequency, illumination) and an action list of the computations to be performed (JV, CV, CF, and QE) [102]. The user can navigate to a wide range of auxiliary panels also cannot only directly view initially measured data, but also band diagrams, electric field, carrier densities, partial recombination currents, i.e. one single mechanism. All measurements can be stored in ASCII format to be treated by the user using their favored set of tools.

4.2.2 GENERAL SCAPS WORKING POINT PARAMETERS

The working point clearly states parameters that are not modified in a measurement simulation and that are relevant to that measurement, figure (4.3) shows the working point parameter for SCAPS.

- The temperature T: relevant for all measurements. In SCAPS, only N_C (T), N_V (T), thermal velocity, thermal voltage KT, and all their derivatives will be the only factors that have an explicit temperature dependence; that should be entered according to the correlating material parameters for each T [102].
- Voltage V: is discarded in JV and CV simulations. It is the dc-bias voltage in the CF simulation and the QE (λ) simulation. SCAPS begins at 0 V and continues at the working point voltage in a sequence of iterations that user should also specify [102].
- Frequency f: is discarded in JV, QE (λ), and CF simulations. It is the frequency where the CV evaluation is modeled [102].
- The illumination: is used for all measurements. It defines the bias light requirements for the QE (λ) measurement. The fundamental settings are dark or light, the decision of the illuminated side, the selection of the spectrum. A single sun (= 1000 W.m^{-2}) illumination with the air mass 1.5. The global spectrum is the default, but there is a wide range of monochromatic light and spectra for specialized simulation [102].

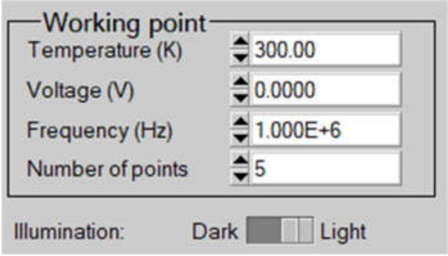
Working point
Temperature (K) 300.00
Voltage (V) 0.0000
Frequency (Hz) 1.000E+6
Number of points 5

Fig. (4.3) General working point parameter.

4.3 REFERENCE CELL

In the current study, the proposed solar cell PIN structure consists of five layers; the absorber is a p-(3C-SiC) doped with Al with a band-gap of 1.454 eV, an intrinsic layer of (3C-SiC) with a band-gap of 2.39 eV. Two buffers are used an n$^+$(3C-SiC) with a band-gap of 2.39 eV and an n-(3C-SiC) doped with Cr with a band-gap of 1.139 eV and a window layer of SnO_2 with a band-gap of 3.6 eV. The cell structure is shown in figure (4.4).

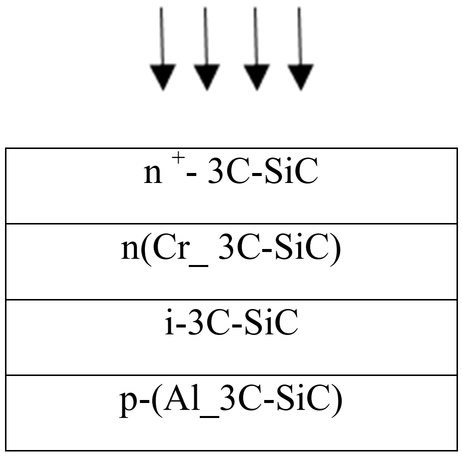

Fig. (4.4) Structure of the PIN 3C-SiC solar cell used in the numerical simulation

In the current design of the solar cell, material parameters such as thickness and doping density must have initial values. These initial values have to be in a reasonable range for each layer to obtain a structure with excellent performance and relatively low cost. The reference cell is a structure with initial inputs that are selected according to the layered role in the cell and to the acceptable useable range. The output parameters as well as quantum efficiency will be the baseline output of the cell, and then a parametric study will occur on this reference cell.

The present study includes the effect of thickness and doping density for each layer of the reference cell on the photovoltaic parameters (short-circuit current density J_{SC}, open-circuit voltage V_{OC}, fill factor FF, and the efficiency η), besides the physical characteristics or the impact of the environmental conditions on the cell output which represented by the temperature and light intensity. To eliminate the reliance of the solar cell area, the short-circuit current density (J_{SC} in mA.cm^{-2}) is more popular than the short-circuit current I_{SC}. Table (4.1) includes the thickness and the doping density for all the layers as inputs of the reference cell. The defects of each layer were fixed on the values given in appendix (B).

Table (4.1) Initial values of the 3C-SiC solar cell.

layer	Doping density (cm^{-3})	Thickness (µm)
p-Al(3C-SiC)	N_a=10^{13}	1
i-(3C-SiC)	10^{10}	1
n-Cr(3C-SiC)	N_d=10^{13}	0.05
n^+(3C-SiC)	N_d=10^{19}	0.05
n-SnO_2	N_d=10^{12}	0.1

4.4 SIMULATION RESULTS OF THE REFERENCE CELL

The JV curve of the reference cell with initial values is shown in figures (4.5) and (4.6) which include the dark and light cases, where (V_{OC} = 0.2524 V, J_{SC} =34.66 mA.cm^{-2}, FF = 41.21% and η = 3.61%). Figure (4.7) shows the quantum efficiency response with the wavelength of the cell with the initial values. The peak response of the cell is (50 %) at the wavelength from (800 to 900 nm). The range drops from (800 nm to approximately 420 nm) due to the recombination processes in the interfaces from (55 % to 23 %) and starts to elevate again from (23 % to less than 40 %) in the range of wavelengths from (less than 400 nm to 300 nm).

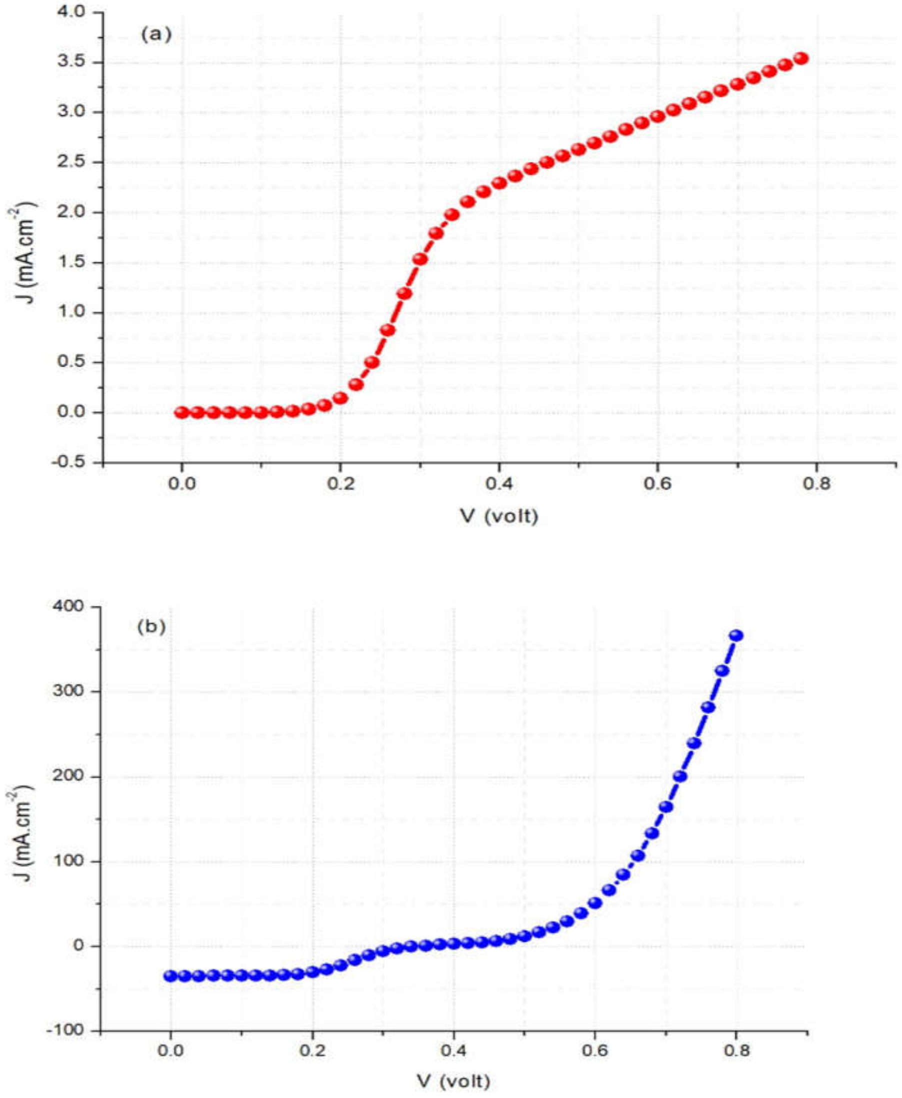

Fig. (4.5) JV curve of the reference cell (a) Dark (b) Light.

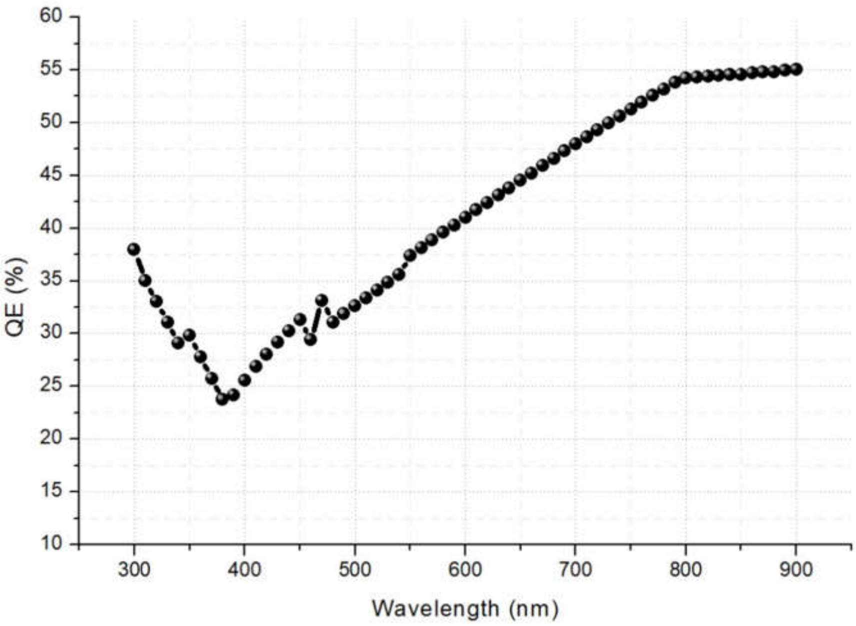

Fig. (4.6) Quantum efficiency of the reference cell.

The energy band structure of the 3C-SiC cell is shown in figure (4.7) under AM 1.5 illumination of 1000 W.m^{-2}, 0 V bias, and thermodynamic equilibrium with the constant fermi level (E_f) through the cell.

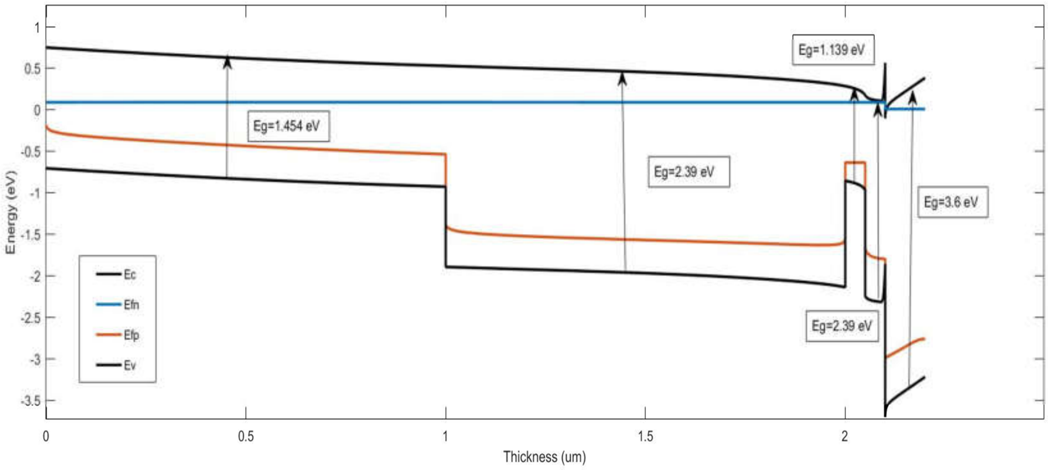

Fig. (4.7) Energy band structure of 3C-SiC cell with initial values.

4.5 PARAMETRIC STUDY

To have a solar cell with the best performance, a parametric study on the major parameters of the cell should be carried out. The study begins by taking the doping density as the first parameter to be changed within a reasonable range for each cell layer until the best cell performance is achieved. The same thing happens on the thickness parameter for all layers.

4.5.1 EFFECT OF CARRIER CONCENTRATION

Each layer of the cell must have a certain doping density to produce an optimum power conversion efficiency. The parametric study starts by keeping the thickness of the whole layers constant at the initial values and start varying the doping density in a single layer independently and keeping the doping of the other layers constant at the initial values to study its effect on the cell performance.

- **ABSORBER LAYER P-Al(3C-SiC)**

In this section, the simulation software will be used to investigate the effect of the carrier concentration of the absorber layer by changing the doping density of the acceptor N_a from 10^{10} to 10^{15} cm^{-3}, while the doping density of the other layers was kept at the initial values. The simulation results are listed in table (4.2).

Table (4.2) The impact of the carrier concentration variation in the absorber on the output parameters.

N_a (cm^{-3})	V_{OC} (v)	J_{SC} (mA.cm^{-2})	FF %	η %
10^{10}	0.1335	29.86	21.72	0.87
10^{11}	0.1410	30.81	22.77	0.99
10^{12}	0.1826	33.68	29.92	1.84
10^{13}	0.2524	34.66	41.21	3.61
10^{14}	0.3440	35.05	51.59	6.22
10^{15}	0.7351	36.32	70.16	18.73

The results in figure (4.8) shows that, changing the doping density in the absorber layer plays a significant role in enhancing the performance of the cell, resulting in a dramatic increase in efficiency from 0.87 to 18.73 % with the doping density increasing from 10^{10} to 10^{15} cm^{-3} respectively. These results give an indication that the optimum doping density for this layer is at $N_a=10^{15}$ cm^{-3}. With an increase in the carrier concentration, the saturation process of the cell increases as does the V_{OC} [103]. However, increasing the doping density more than $N_a=10^{15}$ cm^{-3}, recombination at the interface becomes large and the possibility of the accumulation of photo generated electrons reduced, and as a result a reduction in the current and conversion efficiency [103]. Increasing carrier concentration more than the optimum value also leads to a reduction of the band-gap and the minority carrier lifetime as well [104][105]. Figure (4.9) shows the enhancement of the shape of the JV curve with increasing the absorber layer doping density.

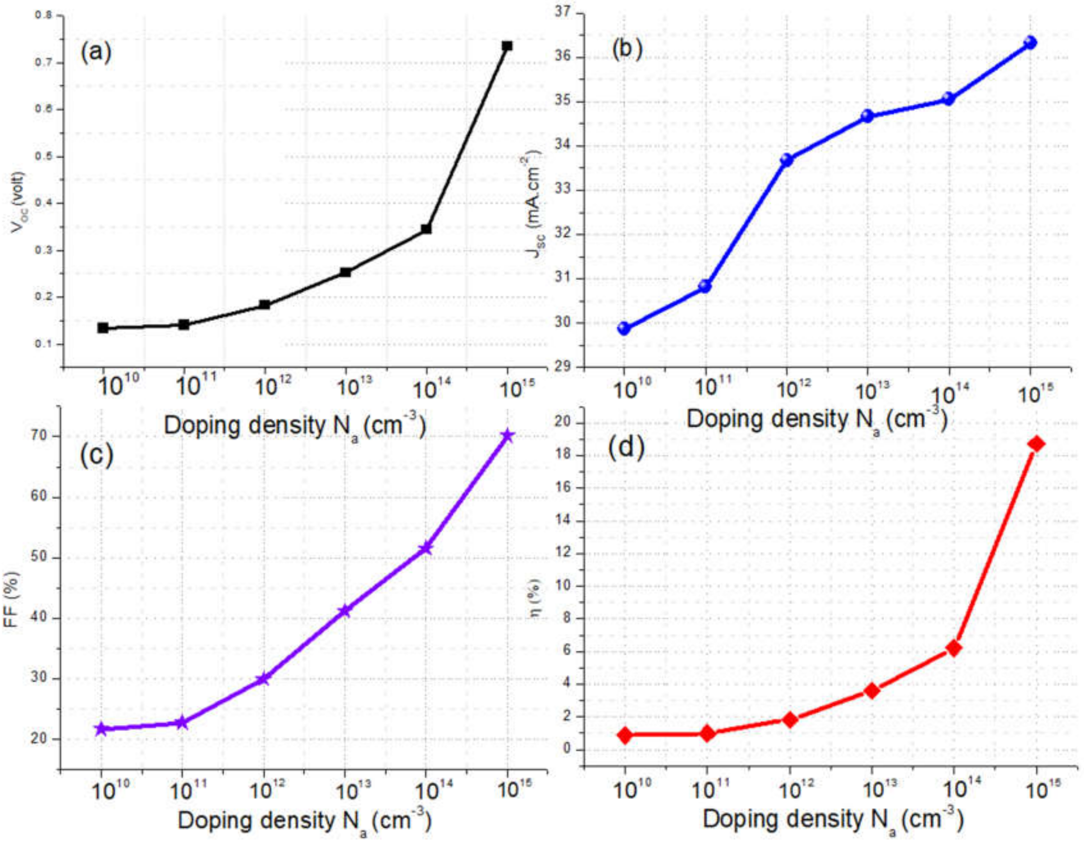

Fig. (4.8) The impact of doping concentration variation in the absorber layer on the (a) Open-circuit voltage (V_{OC}) (b) Short-circuit current density (J_{SC}) (c) Fill Factor (FF) (d) Efficiency (η).

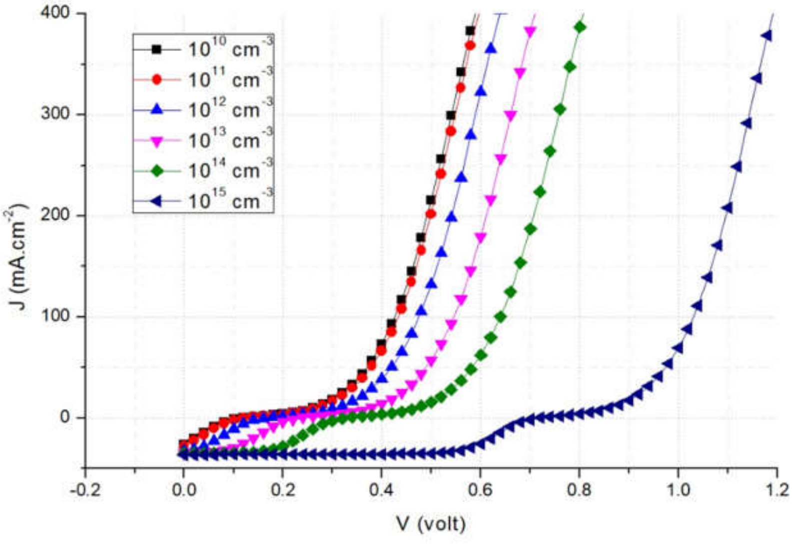

Fig. (4.9) The impact of carrier concentration variation in the absorber layer on the JV shape of the cell.

- **BUFFER LAYERS n$^+$(3C-SiC) and n-Cr (3C-SiC)**

The doping density N_d of the n$^+$(3C-SiC) layer was varied from 10^{18} to 10^{22} cm^{-3}, while keeping the doping density in the absorber layer at the previous optimum value (i.e. N_a=10^{15} cm^{-3}), the doping density of the other layers are kept at the initial values. It is found from the results shown in figure (4.10), that the carrier concentration in the buffer layer increases from 10^{18} to 10^{22} cm^{-3} a power conversion efficiency of the cell increases from 16.84 to 21.52%, while J_{SC} increases slightly from 36.12 to 36.47 mA.cm^{-2} and the V_{OC} is almost constant at 0.735 V. The effect of the carrier concentration in this layer on the output of the cell is not as significant as the carrier concentration effect in the absorber. The optimum doping density in this layer is at N_d =10^{22} cm^{-3} that produces an efficiency of 21.44 %. The main role of the top n$^+$ layer is to enhance the absorption in the UV region of the spectrum and consequently enhance the performance of the cell [106]. Figure (4.10) shows the effect of doping density in the n$^+$ layer on the output parameters, while figure (4.11) shows the effect of doping variation in the n$^+$ layer on the JV curve.

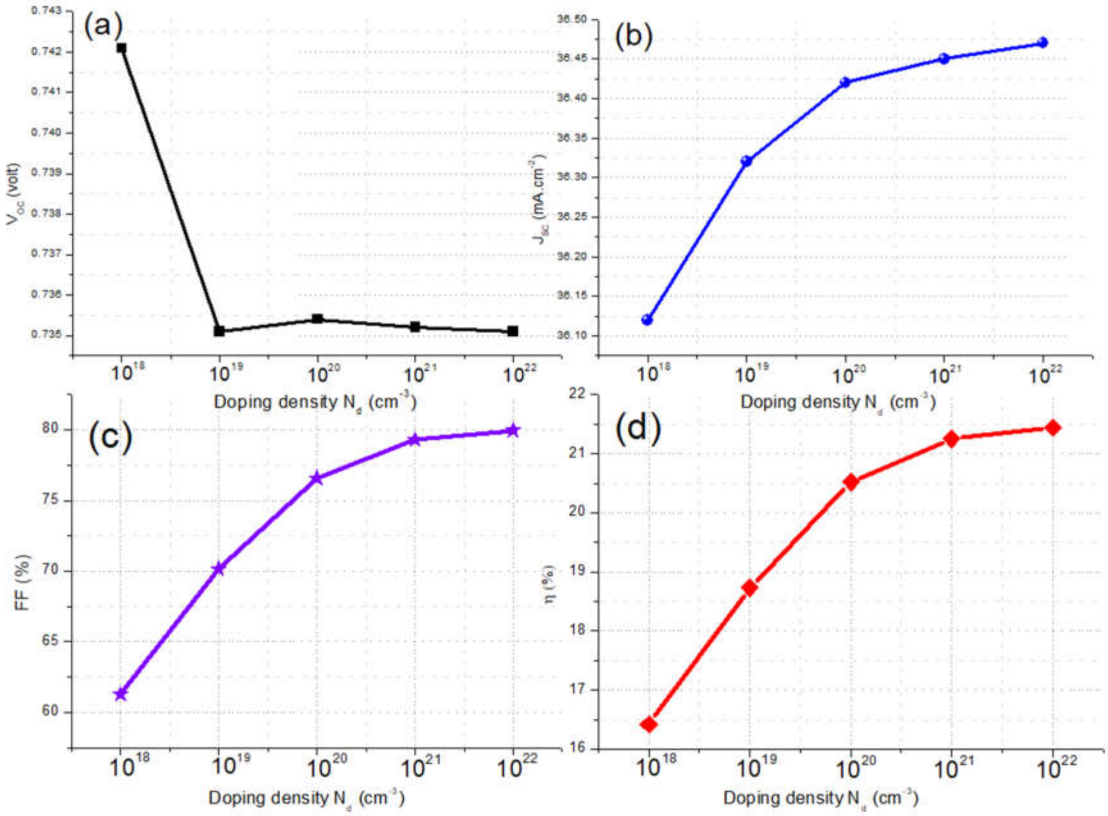

Fig. (4.10) The impact of doping concentration variation in the n^+ on the (a) Open-circuit voltage (V_{OC}) (b) Short-circuit current density (J_{SC}) (c) Fill Factor (FF) (d) Efficiency (η).

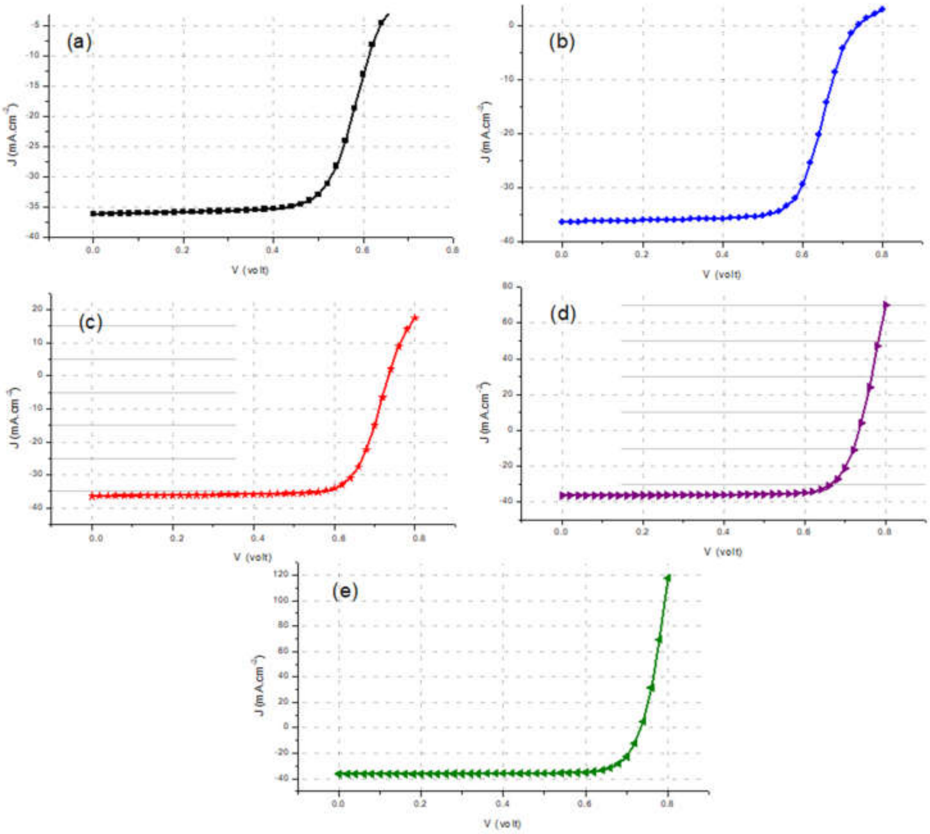

Fig. (4.11) The impact of doping concentration variation in the n^+ on the JV curve of the cell at different values of N_d (a) 10^{18} cm^{-3} (b) 10^{19} cm^{-3} (c) 10^{20} cm^{-3} (d) 10^{21} cm^{-3} (e) 10^{22} cm^{-3}.

The effect of carrier concentration will be investigated on the second buffer layer n-Cr (3C-SiC), keeping the donor concentration in the n^+ layer at N_d=10^{22} cm^{-3}, the acceptor concentration in the absorber at N_a=10^{15} cm^{-3}, and other layers at their initial values. It is obvious from the results that, for donor concentration from (10^{13} to 10^{15} cm^{-3}) the efficiency of the cell does not elevate and stays at (21.44 %) and the values of V_{OC}, as well as J_{SC}, remain constant at 0.7351 V and 36.47 $mA.cm^{-2}$ respectively. The reason behind this is that the donor density in the buffer should not be less than the acceptor, due to the sever recombination in the interface that will occur [107]. Since, the acceptor concentration of the p-(3C-SiC) was at the value (10^{15} cm^{-3}), as the donor density equal to that value, the electron traps decreases to a lower level at the interface, which finally makes the J_{SC} increase and consequently the efficiency. As the donor concentration increased up to 10^{19} cm^{-3}, a moderate increment of J_{SC} from 36.47 to 37.70 mA.cm^{-2} and efficiency from 21.44 to 22.69 %, which leads to an additional decrement of electron traps in the interface. However, beyond the value of 10^{19} cm^{-3} is not a good choice for a semi-conductive material, as it can be turned into a metallic regime due to 'Mott transition' rule [107]. Therefore, in this study, the donor concentration of 10^{19} cm^{-3}can be considered as an optimum value for n-(Cr-3C-SiC) buffer layer which gives an efficiency of 22.69 %. Figure (4.12) shows the effect of carrier concentration variation on the fill factor and the efficiency of the cell.

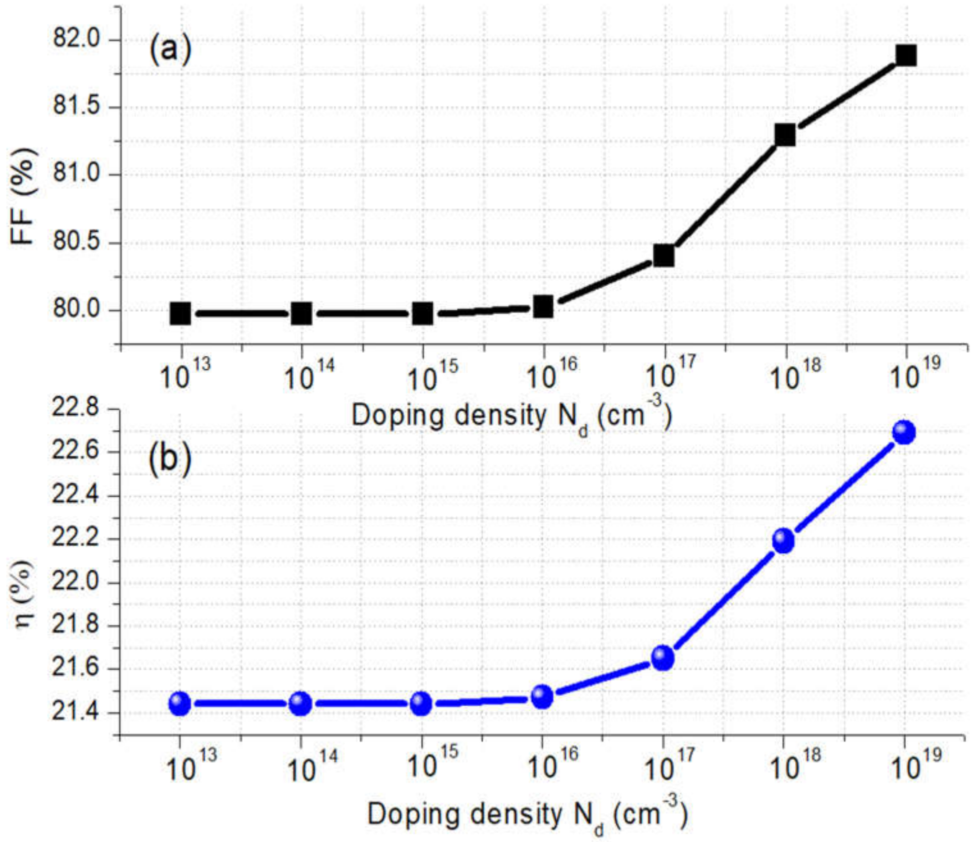

Fig. (4.12) The impact of doping concentration variation in the n-Cr (3C-SiC) on the (a) Fill Factor (FF) (b) Efficiency (η).

The variation of carrier concentration in the n-Cr (3C-SiC) buffer layer has a noticeable impact on the quantum efficiency response especially in the wavelength range from 600 to 900 nm. It starts to increase slightly with doping at $N_d > 10^{17}$ cm^{-3} and reaches the peak response at $N_d \sim 10^{19}$ cm^{-3} at wavelengths range 800 to 900 nm as shown in figure (4.13).

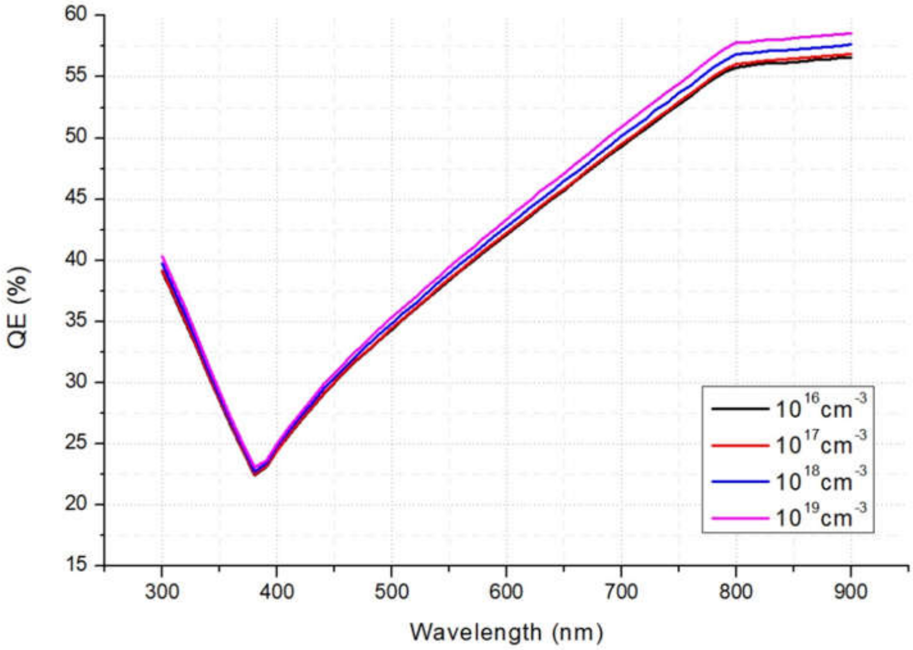

Fig. (4.13) The impact of doping concentration variation in the n-Cr (3C-SiC) on the QE.

The overall impact of the carrier concentration variation in the intrinsic layer of 3C-SiC and the SnO_2 layer is not obvious i.e. does not have a high impact on cell performance. The optimum carrier concentration of the i-(3C-SiC) is 10^{15} cm^{-3} and for SnO_2 is $N_d=10^{18}$ cm^{-3}, which produces a power conversion efficiency of 22.78 %, V_{OC} of 0.7354 V, J_{SC} of 37.70 $mA.cm^{-2}$ and fill factor of 82.18 %.

As a summary of the parametric study on the carrier concentration of each layer of the reference cell, the optimum doping densities that give the better performance are for p-Al(3C-SiC) layer is $N_a=10^{15}$, for n^+(3C-

SiC) is $N_d=10^{22}$, for n-Cr(3C-SiC) is $N_d=10^{19}$, for SnO_2 is $N_d=10^{18}$, and carrier concentration of 10^{15} cm^{-3} for i-(3C-SiC).

4.5.2 EFFECT OF THICKNESS

This part of the simulation will consider the thickness as the subject of study. By keeping the doping density for all the layers at the optimum values mentioned before, the second step is varying the thickness of each layer independently to get the best performance of the structure. This process is achieved for the whole layers of the cell until reaches the best conversion efficiency and better response.

- **ABSORBER LAYER p-Al(3C-SiC)**

The influence of the absorber layer thickness on the cell performance will investigate in this part of the study. The simulation achieved by varying the thickness of absorber from 1 μm to 3 μm with a step of 0.5, while the thickness of other layers is kept at their initial values. It is clear from the results that the increase in the thickness of the absorber layer produces a slight increment in V_{OC} from 0.73 to 0.76 V and the fill factor from 82.18 to 83.94 % that in turn elevates the efficiency from 22.78 to 24.14 %, while the short-circuit current density is almost constant at 37.7 mA.cm^{-2}. This can be ascribed to the increase in the collection of photo-generated carriers before recombination that improves efficiency. However, the absorber layer thickness cannot be increased excessively, the thickness that is more than 3 μm makes the V_{OC}, J_{SC}, FF, and the efficiency only increase marginally and it can be considered almost saturated. Further increase in the thickness of this layer will cause a part of the incoming photons being absorbed deeply far from the space-charge region, and the generated carriers cannot reach the depletion region during their lifetime and they will be recombined. In other words, the increase in the absorber layer thickness makes the possibility of increasing the bulk recombination [108]. Thus, it can be considered that the optimum absorber layer thickness is 3 µm which produces an efficiency of 24.14 %. Figure (4.14) shows the effect of absorber layer thickness on the fill factor and the efficiency of the cell, and figure (4.15) shows the JV variation with thickness for the current layer.

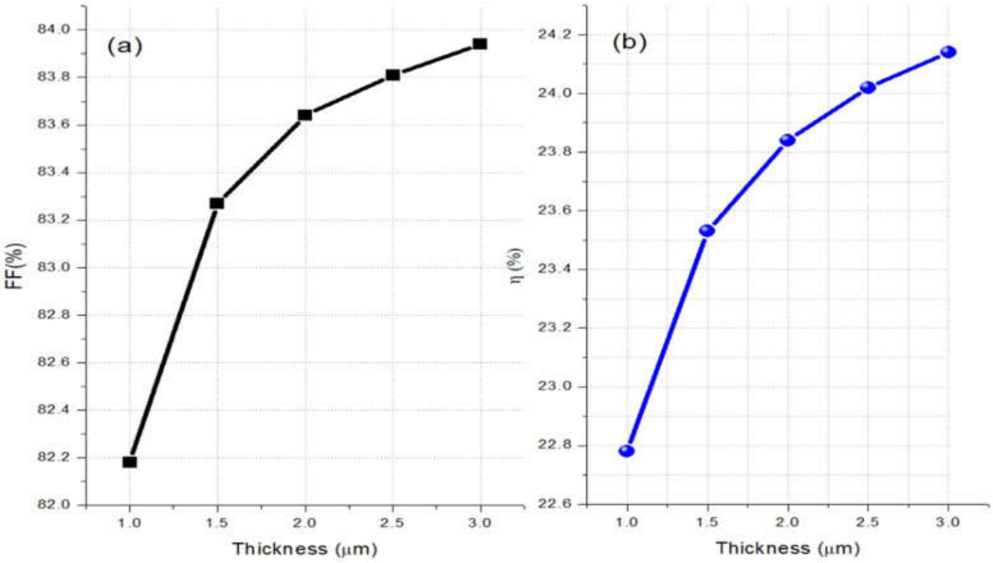

Fig. (4.14) The impact of thickness variation in the absorber layer on the (a) Fill Factor (FF) (b) Efficiency (η).

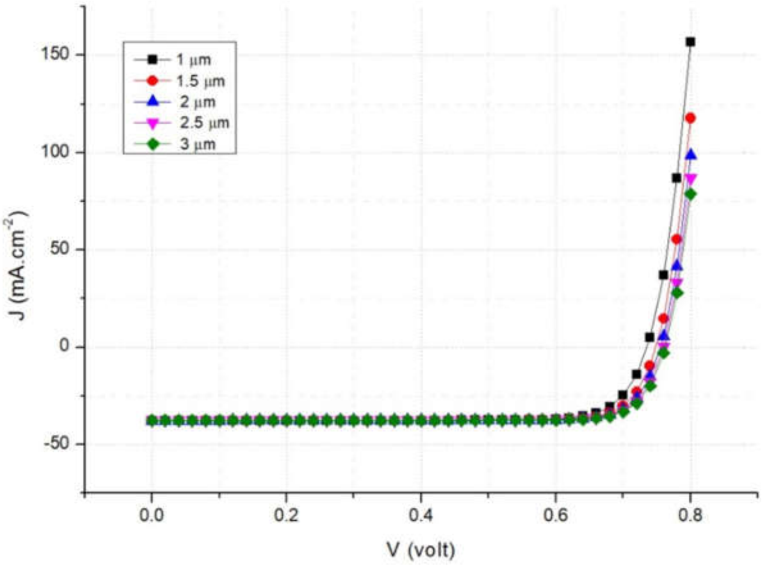

Fig. (4.15) The impact of thickness variation in the absorber layer on the JV curve of the cell.

- **INTRINSIC LAYER i-(3C-SiC)**

The second part of thickness tailoring, the thickness of the absorber layer is kept at 3 µm, other layer thicknesses kept at their initial values, and the intrinsic layer thickness is varying from 1 to 2.5 µm in a step of 0.5 to investigate the influence of this layer thickness variation on the cell performance. The simulation results depicted are in the table (4.3). It is so clear that the role of this layer thickness is the most dominant. Increasing the intrinsic layer thickness elevates the efficiency excessively from 24.14 to 34.45%. The main role of this layer is that it enlarges the width of the space-charge region, where the creation of electron-hole pairs occurs due to photons absorption, thus an increase in J_{SC} will follow, and consequently the efficiency increase, while the V_{OC} is almost constant. The results imply that as the thickness of the active layer increases from 1 to 2.5 µm, J_{SC} increases from 37.73 to 54.27 mA.cm^{-2} due to an increase in the photo-generated carriers, thus the efficiency also increases. Figure (4.16) shows the impact of intrinsic layer thickness on the output parameters of the cell.

Table (4.3) The impact of the thickness variation of the intrinsic layer on the output parameters.

Thickness (µm)	**V_{OC} (v)**	**J_{SC} (mA.cm^{-2})**	**FF %**	**η %**
1	0.7623	37.73	83.94	24.14
1.5	0.7653	46.17	83.56	29.53
2	0.7668	51.24	83.17	32.68
2.5	0.7678	54.27	82.68	34.45

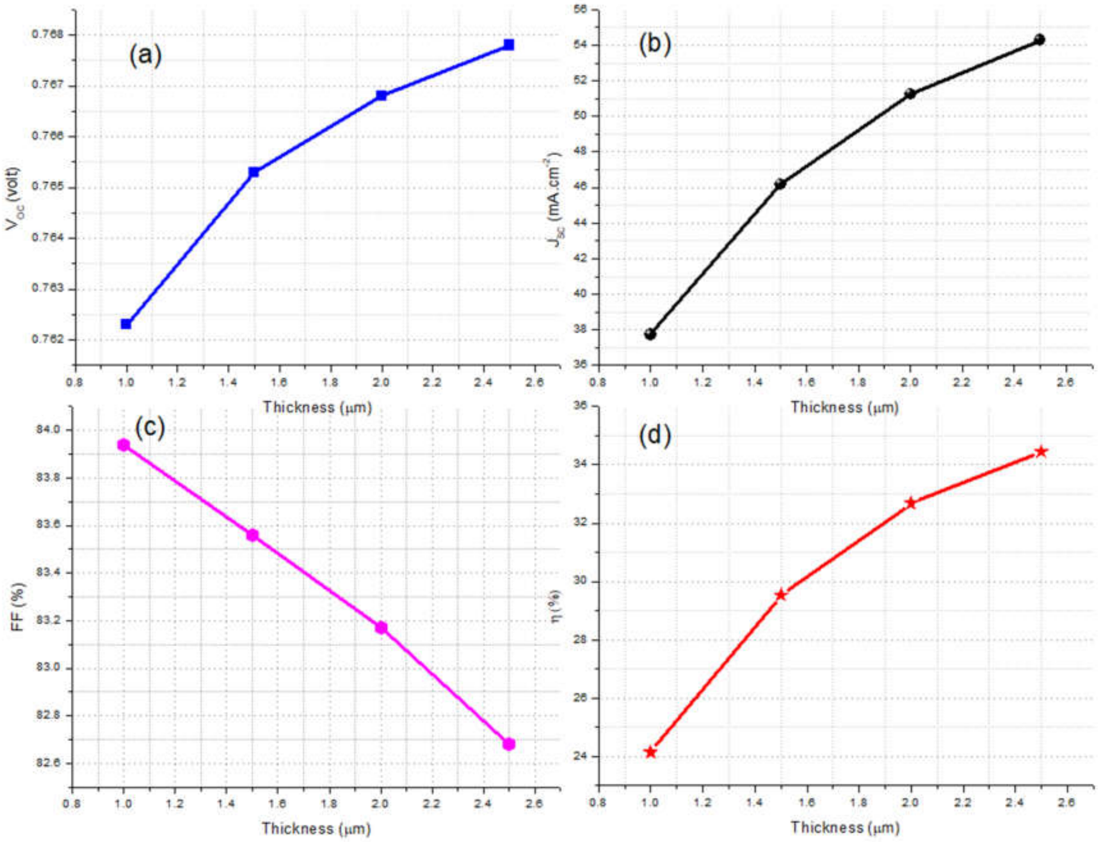

Fig. (4.16) The impact of thickness variation in the i-(3C-SiC) on the (a) Open-circuit voltage (V_{OC}) (b) Short-circuit current density (J_{SC}) (c) Fill Factor (FF) (d) Efficiency (η).

The FF is the percentage of the collected pairs compared to created, therefore when the intrinsic layer thickness increases, a general decrease in the FF due to the generation-recombination balance [109]. On the other hand, increase the thickness of the intrinsic layer will add additional series resistance, which in turn reduces the fill factor. As well to that, when the intrinsic layer becomes thicker than the diffusion length of photo-generated carriers, most of the generated carriers will be trapped in this layer and it becomes difficult for these carriers to reach the electrodes. Thus, the optimum thickness of this layer is 2.5 μm, which gives the highest power conversion efficiency and the most enhanced quantum efficiency as shown in figure (4.17), but the cell still needs optimization on the other layers thickness to reduce the very high value of the J_{SC} and keep the efficiency at a high value.

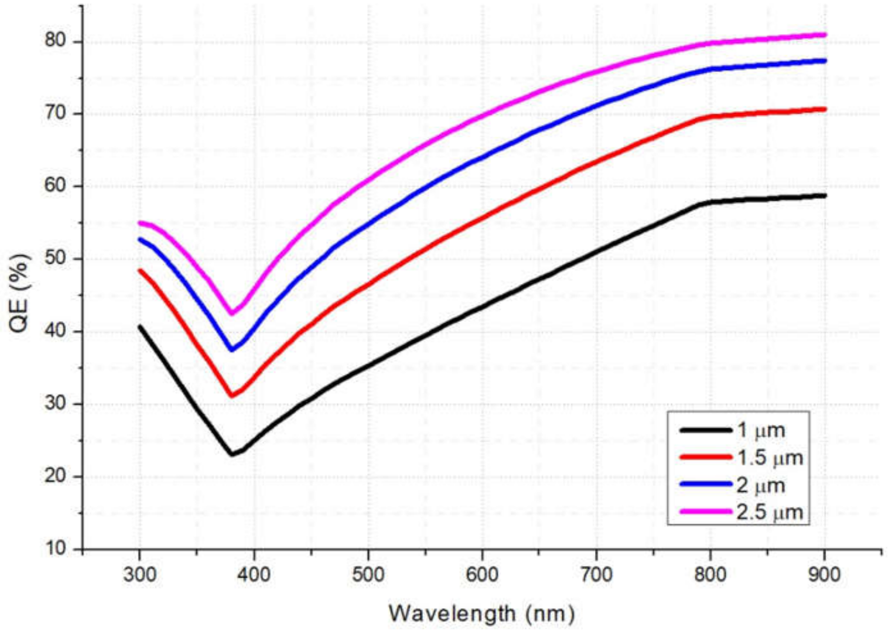

Fig. (4.17) The impact of intrinsic layer thickness variation on the QE.

Figure (4.17) shows the improvement in the QE of the cell with increasing intrinsic layer thickness from 1 to 2.5 μm and the improvement include the whole range of the wavelength from 300 to 900 nm, which implies the significant role of this layer in the enhancement of the cell performance. Figure (4.18) also shows the improvement in the JV curve which is related to the increment in the short-circuit current density with a thickness variation of the current layer.

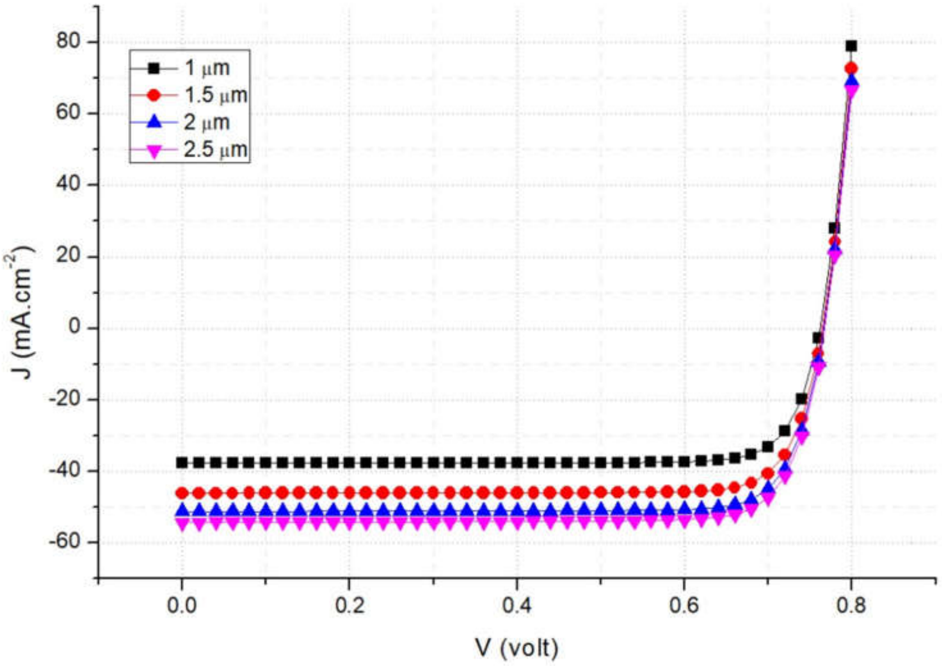

Fig. (4.18) The impact of intrinsic layer thickness variation on the JV curve shape of the cell.

- **WINDOW LAYER n-SnO2**

Every solar cell must have anti-reflecting coating material with optimum thickness to reduce reflection losses and enhance the performance of the cell. To reduce the high short-circuit current that produces due to using a relative thick intrinsic layer, a thickness of anti-reflecting coating material that is more than 0.1 µm is required to increase the absorption in this layer and reduce the number of photons reach the absorber and consequently the photo-generated carriers, and this will yield a decrease the short-circuit current. The simulation performed by varying the thickness of this layer from 0.1 to 0.2 µm in a step of 0.025. Figure (4.19) shows the impact of anti-reflecting layer thickness on J_{SC} and efficiency. It is so clear from the results that the increase in the thickness of this layer has a direct effect on the reduction of J_{SC} from 54.27 to 50.24 mA.cm^{-2}, while no impact on the V_{OC} was observed, which was kept constant at 0.767 V. As shown in figure (4.19 b) the change in J_{SC} affect on the efficiency. Thus increasing the thickness of anti-reflecting layer more than the optimum value that is in the range of 100 to 200 nm degrades the efficiency and causes the SnO_2 to lose its feature as anti-reflecting material. The optimum thickness value for this layer is 0.2 μm.

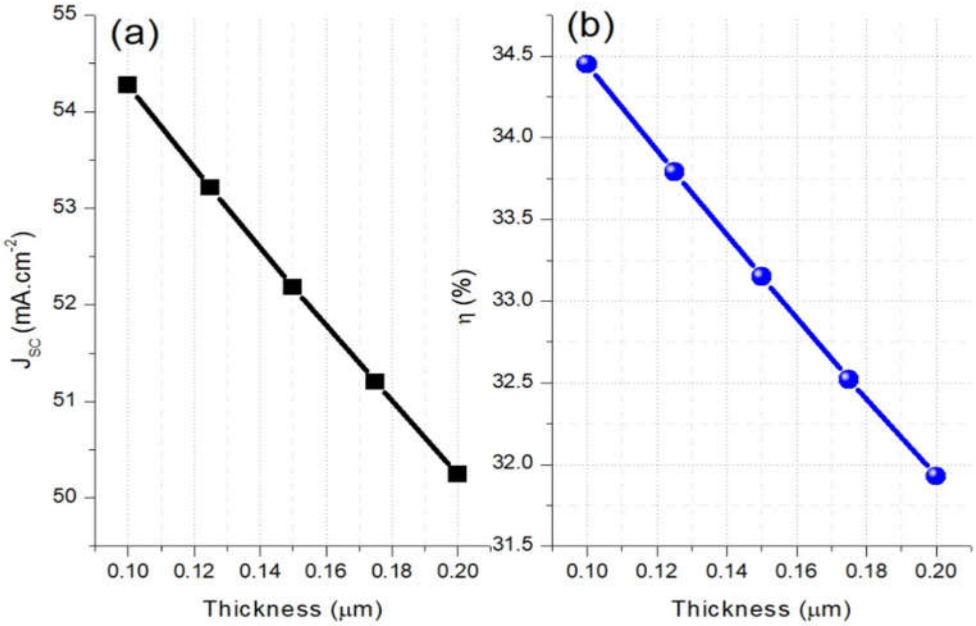

Fig. (4.19) The influence of SnO_2 layer thickness on the (a) Short-circuit current density (J_{SC}) (b) Efficiency (η).

Figure (4.20) shows the influence of increasing the thickness of the window layer in reducing the quantum efficiency of the cell. Thus, there must be a trade-off between the cell parameters i.e. reducing the short-circuit current to the detriment of efficiency degradation, so a precise decision must be taken in choosing the thickness of each layer. Figure (4.21) shows a slight change in the shape of JV curve in the current step of the simulation.

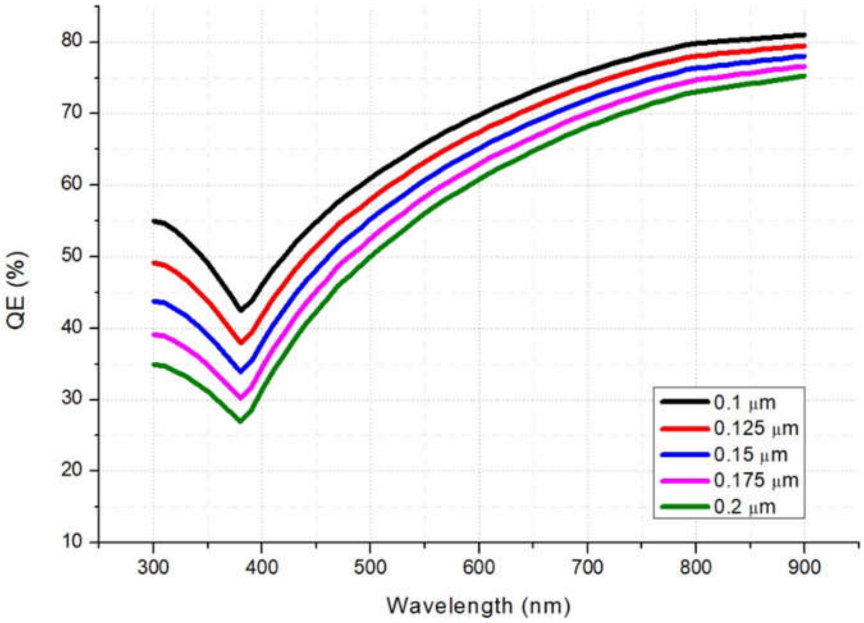

Fig. (4.20) The influence of SnO_2 thickness variation on the QE of the cell.

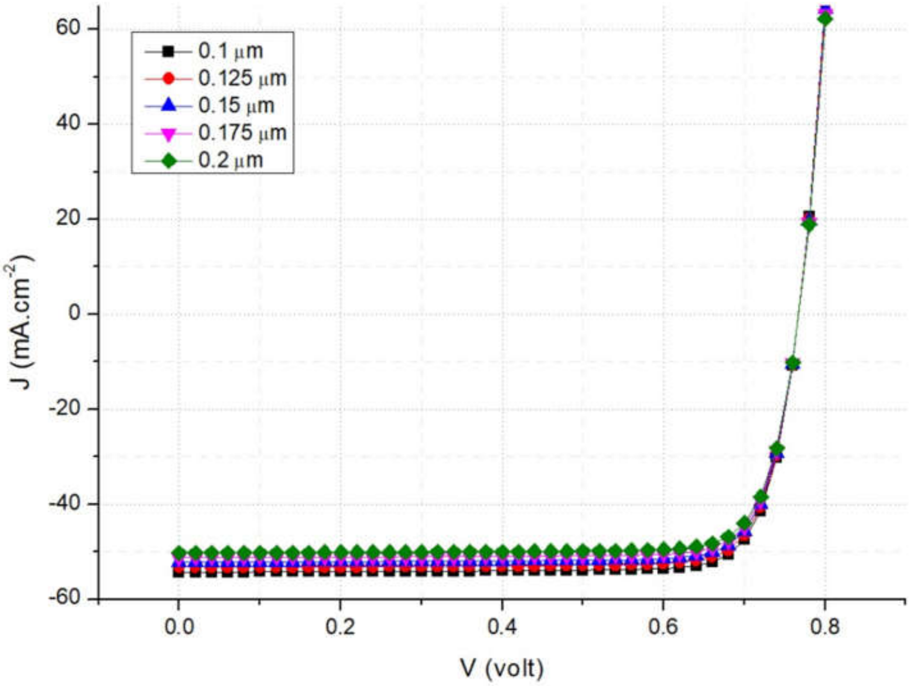

Fig. (4.21) The influence of SnO_2 layer thickness on the JV curve.

- **BUFFER LAYER n^+ (3C-SiC) AND n-Cr(3C-SiC)**

In this part of the simulation, the effect of the two buffer layers thickness on solar cell performance is investigated. The n^+ layer thickness is varying from 0.05 to 0.1 μm in a step of 0.01, while the thickness of the absorber is kept at 3 μm, the intrinsic is at 2.5 μm, and the window layer is at 0. 2 μm**.** Table (4.4) depicts the output parameters response with n^+ layer thickness variation. The results show that the increase in the buffer thickness causes a reduction in the cell parameters. However, the reduction is not so noteworthy for the efficiency as that for J_{SC} as shown in figure (4.22), while V_{OC} is almost constant at 0.768 V. This result can be attributed to the photon loss that occurs in a thick buffer layer. That is, as the buffer layer thickness is increased, more incident photons will be absorbed by the n^+ (3C-SiC) layer, which will affect a decrease of photons that can be capture by the absorber layer. Therefore, the absorbed photons will yield less electron-hole pairs, thus decreasing the quantum efficiency of the cell. Although the higher performance of the cell obtained at thinner buffer layers but too thin buffer layer may result in leakage current, so the optimized and the preferred buffer layer thickness in this cell is 0.1 μm, which gives the minimum short-circuit current density and still produce a good efficiency.

Table (4.4) The output parameters with n^+ layer thickness variation.

Thickness (μm)	**V_{OC} (v)**	**J_{SC} (mA.cm^{-2})**	**FF %**	**η %**
0.05	0.7679	50.24	82.74	31.93
0.06	0.7679	49.72	82.75	31.60
0.07	0.7680	49.20	82.75	31.27
0.08	0.7680	48.69	82.76	30.95
0.09	0.7680	48.19	82.77	30.63
0.1	0.7680	47.69	82.78	30.32

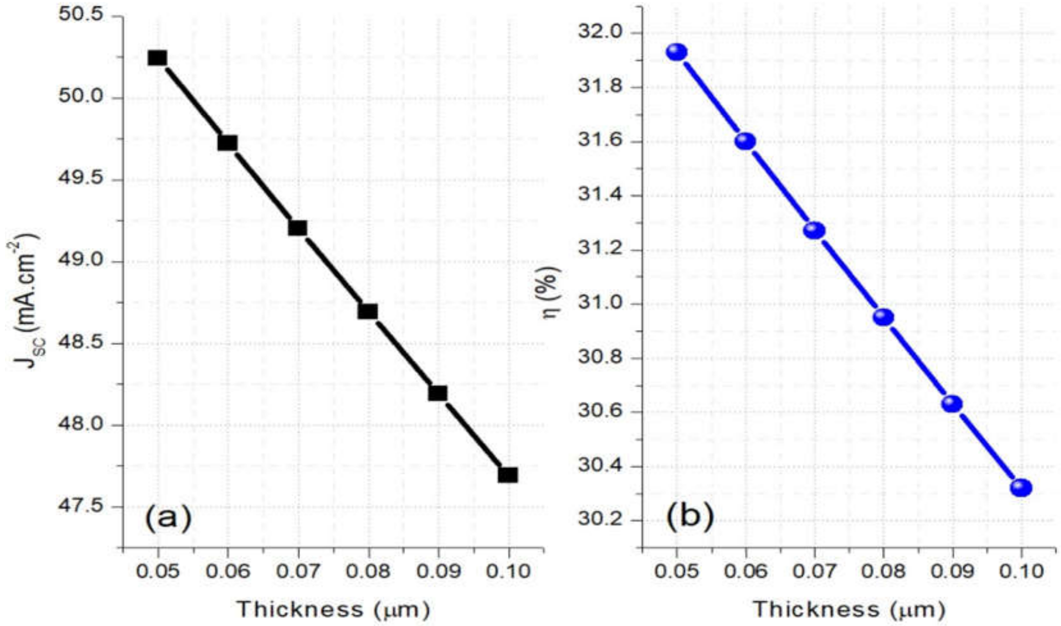

Fig. (4.22) The impact of n$^+$(3C-SiC) layer thickness on the (a) Short-circuit current density (J_{SC}) (b) Efficiency (η).

Figure (4.23) shows the impact of changing this layer thickness on the QE of the cell, which proves that as the n$^+$ buffer layer thickness decreases the QE of the cell improves especially in the UV region. Figure (4.24) illustrates the very slight variation of the JV shape with n$^+$ buffer thickness variation.

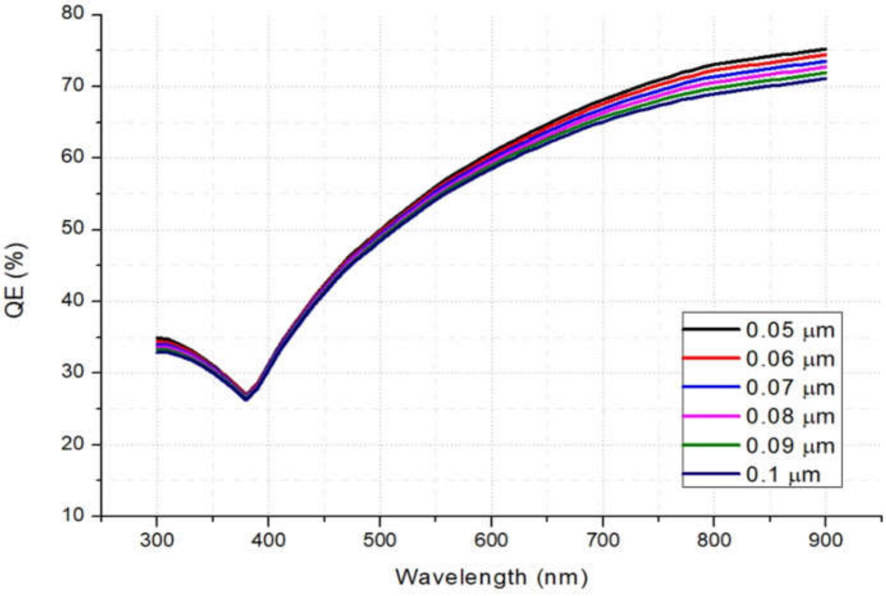

Fig. (4.23) The impact of n$^+$(3C-SiC) layer thickness on the QE.

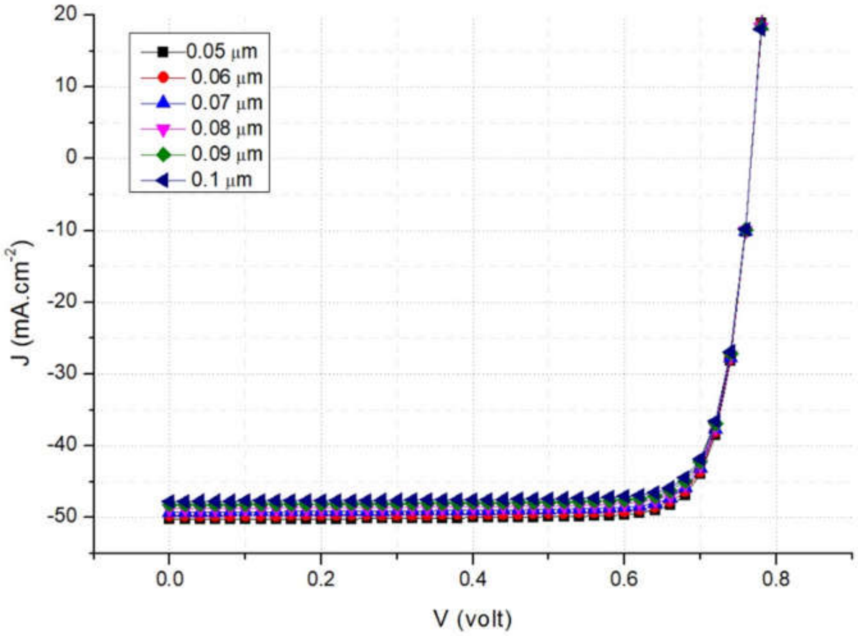

Fig. (4.24) The impact of n$^+$(3C-SiC) layer thickness on the JV curve.

On the other hand, changing the n-Cr (3C-SiC) thickness does not have a noticeable effect on cell performance. Thus taking a thin layer of 100 nm is better to reduce the cell resistance.

As a conclusion of the parametric study on the thickness parameter, the optimum thicknesses for each layer of the cell are (3, 2.5, 0.1, 0.1, and 0.2 µm) for (p-Al(3C-SiC), i-(3C-SiC), n-Cr(3C-SiC), n$^+$(3C-SiC) and n-(SnO_2)) respectively, that produce a power conversion efficiency of 30.27 %, V_{OC} 0.7680 V, J_{SC} 47.63 mA.cm^{-2}, and a fill factor of 82.74 %.

CHAPTER FIVE

PHYSICAL CHARACTERISTICS

5.1 INTRODUCTION

The efficiency of solar cells is generally studied for (STC) Standard Testing Conditions, which are: 1000 $W.m^{-2}$ direct ordinary intensity of light, Air Mass of 1.5 (AM 1.5) and 300 K temperature. The PV cells behavior dramatically affected by the temperature as, in the applications of terrestrial, they are commonly facing temperatures in the ranges from (288 K) 15 ºC to (323 K) 50 ºC [77] and to also temperatures higher than that in space applications and systems of the concentrator [110]. Increasing temperature causes both FF and PCE to decrease, the efficiency degradation due to V_{OC} decrease [110][111][112][113]. On the other hand, the output current of solar cells is directly proportional to the irradiation, so any change of the light intensity causes a proportional change in the J_{SC} [111], while the open-circuit voltage V_{OC} is less sensitive to light intensity than the short-circuit current. Thus, the power conversion efficiency and the whole performance of the cell will be influenced by the light intensity variation.

5.2 ILLUMINATION AND TEMPERATURE IMPACT

The characteristics of (JV) curve of a single diode model of the PV cell are usually described as given in equation (5.1) [114][91][102][115], which constructed from five variables called photo generated current (I_{ph}), current of reverse saturation (I_0), factor of diode ideality (ń), resistance of series (R_S) and resistance of shunt (R_{Sh}). These variables have a strong and direct effect on the (JV) curve shape of a solar cell at any level of light intensity and temperature and therefore determine the values of the parameters of the performance [112].

$$I = I_{ph} \quad I_0\left[\exp\left(\frac{1}{\acute{n}V_{th}}(V + IR_s) \quad 1\right] \quad G\ (V + IR_s) \qquad (5.1)$$

Where, V_{th} is the thermal voltage =KT/q, and G= $1/R_{Sh}$ is the conductance of shunt R_{Sh} .

The impact of light intensity on the photovoltaic parameters is represented by its effect on V_{OC} and J_{SC}. Open-circuit voltage V_{OC} as a function of irradiation can be express in the following equation:

$$V_{oc} = V_{ocn} + \frac{nKT}{q}\ln\left(\frac{E}{I_{0n}}\right) \qquad (5.2)$$

Where: V_{ocn} and I_{0n} are the open-circuit voltage and the irradiation under nominal conditions, while the relationship that links J_{SC} with the irradiance I_0 can be written in the equation (5.3) [111]:

$$\mathrm{J_{sc} = K_E \times I_0} \qquad (5.3)$$

Where K_E is a constant represents the relative variation of J_{SC} as a function of illumination. Many attempts were achieved to study the dependency of solar cell parameters to the major conditions of the environment, the irradiation and the temperature. The behavior of the PV cell is affected by light intensity variance as its performance variables, i.e. open-circuit voltage (V_{OC}), short-circuit current density (J_{SC}), fill factor (FF) and efficiency (η). These parameters are directly related to the characteristics of the cells, that is resistance of series (R_S), resistance of shunt (R_{Sh}=1 / G_{Sh}), and the current of reverse saturation (I_0) [111]. The behavior of solar cells could be greatly affected by the inner series resistance. The area of the maximum rectangle in the output characteristics curve represents the maximum output power of the PV cell. The rectangle area increases by increasing the "sharpness" of the knee in the photovoltaic output characteristics. At increasing the light intensity, the internal series resistance causes a larger of these characteristics. Solar cells are normally designed for best performance at radiation intensities as obtained at the earth's surface [113]. The lowest-resistance solar cell demonstrates a repetitive increase in power output with an increase in light intensity, while the limited R_S values induce the highest output to enhance less quickly with increasing light intensity, this influence is successively increased with the rising of resistance of series and illumination [113]. For photovoltaic cells with small values of series resistance or with fairly low illumination rates so the influence of series resistance could be ignored. This is demonstrated in the situation that the multiplication of IR_S should be negligently low in comparison to the V node voltage. When this requirement is not satisfied, a decrement in the voltage of the ends will be equal to the multiplication of the inner resistance of series R_S and the difference in the current generated by light [113], thus a reduction in efficiency with increasing light intensity in some solar cells is due to the high value of R_S. On the other hand, the temperature has a significant impact on the photovoltaic parameters. At excessive values of temperature, some of the parameters as electron and hole mobility, concentrations of carrier and the material band-gap will be influenced that leads to a reduction in the cell efficiency [102]. The reduction in a semiconductor band-gap with increasing temperature could be seen as an increment in the electron energy inside the material. Smaller amount of energy is needed to destroy the bond. In the band-gap of the semiconductor model of bond, the decrement in the energy of bond decreases the band-gap too. As a result, the large values of temperature decreases the band-gap. V_{OC} is the highly influenced parameter by temperature, the variance of V_{OC} with the temperature can be expressed by equation (5.4) [114]:

$$\frac{d(V_{oc})}{dT} = \frac{V_{oc}}{T} \quad \frac{E_g/q}{T} \qquad (5.4)$$

5.3 OPTIMAL STRUCTURE

The impact of temperature and illumination on the optimal solar cell structure performance resulting from the parametric study will be investigated in this section. The optimal structure of 3C-SiC PIN solar cell is the one that produces a power conversion efficiency, V_{OC}, J_{SC}, and fill factor of 30.27 %, 0.7680 V, 47.63 mA.cm^{-2} 82.74 %, respectively. That had properly optimized input parameters resulted from the previous parametric study as illustrated in table (5.1). The energy band structure, the JV curve and the quantum efficiency of the optimal cell shown in figures (5.1), (5.2) and (5.3) respectively.

Table (5.1) Simulation main parameters.

Parameters	**n-SnO_2**	**n^+(3C-SiC)**	**n-Cr(3C-SiC)**	**i-(3C-SiC)**	**p-Al(3C-SiC)**
Thickness (μm)	0.2	0.1	0.1	2.5	3
Donor density N_d (cm^{-3})	$1*10^{18}$	$1*10^{22}$	$1*10^{19}$	$1*10^{15}$	$1*10^{1}$
Acceptor density N_a (cm^{-3})	$1*10^{2}$	$1*10^{5}$	$1*10^{2}$	$1*10^{15}$	$1*10^{15}$

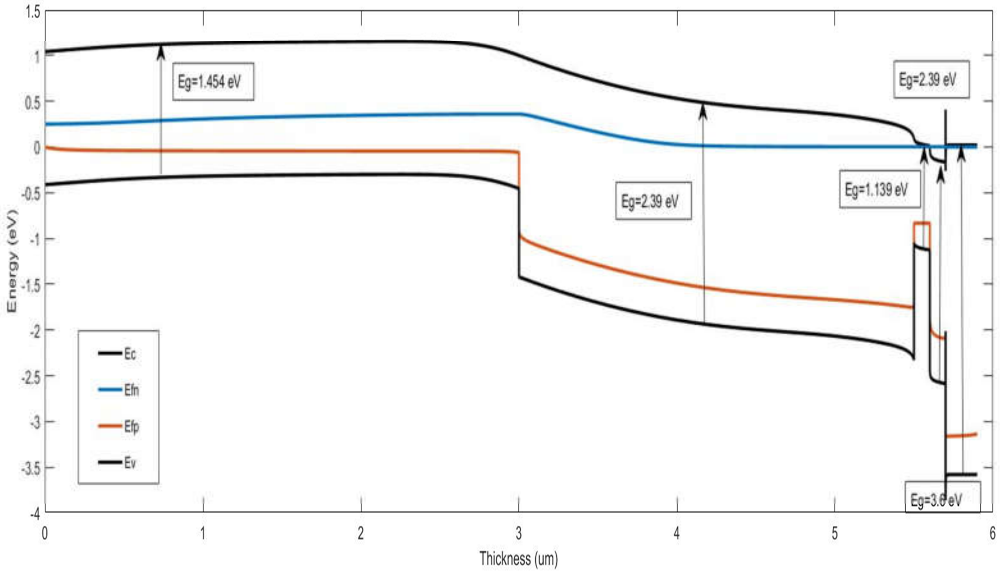

Fig. (5.1) The Energy Band structure of the optimal cell.

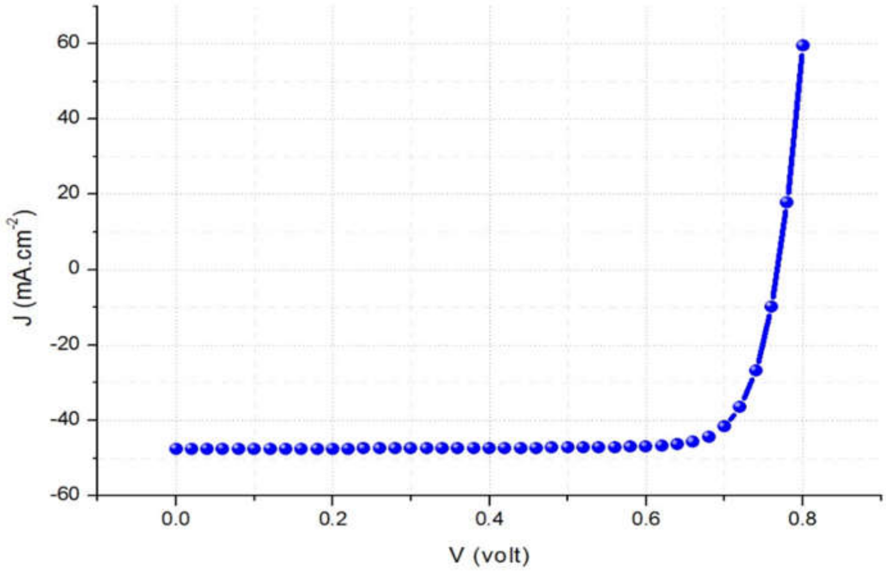

Fig. (5.2) The JV curve of the optimal cell.

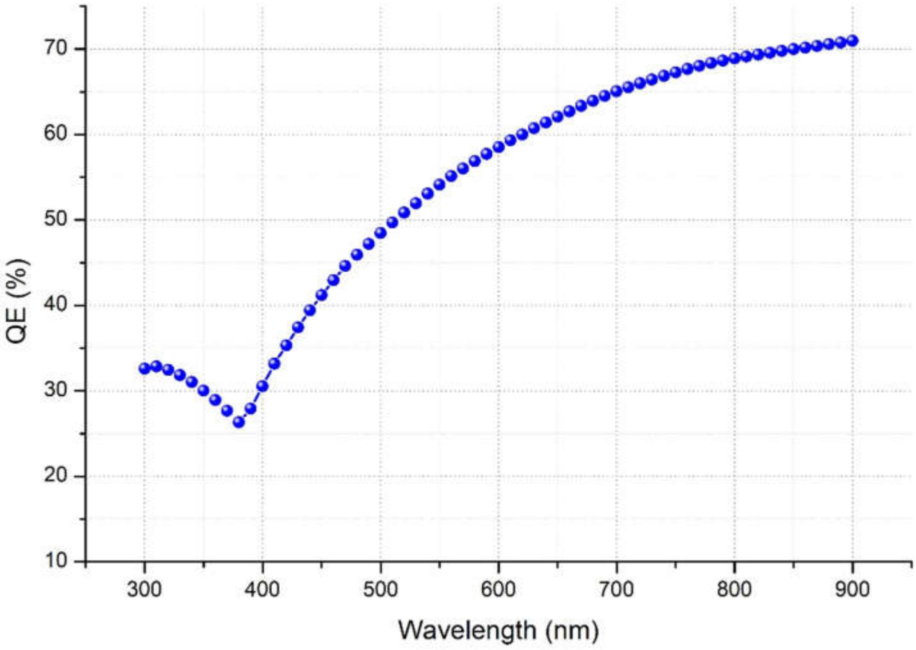

Fig. (5.3) The QE of the optimal cell.

As it was mentioned before, that the current simulation is solved using SCAPS software. This software provide a control on the operating parameters like temperature and illumination through the action panel. After setting the operation point of the solar cell, a list of all cell parameters can be calculated [102].

5.3.1 ILLUMINATION

Changing the intensity level of illumination on a PV cell affects all the solar cell parameters. The photo-generated current is directly proportion to the flux of photons and thus J_{SC} is proportional to the irradiance directly of the solar spectral as the equation [115][116][117]:

$$J_{SC} = q\int_{h\upsilon=E_g}^{\infty} \frac{dN_{ph}}{d\ \ \upsilon} d(\ \ \upsilon) \qquad (5.5)$$

Where N_{ph} is the flux of initial photon. The series resistance has a stronger impact on the performance at high intensity, while the shunt resistance has a higher impact on the performance of the cells at a low light intensity [118].

The first step of the study is keeping the temperature constant at 300 K and start to change the light intensity from 250 to 1200 W.m^{-2} to study the change in the photovoltaic parameters. Table (5.2) implies that the short-circuit current density J_{SC} increases linearly with increasing light intensity, while the V_{OC} increases logarithmically only for I_0 (light intensity) equal or less than1000 W.m^{-2}. At higher light intensity, i.e., more than 1000 W.m^{-2} the open-circuit voltage V_{OC} is almost constant. The results indicated that increasing the irradiation level has a significant impact on the short-circuit current, where the increasing of light intensity from 250 to 1200 W.m^{-2} produce an increase of the J_{SC} from 11.924 to 57.149 mA.cm^{-2}. The reason which stand behind this effect is that the high light intensity implies higher absorption of photons, and hence increasing the carrier generation which lead to produce a high value of J_{SC}. A reduction in the fill factor FF with higher irradiation intensity (I_0>500 W.m^{-2}) was observed, while V_{OC} is almost constant at 0.76 V, due to the effect of the high series resistance [111].

Table (5.2) Cell's parameters variation with light.

Light intensity I_0 (W.m^{-2})	**V_{OC} (V)**	**J_{SC} (mA.cm^{-2})**	**FF (%)**	**η (%)**
250	0.7593	11.924	83.19	30.13
500	0.7661	23.835	83.09	30.34
750	0.7678	35.739	82.92	30.34
1000	0.7680	47.636	82.74	30.27
1200	0.7677	57.149	82.60	30.20

The open-circuit voltage is much less sensitive to the light factor. The cause of the slight reduction in efficiency was the decrease in the fill factor, which mostly depends on two solar cells parameters; the high values of R_S series resistance and the change in the shape of the dark JV curve. Figure (5.4) shows the impact of irradiance on the cell parameters and figure (5.5) shows the influence of the illumination variation on the shape of JV curve, which is highly affected due to the severe effect on the J_{SC}.

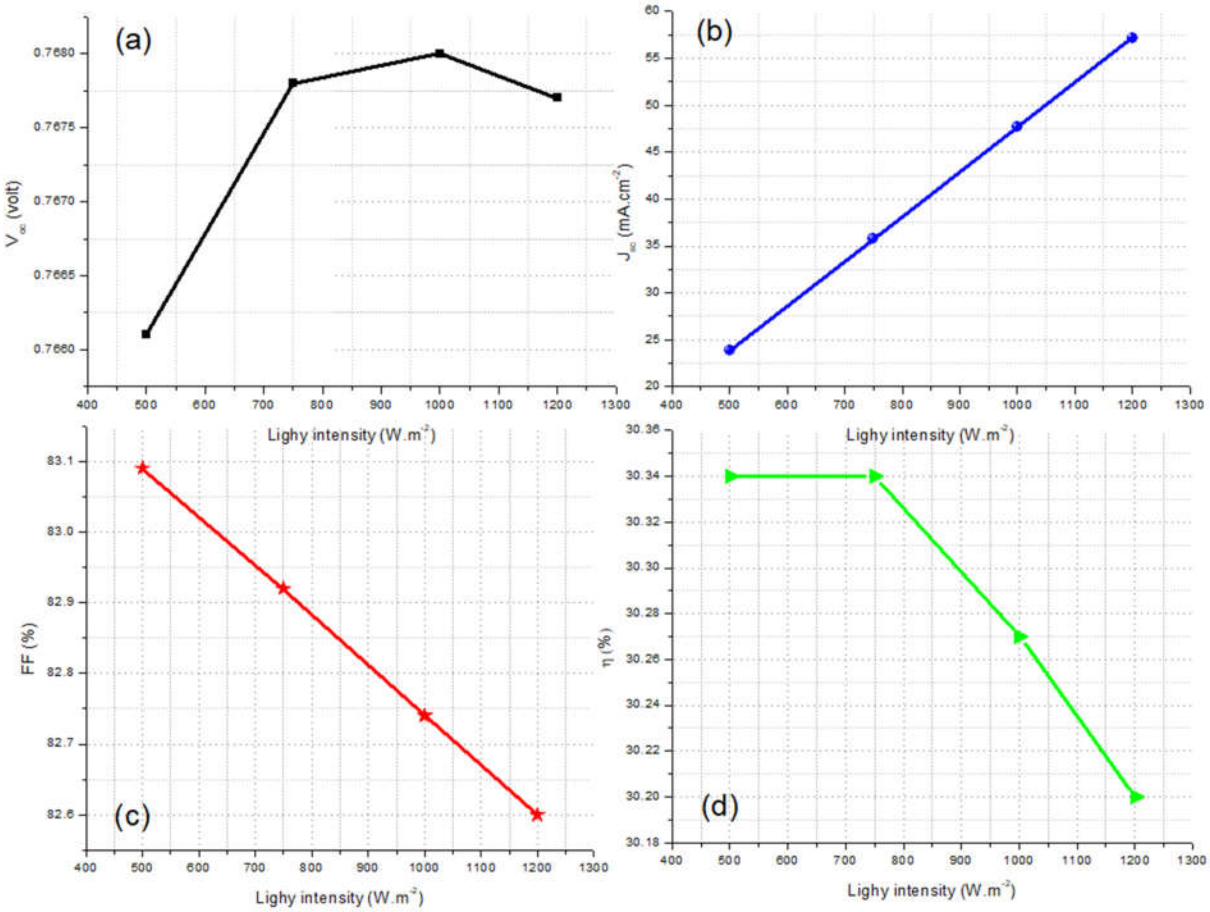

Fig. (5.4) The impact of light intensity on the cell parameters (a) Open-circuit voltage (V_{OC}) (b) Short-circuit current density (J_{SC}) (c) Fill Factor (FF) (d) Efficiency (η).

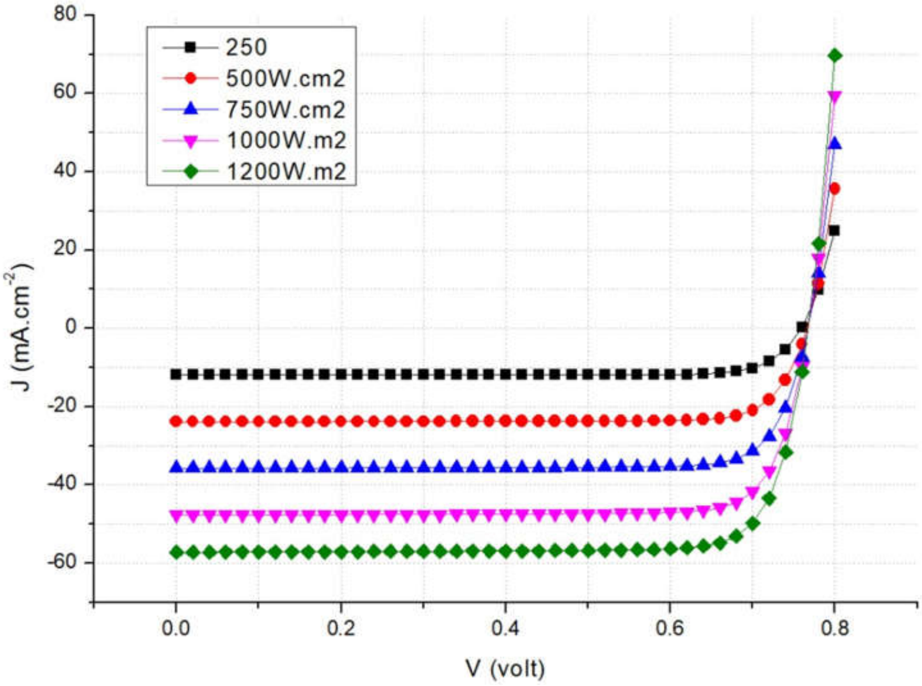

Fig. (5.5) The influence of illumination variation on the JV curve of the cell.

5.3.2 TEMPERATURE

Photovoltaic cells are highly affected by temperature variation. Increases in temperature makes the semiconductor band-gap decrease, and hence most of the parameters of the semiconductor material are influenced. The reduction in the semiconductor band-gap with temperature increment can be ascribed to the increasing in electrons energy in the material. Thus, smaller energy is required to destroy the bond. Most of the variance in the energy gap of the semiconductors with temperature is attributable to the two following processes [119] :

- The main contribution to the temperature-dependent of the semiconductors band-gap is the shift in the relative position of the conduction and valence bands due to the temperature-dependency interaction between the electron and the lattice.

- The temperature-dependent expansion of the lattice involves a change in the relative position of the valence band and conduction band.

Using the relation of Varshni [120] that links the band-gap with temperature which can be described in the equation:

$$\mathrm{E_g(T) = E_g(0)} \quad \frac{\overline{\alpha}\mathrm{T}^2}{(\mathrm{T}+\beta)} \quad (5.6)$$

Where, E_g (T) is the semiconductor band-gap at some values of temperature, which can be direct or indirect, E_g (0), is the band-gap at T~ 0 K and $\overline{\alpha}$ as well as β are constants. Other solar cells parameters will be affected through the impact of temperature on the band-gap. The effect of temperature on the short-circuit current density J_{SC} can be seen in the equation (5.5) which is used to calculate the value of J_{SC} at different values of temperature [117]. J_{SC} can be found by integrating the solar spectrum to the corresponding E_g by equation (5.5), the E_g value for each T can be extracted from equation (5.6). On the other hand the open-circuit voltage as a function of T can be given by [117]:

$$V_{OC} = \frac{KT}{q} \ln(\frac{J_{SC}}{J_0} + 1) \quad (5.7)$$

Where, J_{SC} ~ J_{ph}, V_{OC} is directly relevant to J_{SC} and J_o reverse saturation current density, and therefore to E_g. The V_{OC} temperature dependence can be gained from equation (5.8) as [117]:

$$\frac{dV_{OC}}{dT} = \left(\frac{V_{OC}}{T}\right) + V_{th}(\frac{1}{J_{SC}}\frac{dJ_{SC}}{dT} \quad \frac{1}{J_0}) \quad (5.8)$$

The simulation was performed at irradiance level of 1000 $W.m^{-2}$, and the temperature was varying from 300 to 400 K in a step of 20. Figure (5.6) shows the effect of temperature on the cell parameters. The results of simulation proved that increasing temperature has a dramatic impact on V_{OC}, as the temperature increases the V_{OC} decreases and consequently the efficiency of the cell decreases. The reduction in the V_{OC} is because it is directly depends on the current density of saturation J_0 that reduces rapidly as well with raising values of temperature [115][116]. The change in temperature from 300 to 400 K led to increasing the saturation current and hence the V_{OC} reduces from 0.768 to 0.516 V, which in turn decreases the fill factor and the efficiency of the solar cell from 30.27% to 18.10% respectively. Reverse saturation current, J_0, is a measure of recombination or leakage of the minority carriers through the PN junction in reverse condition of biasing. This leakage results from the recombination of the carrier on each side of the junction in the neutral areas and, thus J_0 mainly controls the value of V_{OC} in the PV cell. Minority carriers are thermally-produced; consequently, J_0 is extremely sensitive to changes in temperature. Reverse saturation current density, J_0, for PN junction PV cell is given by [117]:

$$\mathrm{J}_0 = q(\frac{D_n}{L_n N_a} + \frac{D_p}{L_p N_d}) n_i^2 \ (5.9)$$

Where, L_n and L_p are lengths of diffusion of minority carriers in n and p regions, respectively. From equation (5.9), J_0 is totally committed to the proportionality to ~ $\mathrm{n_i^2}$ and ni can be described as [117]:

$$\mathrm{n_i^2} = N_c N_v \exp(\ \frac{E_g}{KT}) \ (5.10)$$

Furthermore higher temperature reduces the band-gap, thus affecting the cell whole performance [121][117]. Intrinsic carrier concentration depends on the energy of the band-gap (lower band-gaps leading to higher intrinsic carrier concentration). Merging equations (5.9) and (5.10), J_0 can be represented in terms of temperature and band-gap [122] as in equation (5.11):

$$J_0 = C\, T^3 \exp(\ \frac{E_g}{KT}) \ (5.11)$$

According to equation (5.11), doping as well as the solar cells parameters are combined in this single constant C [122]. The temperature and band-gap parameters of the solar cell are essential for calculation process. The larger the E_g the lower the J_0.

Finally, the effect of temperature through its effect on J_{SC} and V_{OC} could be seen clearly in the fill factor parameter, which can be described as the ratio of the maximum output power to the product of the V_{OC} and the J_{SC}. With the temperature increase, J_0 increases, and hence, V_{OC} decreases which in turn reduces the fill factor and consequently the efficiency of the PV cell. Table (5.3) depicts the current structure behavior at the temperature values ranging from 300 to 400 K. Figure (5.7) shows the impact of temperature on the JV curve shape, which is directly affected through the effect of V_{OC} that in turn impacted by operating temperature.

Table (5.3) Output parameters of a solar cell sample at different temperatures.

Temperature (K)	V_{OC} (V)	J_{SC} (mA.cm^{-2})	FF (%)	η (%)
300	0.768	47.636	82.74	30.27
320	0.730	47.612	81.74	28.42
340	0.672	47.587	80.03	25.62
360	0.621	47.571	78.19	23.11
380	0.567	47.562	76.07	20.54
400	0.516	47.563	73.72	18.10

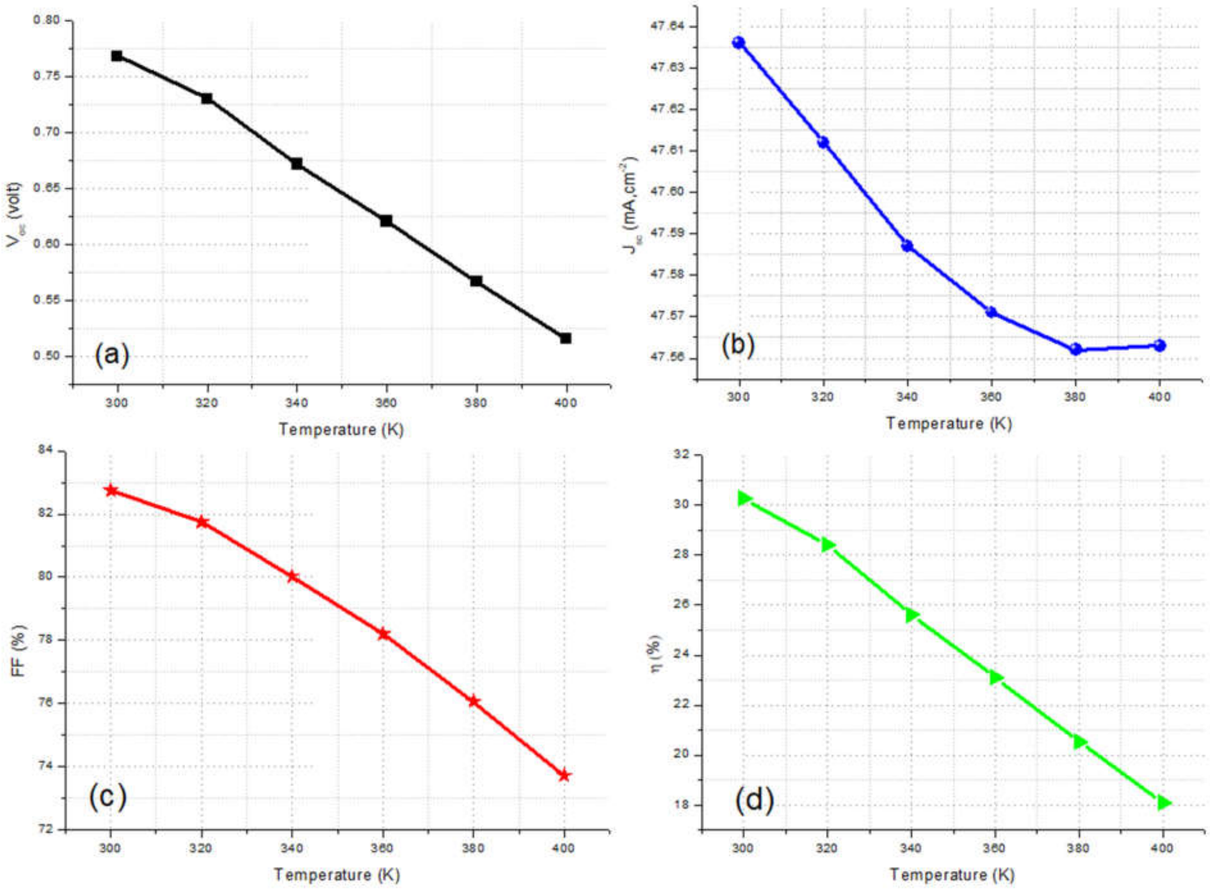

Fig. (5.6) The impact of temperature variation on cell parameters (a) Open-circuit voltage (V_{OC}) (b) Short-circuit current density (J_{SC}) (c) Fill Factor (FF) (d) Efficiency (η).

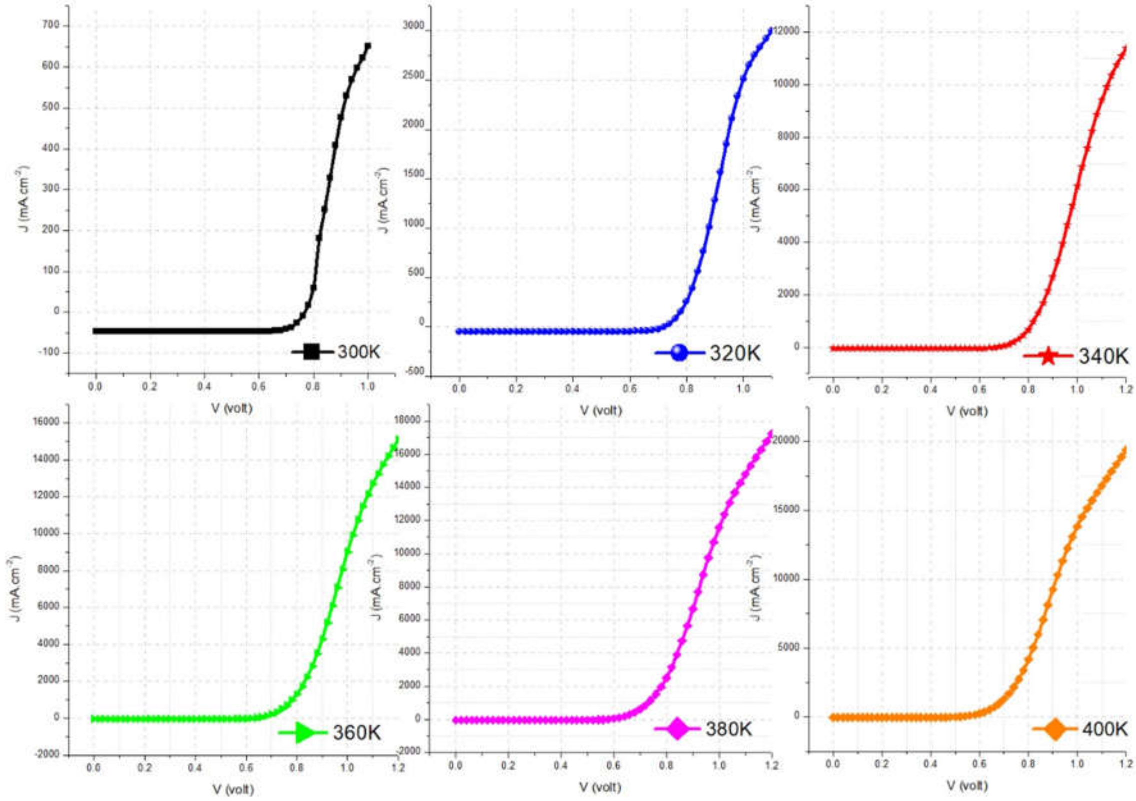

Fig. (5.7) The influence of the temperature variation on the JV curve of the cell.

CHAPTER SIX

CONCLUSIONS AND FUTURE WORKS

6.1 CONCLUSIONS:

The utilization of simulation software would help to understand the basic concepts of the operation of solar cells in details. Owing to the unrestricted nature of the simulation models, the research could recommend multiple techniques for enhancing its devices before manufacturing them to save effort, time, and cost. Based on this concept we used SCAPS software to study the performance of the PIN solar cell. The proposed structure in the current study, based on 3C-SiC material consists of five layers, the absorber is a 3C-SiC doped with Al to obtain p-type semiconductor properties. Two n-type buffers n-3C-SiC and a 3C-SiC doped with Cr to get the n-type semiconductor properties, an intrinsic layer of 3C-SiC which inserted between the absorber and the buffer and finally a window layer of SnO_2 material. Such doping with Cr and Al of the 3C-SiC produces a semiconductor with energy gap of 1.139 and 1.454 eV, respectively. This will lead to an increase the sunlight absorption in most of the visible regions. A parametric study was achieved on a reference cell that based on initial values. The study includes the effect of doping density and thickness for each layer of the cell to obtain the optimal design with best performance. In addition to that a study of the physical characteristics impact, illumination and temperature, on the performance of the optimum cell was achieved. The study indicated that:

1. The concentration of acceptors in the absorber layer was varied in a moderate range from (10^{14} to 10^{17} cm^{-3}). It was found that the acceptor concentration of 10^{15} cm^{-3} is best density in order to obtain a power conversion efficiency of 18.73 %. An increasing in

the carriers density will cause an elevated in the saturation process of the device as well as V_{OC}. However, with a further increase in the concentration of carriers more than $N_a=10^{15}$ cm^{-3}, recombination at the interface enlarge and the possibility of photo-generated electrons accumulation reduced.

2. A variation in the carrier concentration in the n^+ (3C-SiC) buffer layer from 10^{18} to 10^{22} cm^{-3} produces an increasing in the power conversion efficiency of the cell from 16.84 to 21.52%. The effect of the carrier concentration in this layer on the output of the cell is not as significant as the carrier concentration effect in the absorber layer. The optimum doping density in this layer is at $N_d = 10^{22}$ cm^{-3} that produces an efficiency of 21.44 %.
3. The concentration of donors in the buffer layer should not be less than the acceptors in the absorber, since it causes serious recombination in the interface. As the donor concentration equal to the value of acceptor concentration, the electron traps decrease to a lower level at the interface, which eventually increases the J_{SC} and caused a high increment in the efficiency. As the acceptors in the absorber is 10^{15} cm^{-3} thus, the donors in the buffer should be more than this value to have best output. In the current structure for the n-Cr (3C-SiC) $N_d=10^{19}$ cm^{-3} is the optimum donors that gives an efficiency of 22.69 %. Beyond the value of 10^{19} cm^{-3} is not a good choice for a semi-conductive material, as it can be turned into metallic regime.
4. The variation in the carrier concentration for the intrinsic layer of 3C-SiC and the SnO_2 layer doesn't have a high impact on cell performance. The good doping density of the SnO_2 layers is $N_d=10^{18}$ cm^{-3} and the intrinsic carrier concentration of 10^{15} cm^{-3} for

the i-(3C-SiC), that produces a power conversion efficiency of 22.78 %.

5. The efficiency of the cell is improved by increasing the thickness of the absorber layer in a restricted range, which leads to increasing in the collection of photo-generated carriers before recombination that improves efficiency. However increasing it more than the optimum value leads to more photons absorbed deep inside the absorber and the generated carriers cannot reach the depletion region during their lifetime and they will be recombined. The optimum absorber layer thickness is 3 μm that gives a power conversion efficiency of 24.14%.
6. An intrinsic layer of (3C-SiC) with a proper thickness is very significant to enlarge the space charge region in order to enhance the internal electric field and increase the separation of generated charge carriers, besides increasing the absorption and consequently the generation in this region. All these points proved that using a PIN structure leads to enhance cell performance and increases efficiency. The optimum thickness for this layer is 2.5 μm that makes J_{SC} increases from 37.73 to 54.27 mA.cm^{-2} due to increasing the photo-generated carriers which in turn makes the efficiency of the cell elevates excessively from 24.14 to 34.45%.
7. Using a TCO layer in the current cell is SnO_2 material as a window layer with proper thickness reduces the reflection losses and improves the efficiency of the cell. However, to reduce the high value of J_{SC} that produces as a result of a relative thick intrinsic layer, a thickness of more than 0.1 μm is required to increase the absorption in this layer and reduce the number of photons reach the absorber and consequently the photo-generated carriers, and this will yield a decrease the short-circuit current. The optimum

thickness for this layer is 0.2 μm, which reduces the J_{SC} from 54.27 to 50.24 mA.cm^{-2} and still produce a relatively high efficiency of more than 30 %.

8. The efficiency of the 3C-SiC solar cell can be enhanced by reducing the thickness of the buffer layer due to an increment in the number of absorbed photons reaching the absorber layer, but the further thinning of these layers will increase the chance of the cell being shunted. The optimum n^+ (3C-SiC) buffer layer thickness is 0.1 μm which gives a cell efficiency of 30.32 % and also reduces the J_{SC} to 47.69 mA.cm^{-2}. Using n^+ (3C-SiC) buffer layer also enhances the absorption of light in the UV region due to the high band gap of this layer.
9. Changing the thickness of the n-Cr (3C-SiC) layer does not have a noticeable effect on the performance. Thus taking a thin layer of 100 nm is better to reduce the cell resistance, which gives an efficiency of 30.27 %.
10. The optimum structure of the current 3C-SiC solar cell has doping densities of $N_a=10^{15}$ cm^{-3} for the p-Al (3C-SiC), $N_d=10^{22}$, 10^{19}, and 10^{18} cm^{-3} for n^+, n-Cr (3C-SiC) and SnO_2 layers respectively and carrier concentration of 10^{15} cm^{-3} for the intrinsic layer. On the other hand the thicknesses of the optimum structure are (3, 2.5, 0.1, 0.1, 0.2 μm) for p-Al (3C-SiC), i-(3C-SiC), n-Cr (3C-SiC), n^+ (3C-SiC) and SnO_2 layers respectively, all these input parameters produce output cell parameters of (V_{OC}=0.7680 V, J_{SC}=47.63 mA.cm^{-2}, FF=82.74 % and η=30.27 %).
11. The influence of the light intensity was investigated on the optimal structure and it was found that increasing light intensity has a high impact on the short-circuit current, while the open-circuit voltage is less sensitive to illumination variation. The illumination level

changing from 250 to 1200 W.m^{-2} produced an increasing in the J_{SC} from 11.924 to 57.149 mA.cm^{-2}. This is happened due to the higher absorption of photons, and hence increasing the carrier generation. A reduction in the fill factor and the efficiency with higher irradiation intensity that is more than 500 W.m^{-2} was observed, due to the effect of the high series resistance.

12. The impact of changing the cell temperature was studied on the optimal cell and it was found that the most affected parameter by temperature variation is the open-circuit voltage. As the temperature increases from 300 to 400 K the V_{OC} decreases from 0.768 to 0.516 V and consequently the efficiency of the cell decreases from 30.27 to 18.10%, V_{OC} considerably decreases due to the decrement in current of saturation that reduces directly with an increase in temperature.

6.2 FUTURE WORKS:

1. A fabrication of 3C-SiC thin film solar cell with optimum design gained from the current simulated data in practice and finding the characteristics of the fabricated cells, such as V_{OC}, J_{SC}, FF, η, and QE to make a comparison with the simulation results.
2. Using this structure in constructing a tandem junction solar cell and utilizing a proper back and front contact.
3. Study the influence of the multi defect levels on the cell performance.

APPENDIX (A)

The series resistance R_S of the proposed 3C-SiC solar cell structure was calculated by using the information in the website PV Education: https://www.pveducation.org/pvcdrom/solar-cell-operation/series-resistance

Series Resistance

Series resistance in a solar cell has three causes: firstly, the movement of current through the emitter and base of the solar cell; secondly, the contact resistance between the metal contact and the silicon; and finally the resistance of the top and rear metal contacts. The main impact of series resistance is to reduce the fill factor, although excessively high values may also reduce the short-circuit current.

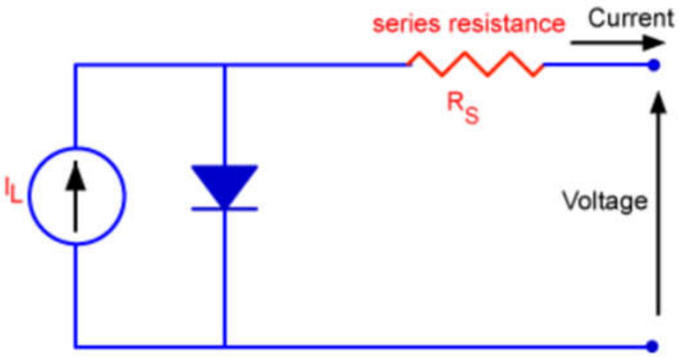

Schematic of a solar cell with series resistance.

$$I = I_L \quad I_0 \exp(\frac{q(V + IR_S)}{nKT}$$

Where: I is the cell output current, I_L is the light generated current, V is the voltage across the cell terminals, T is the temperature, q and k are constants, n is the ideality factor, and R_S is the cell series resistance. The formula is an example of an implicit function due to the appearance of the current, I, on both sides of the equation and requires numerical methods to solve.

Series resistance does not affect the solar cell at open-circuit voltage since the overall current flow through the solar cell, and therefore through the series resistance is zero. However, near the open-circuit voltage, the IV curve is strongly affected by the series resistance. A straight-forward method of estimating the series resistance from a solar cell is to find the slope of the IV curve at the open-circuit voltage point.

An equation for the FF as a function of series resistance can be determined by noting that for moderate values of series resistance, the maximum power may be approximated as the power in the absence of series resistance minus the power lost in the series resistance. The equation for the maximum power from a solar cell then becomes:

$$P'_{MP} = V_{MP}I_{MP} \quad I_{MP}^2R_S = V_{MP}I_{MP}\left(1 \quad \frac{I_{MP}}{V_{MP}}R_S\right) = P_{MP}(1 \quad \frac{I_{SC}}{V_{OC}}R_S)$$

$$P'_{MP} = P_{MP}\left(1 \quad \frac{R_S}{R_{CH}}\right)$$

defining a normalized series resistance as;

$$r_S = \frac{R_S}{R_{CH}}$$

gives the following equation which approximates the effect of series resistance on the output power of a solar cell;

$$P'_{MP} = P_{MP}(1 \quad r_S)$$

Assuming that the open-circuit voltage and short-circuit current are not affected by the series resistance allows the impact of series resistance on FF to be determined;

$$P'_{MP} = P_{MP}(1 \quad r_S)$$

$$V'_{OC}I'_{SC}FF' = V_{OC}I_{SC}FF(1 \quad r_S)$$

$$FF' = FF(1 \quad r_S)$$

In the above equation the fill factor which is not affected by series resistance is denoted by FF_0 and FF' is called FF_S. The equation then becomes;

$$FF_S = FF_O(1 \quad r_S)$$

An empirical equation, which is slightly more accurate for the relationship between FF_0 and FF_S is;

$$FF_S = FF_O(1 \quad r_S)$$

$$FF_S = FF_O(1 \quad 1.1r_S) + \frac{r_S^2}{5.4}$$

Which is valid for $r_s < 0.4$ and $v_{oc} > 10$.

The following calculator determines the effect of R_s on the solar cell fill factor. Typical values for area-normalized series resistance are between 0.5 $\Omega.cm^2$ for laboratory type solar cells and up to 1.3 0.5 $\Omega.cm^2$ for commercial solar cells. The current levels in the solar cell have a major impact on the losses due to series resistance and in the following calculator, examine the impact raising the current has on the FF.

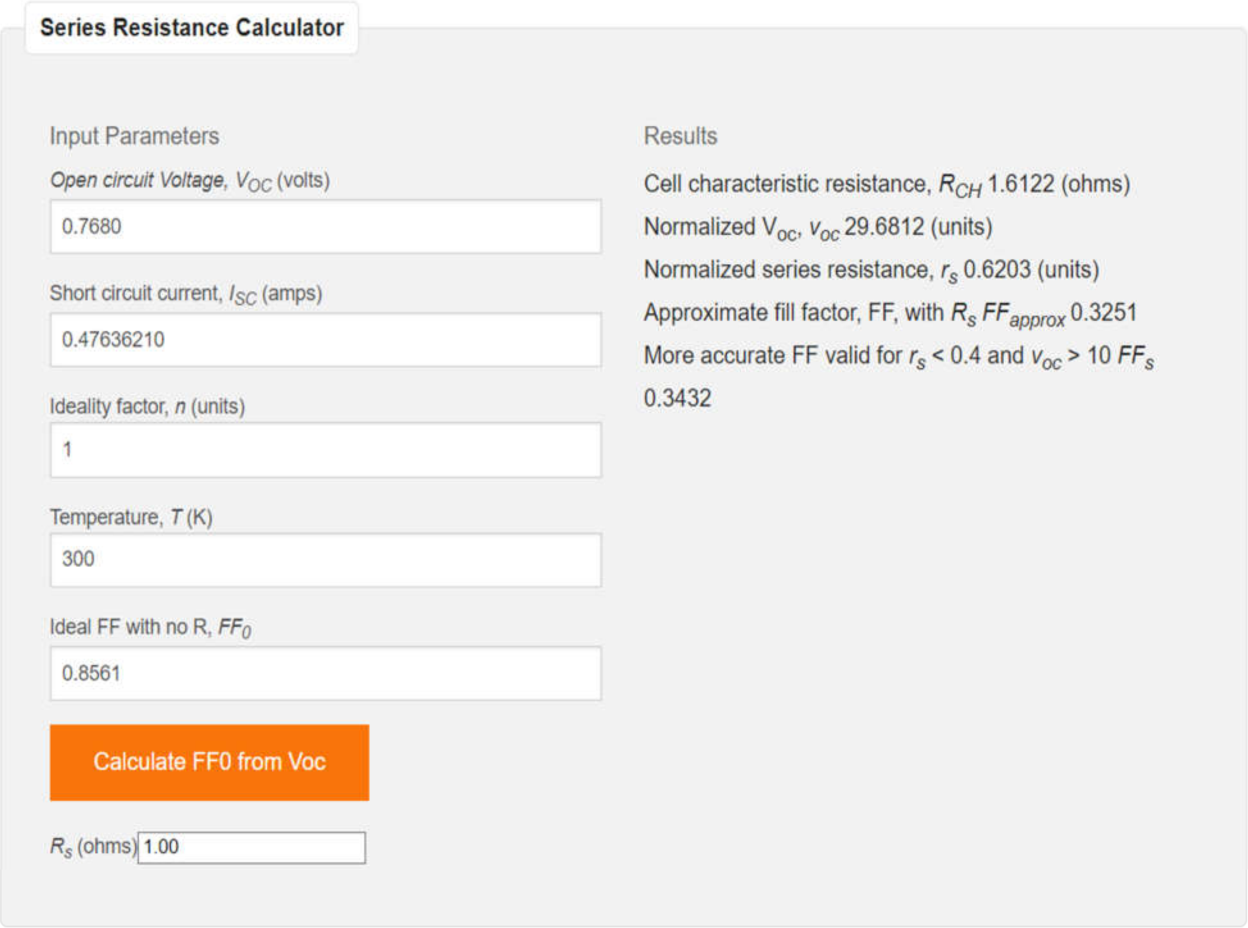

Series Resistance Calculator

Input Parameters

Open circuit Voltage, V_{OC} (volts)

0.7680

Short circuit current, I_{SC} (amps)

0.47636210

Ideality factor, *n* (units)

1

Temperature, *T* (K)

300

Ideal FF with no R, FF_0

0.8561

R_s (ohms) 1.00

Results

Cell characteristic resistance, R_{CH} 1.6122 (ohms)

Normalized V_{oc}, v_{oc} 29.6812 (units)

Normalized series resistance, r_s 0.6203 (units)

Approximate fill factor, FF, with R_s FF_{approx} 0.3251

More accurate FF valid for $r_s < 0.4$ and $v_{oc} > 10$ FF_s

0.3432

APPENDIX (B)

The defects values of the absorber and the buffer layers are listed in the following table:

Layer	Defect type	Defect density N_t total (cm^{-3})	Energy level (eV)
p-Al(3C-SiC)	Amphoteric Single Donor	$1*10^{10}$ $1*10^{14}$	characteristic energy 0.3 0.6 above E_v
n-Cr(3C-SiC)	Single Donor	$1*10^{13}$	0.4 below E_c
n^+ (3C-SiC)	Amphoteric	$1*10^{14}$	characteristic energy 0.1

REFERENCES

[1] P. R. Bauquis, “A Reappraisal of Energy Supply and Demand in 2050,” *Oil Gas Sci. Technol.*, vol. 56, no. 4, pp. 389–402, 2001.

[2] M. Houmad, H. Zaari, A. Benyoussef, and A. El Kenz, “Optical properties of titanium and iron doped 3C-SiC behaviors TB-mBJ,” *Chinese J. Phys.*, vol. 54, no. 6, pp. 960–967, 2016.

[3] S. W. Hur *et al.*, “Organic photovoltaic effects using CuPc and C60 depending on layer thickness,” *Synth. Met.*, vol. 154, no. 1–3, pp. 49–52, 2005.

[4] A. Goetzberger, C. Hebling, and H. W. Schock, “Photovoltaic materials, history, status and outlook,” *Mater. Sci. Eng. R Reports*, vol. 40, no. 1, pp. 1–46, 2003.

[5] A. Rothwarf and K. W. Böer, “Direct conversion of solar energy through photovoltaic cells,” *Prog. Solid State Chem.*, vol. 10, no. PART 2, pp. 71–102, 1975.

[6] J. Transistors, “06773080,” 1948.

[7] J. Bardeen and W. H. Brattain, “Transistor, a semiconductor triode,” *Proc. IEEE*, vol. 86, no. 1, pp. 29–30, 1998.

[8] D. M. Chapin, C. S. Fuller, and G. L. Pearson, “A new silicon p-n junction photocell for converting solar radiation into electrical power [3],” *J. Appl. Phys.*, vol. 25, no. 5, pp. 676–677, 1954.

[9] A. Goetzberger, J. Knobloch, and B. Voss, “Crystalline silicon solar cells,” *New York*, pp. 114–118, 1998.

[10] S. J. Fonash, *Cell Solar Physics Device physics*. 2010.

[11] D. E. Carlson and C. R. Wronski, “Amorphous silicon solar cell,” *Appl. Phys. Lett.*, vol. 28, no. 11, pp. 671–673, 1976.

[12] T. Yamaguchi, J. Matsufusa, and A. Yoshida, “Thin films of CuInSe2 prepared by RF sputtering from various compositional powder targets,” *Sol. Energy Mater. Sol. Cells*, vol. 27, no. 1, pp.

25–35, 1992.

[13] M. T. Kibria, A. Ahammed, S. M. Sony, and F. Hossain, “A Review : Comparative studies on different generation solar cells technology,” *Int. Conf. Environ. Asp. Bangladesh*, pp. 51–53, 2014.

[14] M. Zeman, “Chapter 3. Semiconductor materials for solar cells,” *Syllabus course Sol. Cells*, pp. 3.1-3.27.

[15] C. M. I. Jayawardena, L. J. Rozanski and N. A. N. and P. S. R. P. S. M. J. Beliatis, “Nanoscale,” no. 207890, 2013.

[16] L. Wang, Y. Wang, A. Gerger, A. Lochtefeld, K. Shreve, and A. Barnett, “Three terminal Si-Si:Ge solar cells,” *Conf. Rec. IEEE Photovolt. Spec. Conf.*, no. November 2014, pp. 000286–000289, 2011.

[17] S. Chander, A. Purohit, A. Nehra, S. P. Nehra, and M. S. Dhaka, “A study on spectral response and external quantum efficiency of mono-crystalline silicon solar cell,” *Int. J. Renew. Energy Res.*, vol. 5, no. 1, pp. 41–44, 2015.

[18] S. Chander, A. Purohit, A. Sharma, Arvind, S. P. Nehra, and M. S. Dhaka, “A study on photovoltaic parameters of mono-crystalline silicon solar cell with cell temperature,” *Energy Reports*, vol. 1, pp. 104–109, 2015.

[19] J. Benick *et al.*, “High-Efficiency n-Type HP mc Silicon Solar Cells,” *IEEE J. Photovoltaics*, vol. 7, no. 5, pp. 1171–1175, 2017.

[20] R. R. Bahabry *et al.*, “Corrugation Architecture Enabled Ultraflexible Wafer-Scale High-Efficiency Monocrystalline Silicon Solar Cell,” *Adv. Energy Mater.*, vol. 8, no. 12, pp. 1–9, 2018.

[21] C. Zhou, F. Ji, S. Cheng, J. Zhu, W. Wang, and D. Hu, “Light and elevated temperature induced degradation in B–Ga co-doped cast mono Si PERC solar cells,” *Sol. Energy Mater. Sol. Cells*, vol. 211, no. March, p. 110508, 2020.

[22] I. B. Karki, “Effect of Temperature on the I-V Characteristics of a Polycrystalline Solar Cell,” *J. Nepal Phys. Soc.*, vol. 3, no. 1, p. 35, 2016.

[23] N. F. Ramli *et al.*, “Model development of monolithic tandem silicon-perovskite solar cell by SCAPS simulation,” *AIP Conf. Proc.*, vol. 1838, 2017.

[24] F. Haase *et al.*, “Interdigitated back contact solar cells with polycrystalline silicon on oxide passivating contacts for both polarities,” *Jpn. J. Appl. Phys.*, vol. 56, no. 8, pp. 1–5, 2017.

[25] K. Yoshikawa *et al.*, “Exceeding conversion efficiency of 26% by heterojunction interdigitated back contact solar cell with thin film Si technology,” *Sol. Energy Mater. Sol. Cells*, vol. 173, no. June, pp. 37–42, 2017.

[26] K. Yamamoto, “Towards the Record Efficiency of Si Based Solar Cells,” *AM-FPD 2019 - 26th Int. Work. Act. Flatpanel Displays Devices TFT Technol. FPD Mater. Proc.*, vol. 26th, pp. 1–4, 2019.

[27] H. Liu, L. Zhao, H. Diao, and W. Wang, “High-performance texturization of multicrystalline silicon wafer by HF/HNO3/H2O system incorporated with MnO2 particles,” *Mater. Sci. Semicond. Process.*, vol. 101, no. January, pp. 149–155, 2019.

[28] N. R. Paudel, J. D. Poplawsky, K. L. Moore, and Y. Yan, “Current Enhancement of CdTe-Based Solar Cells,” *IEEE J. Photovoltaics*, vol. 5, no. 5, pp. 1492–1496, 2015.

[29] K. Shen *et al.*, “Stable CdTe solar cell with V2O5 as a back contact buffer layer,” *Sol. Energy Mater. Sol. Cells*, vol. 144, pp. 500–508, 2016.

[30] R. Safa Sultana, A. N. Bahar, M. Asaduzzaman, and K. Ahmed, “Numerical modeling of a CdS/CdTe photovoltaic cell based on ZnTe BSF layer with optimum thickness of absorber layer,” *Cogent*

Eng., vol. 4, no. 1, pp. 1–12, 2017.

[31] G. Kartopu *et al.*, “Enhancement of the photocurrent and efficiency of CdTe solar cells suppressing the front contact reflection using a highly-resistive ZnO buffer layer,” *Sol. Energy Mater. Sol. Cells*, vol. 191, no. October 2018, pp. 78–82, 2019.

[32] S. D. B. K. Sharma, A. Stoesser, S. K. Mondal, S. K. Garlapati, M. H. Faway, V. S. K.Chakravadhanula, R. Kruk, H. Hahn, “Ac ce d M pt,” *ACS Appl. Mater. Interfaces*, vol. 10, pp. 22408–22418, 2018.

[33] L. I. Nykyruy, R. S. Yavorskyi, Z. R. Zapukhlyak, G. Wisz, and P. Potera, “Evaluation of CdS/CdTe thin film solar cells: SCAPS thickness simulation and analysis of optical properties,” *Opt. Mater. (Amst).*, vol. 92, no. December 2018, pp. 319–329, 2019.

[34] S. A. A. Kazmi *et al.*, “Efficient materials for thin-film CdTe solar cell based on back surface field and distributed Bragg reflector,” *Appl. Phys. A Mater. Sci. Process.*, vol. 126, no. 1, 2020.

[35] M. Elbar, S. Tobbeche, and A. Merazga, “Effect of top-cell CGS thickness on the performance of CGS/CIGS tandem solar cell,” *Sol. Energy*, vol. 122, pp. 104–112, 2015.

[36] M. Mostefaoui, H. Mazari, S. Khelifi, A. Bouraiou, and R. Dabou, “Simulation of High Efficiency CIGS Solar Cells with SCAPS-1D Software,” *Energy Procedia*, vol. 74, no. August, pp. 736–744, 2015.

[37] D. Fraga, E. Barrachina, I. Calvet, T. S. Stoyanova Lyubenova, and J. B. Carda, “Developing CIGS solar cells on glass-ceramic substrates,” *Mater. Lett.*, vol. 221, no. March, pp. 104–106, 2018.

[38] T. Alzoubi and M. Moustafa, “Numerical optimization of absorber and CdS buffer layers in CIGS solar cells using SCAPS,” *Int. J. Smart Grid Clean Energy*, vol. 8, no. 3, pp. 291–298, 2019.

[39] S. Royanian, A. Abdolahzadeh Ziabari, and R. Yousefi, “Efficiency Enhancement of Ultra-thin CIGS Solar Cells Using Bandgap Grading and Embedding Au Plasmonic Nanoparticles,” *Plasmonics*, vol. 15, no. 4, pp. 1173–1182, 2020.

[40] M. Yamaguchi, “III–V compound multi-junction solar cells: present and future,” *Sol. energy Mater. Sol. cells*, vol. 75, no. 1–2, pp. 261–269, 2003.

[41] R. R. King *et al.*, “40% efficient metamorphic GaInPGaInAsGe multijunction solar cells,” *Appl. Phys. Lett.*, vol. 90, no. 18, pp. 90–93, 2007.

[42] A. C. Varonides, “High Efficiency Multijunction Tandem Solar Cells with Embedded Short-Period Superlattices,” *Proc. World Renew. Energy Congr. – Sweden, 8–13 May, 2011, Linköping, Sweden*, vol. 57, no. 570, pp. 2767–2773, 2011.

[43] K. Sasaki, T. Agui, K. Nakaido, N. Takahashi, R. Onitsuka, and T. Takamoto, “Development Of InGaP/GaAs/InGaAs inverted triple junction concentrator solar cells,” *AIP Conf. Proc.*, vol. 1556, no. September, pp. 22–25, 2013.

[44] R. Cheriton *et al.*, “Design optimizations of InGaAsN(Sb) subcells for concentrator photovoltaic systems,” *J. Vac. Sci. Technol. B, Nanotechnol. Microelectron. Mater. Process. Meas. Phenom.*, vol. 34, no. 2, p. 02M103, 2016.

[45] O. Saif, M. Abouelatta, A. Shaker, and M. K. Elsaid, “On the optimization of InGaP/GaAs/InGaAs triple-junction solar cell,” *IOP Conf. Ser. Mater. Sci. Eng.*, vol. 446, no. 1, 2018.

[46] M. Moustafa and T. Alzoubi, “Numerical simulation of single junction ingan solar cell by scaps,” *Key Eng. Mater.*, vol. 821 KEM, pp. 407–413, 2019.

[47] R. S. Ohl, “Light-sensitive electric device,” *United States Pat. Off.*

2402662, pp. 1–14, 1941.

[48] T. H. European, P. Solar, and E. Conference, “10Th European Photovoltaic Solar Energy Conference &-12 April 1991 Lisbon, Portugal,” no. April, pp. 270–272, 1991.

[49] H. Savin *et al.*, “Black silicon solar cells with interdigitated back-contacts achieve 22.1% efficiency,” *Nat. Nanotechnol.*, vol. 10, no. 7, pp. 624–628, 2015.

[50] K. Yoshikawa *et al.*, “Silicon heterojunction solar cell with interdigitated back contacts for a photoconversion efficiency over 26%,” *Nat. energy*, vol. 2, no. 5, p. 17032, 2017.

[51] D. M. Callahan, J. N. Munday, and H. A. Atwater, “Solar cell light trapping beyond the ray optic limit,” *Nano Lett.*, vol. 12, no. 1, pp. 214–218, 2012.

[52] H. Heidarzadeh, M. Dolatyari, G. Rostami, and A. Rostami, “Modeling of solar cell efficiency improvement using pyramid grating in single junction silicon solar cell,” in *2nd International Congress on Energy Efficiency and Energy Related Materials (ENEFM2014)*, 2015, pp. 61–67.

[53] R. R. Khan, F. M. Chowdhury, M. D. Subramanyam, and S. W. Thomas, “Performance comparison of plasmonic solar cell employing aluminum and silver nano particles,” in *2017 IEEE 17th International Conference on Nanotechnology (IEEE-NANO)*, 2017, pp. 526–530.

[54] J.-C. Lin, W.-J. Ho, C.-W. Yeh, J.-J. Liu, H.-J. Syu, and C.-F. Lin, “Light trapping of plasmonics textured silicon solar cells based on broadband light scattering and wide acceptance angle of indium nanoparticles,” in *2017 International Conference on Applied System Innovation (ICASI)*, 2017, pp. 118–121.

[55] M. Liu, M. B. Johnston, and H. J. Snaith, “Efficient planar

heterojunction perovskite solar cells by vapour deposition," *Nature*, vol. 501, no. 7467, pp. 395–398, 2013.

[56] H. Heidarzadeh and F. Mehrfar, "Effect of size non-uniformity on performance of a plasmonic perovskite solar cell: an array of embedded plasmonic nanoparticles with the Gaussian distribution radiuses," *Plasmonics*, vol. 13, no. 6, pp. 2305–2312, 2018.

[57] P. Taylor, G. Ferro, and G. Ferro, "Critical Reviews in Solid State and Materials Sciences 3C-SiC Heteroepitaxial Growth on Silicon : The Quest for Holy Grail 3C-SiC Heteroepitaxial Growth on Silicon : The Quest for Holy Grail," no. February, pp. 37–41, 2015.

[58] G. L. Harris, *Properties of silicon carbide*, no. 13. Iet, 1995.

[59] B. S. Richards *et al.*, "3C-SiC as a future photovoltaic material," in *3rd World Conference onPhotovoltaic Energy Conversion, 2003. Proceedings of*, 2003, vol. 3, pp. 2738–2741.

[60] Y. Dou *et al.*, "Structural stability, electronic and optical properties of Ni-doped 3C-SiC by first principles calculation," *J. Alloys Compd.*, vol. 509, no. 20, pp. 6117–6122, 2011.

[61] H. Heidarzadeh, H. Baghban, H. Rasooli, M. Dolatyari, and A. Rostami, "A new proposal for Si tandem solar cell: Significant efficiency enhancement in 3C-SiC/Si," *Optik (Stuttg).*, vol. 125, no. 3, pp. 1292–1296, 2014.

[62] M. Toure *et al.*, "New 3C Silicon Carbide on Silicon Hetero-Junction Solar Cells for UV Collection enhancement," in *MRS Proceedings*, 2014, vol. 1693.

[63] P. L. Zhou, S. K. Zheng, L. Ma, J. He, Y. Tian, and R. Shi, "Electronic and optical properties of Co-doped 3C-SiC from density functional calculations," *Solid State Commun.*, vol. 196, pp. 28–31, 2014.

[64] M. Eskandari, H. Heidarzadeh, A. Rostami, G. Rostami, and M.

Dolatyari, “A Proposal for Intermediate Band Solar Cells with Optimized Transition Energy in Cr Doped 3C-SiC,” 2015, pp. 69–76.

[65] J. W. Sun *et al.*, “Solar driven energy conversion applications based on 3C-SiC,” *Mater. Sci. Forum*, vol. 858, pp. 1028–1031, 2016.

[66] H. Zerfaoui, D. Dib, and B. Kadem, “The Simulated Effects of Different Light Intensities on the SiC-Based Solar Cells,” *Silicon*, vol. 11, no. 4, pp. 1917–1923, 2019.

[67] H. Heidarzadeh, “Transition metal-doped 3C-SiC as a promising material for intermediate band solar cells,” *Opt. Quantum Electron.*, vol. 51, no. 1, pp. 1–11, 2019.

[68] H. Heidarzadeh, “Performance analysis of cubic silicon carbide solar cell as an appropriate candidate for high temperature application,” *Opt. Quantum Electron.*, vol. 52, no. 4, pp. 1–11, 2020.

[69] N. Alhuda and Q. Algwari, “Simulation and optimization of a thin film 3C-SiC solar cell using SCAPS,” no. October, 2020.

[70] N. Jain, “Design of Iii-V Multijunction Solar Cells on Silicon Substrate,” p. 70, 2013.

[71] A. Zekry, “A course on photo-voltaic array systems,” *Princ. Analaysis Des. PV Syst.*, no. January 1996, 2017.

[72] M. Boxwell, “Solar Electricity Handbook-2012 Edition: A Simple Practical Guide to Solar Energy-Designing and Installing Photovoltaic Solar Electric Systems,” *Warwickshire, Engl. Greenstream*, 2012.

[73] S. Bapanapalli, “Cds / cdte thin film solar cells with zinc stannate buffer layer,” 2005.

[74] K. S. Rida, A. A. K. Al-waeli, and K. A. H. Al-asadi, “The impact of air mass on photovoltaic panel performance,” *Pisco Med Publ.*,

vol. 1, no. December, pp. 1–9, 2016.

[75] H. A. Kazem and M. T. Chaichan, “The Impact of Using Solar Colored Filters to Cover the PV Panel in Its Outcomes,” *Sch. Bull.*, vol. 2, no. 7, pp. 464–469, 2016.

[76] Y. H. Khattak, “Modeling of High Power Conversion Efficiency Thin Film Solar Cells,” 2019.

[77] S. M. Sze and K. K. Ng, *Physics of semiconductor devices*. John wiley & sons, 2006.

[78] A. R. Anggraini and J. Oliver, *Integrated Silicon Optoelectronics*, vol. 53, no. 9. 2019.

[79] J.-P. Colinge and C. A. Colinge, *Physics of semiconductor devices*. Springer Science & Business Media, 2005.

[80] A. McEvoy, T. Markvart, and L. Castaner, *Practical Handbook of Photovoltaics - Fundamentals and Applications (2012)*. 2012.

[81] G. E. Jellison and P. C. Joshi, *Crystalline silicon solar cells*, vol. 212. 2018.

[82] PeterWürfel and UliWürfel, *Physics of Solar Cells: from basic principles to advanced concepts. John Wiley & Sons*, no. 1. 2016.

[83] Emmanuel Rosencher and Borge Vinter, *Optoelectronics”, English Edition Cambridge University Press*, no. 1. .

[84] M. A. Parker, *Solid State and Quantum Theory for Optoelectronics*. 2009.

[85] F. Baig, “Numerical Analysis for Efficiency Enhancement of Thin Film Solar Cells,” 1999.

[86] A. Laurent, “Modelling and analysis of multi-junction photovoltaic cells using MATLAB / Simulink for the improvement of conversion efficiency . A dissertation submitted by,” 2016.

[87] M. A. Green and H. Cui, “Molybdenum Back Contact Treatment for Cu 2 ZnSnS 4 Solar Cells By Supervised by,” 2015.

[88] S. Irvine, “Solar Cells and Photovoltaics BT - Springer Handbook of Electronic and Photonic Materials,” S. Kasap and P. Capper, Eds. Cham: Springer International Publishing, 2017, p. 1.

[89] S. B. Naredla, “Electrical properties of molybdenum silicon carbide Schottky barrier diodes.” 2019.

[90] A. Elasser, T. P. Chow, and S. Member, “Silicon Carbide Benefits and Advantages for Power Electronics Circuits and Systems,” vol. 90, no. 6, pp. 969–986, 2002.

[91] X. Lu, T. Zhao, Q. Lei, X. Yan, J. Ren, and P. La, “Effects of co-doping on electronic structure and optical properties of 3C-SiC from first-principles method,” *Comput. Mater. Sci.*, vol. 170, no. February, p. 109172, 2019.

[92] B. Parida, J. Choi, G. Lim, K. Kim, and K. Kim, “Enhanced visible light absorption by 3C-SiC nanoparticles embedded in Si solar cells by plasma-enhanced chemical vapor deposition,” *J. Nanomater.*, vol. 2013, 2013.

[93] D. Feng *et al.*, “Catalytic Synthesis and Photoluminescence of Needle-Shaped 3C–SiC Nanowires,” *Solid State Commun.*, vol. 128, pp. 295–297, Nov. 2003.

[94] A. Arvanitopoulos, N. Lophitis, K. N. Gyftakis, S. Perkins, and M. Antoniou, “Validated physical models and parameters of bulk 3C-SiC aiming for credible technology computer aided design (TCAD) simulation,” *Semicond. Sci. Technol.*, vol. 32, no. 10, 2017.

[95] Z.-M. Li *et al.*, “First principles calculation of electronic structure for Al-doped 3C-SiC and its microwave dielectric properties,” *Acta Phys. Sin.*, vol. 61, no. 23, p. 237103, 2012.

[96] S. Greulich-Weber, M. Zöller, and B. Friedel, “Textile solar cells based on SiC microwires,” *Mater. Sci. Forum*, vol. 615 617, no. January 2009, pp. 239–242, 2009.

[97] Y. K. Dou, X. Qi, H. B. Jin, M. S. Cao, U. Zahid, and Z. L. Hou, "First principle study of the electronic properties of 3C-SiC doped with different amounts of Ni," *Chinese Phys. Lett.*, vol. 29, no. 7, 2012.

[98] A. A. El-Amin, "Study of the Electrical Properties and the Internal Quantum Efficiency of SnO2-p/n- Si Thin Film Solar Cells," *Silicon*, vol. 9, no. 1, pp. 47–51, 2017.

[99] F. Trani, M. Causà, D. Ninno, G. Cantele, and V. Barone, "Density functional study of oxygen vacancies at the SnO2 surface and subsurface sites," *Phys. Rev. B - Condens. Matter Mater. Phys.*, vol. 77, no. 24, 2008.

[100] H. Zerfaoui, D. Dib, M. Rahmani, K. Benyelloul, and C. Mebarkia, "Study by simulation of the SnO2 and ZnO anti-reflection layers in n-SiC/p-SiC solar cells," *AIP Conf. Proc.*, vol. 1758, 2016.

[101] M. I. Kabir, S. A. Shahahmadi, V. Lim, S. Zaidi, K. Sopian, and N. Amin, "Amorphous silicon single-junction thin-film solar cell exceeding 10 % efficiency by design optimization," *Int. J. Photoenergy*, vol. 2012, no. November, 2012.

[102] C. Cds, Z. M. Thin, and F. Solar, "Effect of Absorber Layer Thickness and Band Gap on the Performance of Effect of Absorber Layer Thickness and Band Gap on the Performance of CdTe / CdS / ZnO Multi-Junction Thin Film Solar Cell," no. July, 2018.

[103] S. Enayati Maklavani and S. Mohammadnejad, "The impact of the carrier concentration and recombination current Enayati Maklavani, S., & Mohammadnejad, S. (2020). The impact of the carrier concentration and recombination current on the p+pn CZTS thin film solar cells. Optical and Quantum Electronics," *Opt. Quantum Electron.*, vol. 52, no. 6, 2020.

[104] W. Fang *et al.*, "The ideal doping concentration of silicon wafer for

single junction hybrid n-Si /PEDOT: PSS solar cells with 3.2% elevated PCE and V oc of 620 mV," *J. Mater. Sci. Mater. Electron.*, vol. 31, no. 8, pp. 6398–6405, 2020.

[105] M. Wolf, "The influence of heavy doping effects on silicon solar cell performance," *Sol. Cells*, vol. 17, no. 1, pp. 53–63, 1986.

[106] M. Salem, A. Zekry, A. Shaker, M. Abouelatta-Ebrahim, and T. Abdolkader, "Performance Enhancement of a Proposed Solar Cell Microstructure Based on Heavily Doped Silicon Wafers," *Semicond. Sci. Technol.*, vol. 34, Jan. 2019.

[107] E. Technology, "OPTIMIZATION OF MONOCLINIC Cu 2 SnS 3 (CTS) THIN FILM SOLAR CELL PERFORMANCES THROUGH NUMERICAL ANALYSIS Department of Electrical and Electronic Engineering , Dhaka University of," vol. 17, no. 2, pp. 85–98, 2020.

[108] N. Khoshsirat, N. A. Md Yunus, M. N. Hamidon, S. Shafie, and N. Amin, "Analysis of absorber layer properties effect on CIGS solar cell performance using SCAPS," *Optik (Stuttg).*, vol. 126, no. 7–8, pp. 681–686, 2015.

[109] A. Fantoni, M. Vieira, and R. Martins, "Simulation of hydrogenated amorphous and microcrystalline silicon optoelectronic devices," *Math. Comput. Simul.*, vol. 49, no. 4–5, pp. 381–401, 1999.

[110] G. A. Landis, D. Merritt, R. P. Raffaelle, and D. Scheiman, "High-temperature solar cell development," 2005.

[111] M. Chegaar, A. Hamzaoui, A. Namoda, P. Petit, M. Aillerie, and A. Herguth, "Effect of illumination intensity on solar cells parameters," *Energy Procedia*, vol. 36, no. November 2018, pp. 722–729, 2013.

[112] F. Khan, S. N. Singh, and M. Husain, "Effect of illumination intensity on cell parameters of a silicon solar cell," *Sol. Energy*

Mater. Sol. Cells, vol. 94, no. 9, pp. 1473–1476, 2010.

[113] M. Wolf and H. Rauschenbach, "Series resistance effects on solar cell measurements," *Adv. Energy Convers.*, vol. 3, no. 2, pp. 455–479, 1963.

[114] L. Et-taya, T. Ouslimane, and A. Benami, "Numerical analysis of earth-abundant Cu2ZnSn(SxSe1-x)4 solar cells based on Spectroscopic Ellipsometry results by using SCAPS-1D," *Sol. Energy*, vol. 201, no. November 2019, pp. 827–835, 2020.

[115] H. Heriche, Z. Rouabah, and N. Bouarissa, "New ultra thin CIGS structure solar cells using SCAPS simulation program," *Int. J. Hydrogen Energy*, vol. 42, no. 15, pp. 9524–9532, 2017.

[116] D. M. Tobnaghi, R. Madatov, and P. Farhadi, "Investigation of light intensity and temperature dependency of solar cells electric parameters," *Electr. Power Eng. Contol Syst. 2013*, no. November, pp. 90–93, 2013.

[117] P. Singh and N. M. Ravindra, "Solar Energy Materials & Solar Cells Temperature dependence of solar cell performance — an analysis," *Sol. Energy Mater. Sol. Cells*, vol. 101, pp. 36–45, 2012.

[118] G. E. Bunea, K. E. Wilson, Y. Meydbray, M. P. Campbell, and D. M. De Ceuster, "Low light performance of mono-crystalline silicon solar cells," *Conf. Rec. 2006 IEEE 4th World Conf. Photovolt. Energy Conversion, WCPEC-4*, vol. 2, pp. 1312–1314, 2006.

[119] A. Liquide and M. Systems, "Temperature dependence pf of the Eg in semiconductors," vol. 30328, no. July, pp. 1–17, 2016.

[120] A. Manoogian and J. C. Woolley, "Temperature Dependence of the Energy Gap in Semiconductors.," *Can. J. Phys.*, vol. 62, no. 3, pp. 285–287, 1984.

[121] P. Singh, S. N. Singh, M. Lal, and M. Husain, "Solar Energy Materials & Solar Cells Temperature dependence of I – V

characteristics and performance parameters of silicon solar cell," vol. 92, pp. 1611–1616, 2008.

[122] S. Design, "The Spectral p-n Junction Model for Tandem," no. 2, 1987.

الخلاصة

في هذه الدراسة، تم إجراء تحليل محدد على خلايا شمسية رقيقه نوع PIN 3C-SiC. تتكون هذه الخلية من الطبقة الماصة والتي هي عباره عن مادة 3C-SiC مشوبة بالألمنيوم لغرض الحصول على شبه موصل بمواصفات نوع p وبفجوة طاقة تبلغ 1.454 الكترون فولت، وطبقة نقية غير مشوبة من مادة 3C-SiC بفجوة طاقة 2.39 الكترون فولت. وكذلك شريحة مزدوجة تتكون من طبقتين من نوع n، طبقة من مادة 3C-SiC نوع n بفجوة طاقة 2.39 الكترون فولت وطبقه 3C-SiC مشوبة بالكروم لغرض الحصول على شبه موصل بمواصفات نوع n وبفجوة طاقة 1.139 الكترون فولت، وطبقة SnO_2 تعمل كنافذة لدخول الضوء وهي مادة مضادة للانعكاس وبفجوة طاقة 3.6 الكترون فولت.

تمت الدراسة باستخدام برنامج المحاكاة الحاسوبية SCAPS-1D. والذي تم تصميمه لمحاكاة ودراسة خصائص الخلايا الشمسية الرقيقة.

تم إجراء دراسة تحديديه على الخلية المرجعية، والتي تعتمد على القيم الأولية لمعلمات الخلية (كثافة المنشطات وسمكها) لكل طبقة من الخلية. وكانت القيم الأولية لتركيز حاملات الشحنة كالتالي: لطبقة p-Al (3C-SiC) كانت $N_a = 10^{13}$ سم$^{-3}$، ولطبقة n-Cr (3C-SiC) كانت $N_d = 10^{13}$ سم$^{-3}$، ولطبقة n^+(3C-SiC) كانت $N_d = 10^{19}$ سم$^{-3}$، وبالنسبة لطبقة n- (SnO_2) كانت $N_d = 10^{12}$ سم$^{-3}$، اما طبقة (3C-SiC) النقية فكان تركيز حاملات الشحنة الاولي لها هو 10^{10} سم$^{-3}$. قيم السمك الأولي هو (1، 1، 0.05، 0.05، و 0.1 مايكرومتر) للطبقات: p-Al (3C-SiC)، i- (3C-SiC)، n-Cr (3C-SiC)، n^+ (3C-SiC) و n- (SnO_2) على التوالي. وكانت معلمات الإخراج للخلية المرجعية: (V_{OC}=0.2524 فولت، J_{SC} =34.66 مللي أمبير.سم $^{-2}$، FF= 41.21٪ و كفاءه= 3.61٪).

تم دراسة تأثير تركيز حاملات الشحنة لكل طبقة على أداء الخلية المرجعية. تم إثبات أن كفاءة الخلية المرجعية زادت من 0.87 إلى 18.73٪ عندما تغيرت كثافة الحاملات للطبقة الماصة من 10^{10} إلى 10^{15} سم $^{-3}$، كما وازدادت كفاءة الخلية من 16.84 إلى 21.52٪ مع زيادة تركيز الحاملات في طبقة n^+ من 10^{18} إلى 10^{22} سم $^{-3}$. ومن ناحية أخرى، فإن زيادة تركيز الحاملات في الطبقة العازلة n-Cr (3C-SiC) من 10^{13} إلى 10^{15} سم $^{-3}$ لا يؤثر على كفاءة الخلية، وذلك بسبب عمليات إعادة الاتحاد الشديدة والتي تحدث نتيجة لكون تركيز المانح في الطبقة العازلة اقل من تركيز القابل في طبقة الامتصاص وبالتالي، تم إجراء زيادة إضافية في كثافة الحاملات في هذه الطبقة حتى 10^{19} سم $^{-3}$ والذي أدى الى زيادة كفاءة الخلية من 21.44 إلى 22.69٪. تغيير تركيز حاملات الشحنة في طبقة i- (3C-SiC) وطبقة SnO_2 ليس له تأثير كبير على أداء الخلية والتركيز الأمثل لحاملات الشحنة في طبقة i- (3C-SiC) هو 10^{15} سم $^{-3}$ وبالنسبة لـ SnO_2 هو $N_d = 10^{18}$ سم $^{-3}$ واللذان ينتجان كفاءة تحويل بنسبة 22.78٪.

تم إجراء الجزء الثاني من الدراسة على سمك كافة طبقات الخلية الشمسية حيث تم تغيير سمك طبقة الامتصاص من 1 إلى 3 مايكرومتر وأدى هذا الى زيادة بالكفاءة من 22.78 إلى 24.14٪، والذي نتج بسبب زيادة جمع حاملات الشحنة المتولدة ضوئيا قبل حدوث عملية إعادة الاتحاد لها. تم تغيير سمك الطبقة النقية من 1 إلى 2.5 مايكرومتر والذي أدى الى زيادة في كفاءة الخلية من 24.14 إلى 34.45٪، وهذا يوضح الدور الهام لسمك الطبقة النقية في أداء الخلية. زيادة سمك طبقة النافذة من 0.1 إلى 0.2 مايكرومتر يقلل من كفاءة الخلية من 34.45 إلى 31.93٪، كما وأن زيادة سمك الطبقة n^+ من 0.05 إلى 0.1 مايكرومتر يقلل الكفاءة من 31.93 إلى 30.32٪. ومع ذلك، فإن زيادة سمك هذه الطبقات له تأثير مفيد في تقليل القيمة العالية لتيار الدائرة القصيرة للخلية من 54.27 إلى 47.69 مللي أمبير. سم$^{-2}$. ومن ناحية أخرى، لا يؤثر تغيير سمك طبقة n-Cr (3C-SiC) بشكل ملحوظ على أداء الخلية. وبالتالي فإن أخذ طبقة رقيقة (100 نانومتر) هو الأفضل لتقليل مقاومة الخلية، والذي ينتج كفاءة تحويل طاقة تبلغ 30.27٪.

كما وتناولت الدراسة الحالية تأثير الظروف البيئية الرئيسية (الإضاءة ودرجة الحرارة) على هيكل الخلية الأمثل. حيث ثبت أن التيار الناتج من الخلايا الكهروضوئية يتناسب بشكل مباشر مع الإضاءة، مع زيادة شدة الضوء من 250 إلى 1200 وات. م$^{-2}$، يزداد تيار الدائرة القصيرة J_{SC} من 11.924 إلى 57.149 مللي أمبير. سم$^{-2}$ وذلك بسبب الزيادة الحاصلة في امتصاص الفوتونات والذي بدوره يؤدي الى زيادة توليد حاملات الشحنة وبالتالي زيادة تيارJ_{SC}. كذلك وقد لوحظ انخفاض كفاءة الخلية مع ارتفاع شدة الإضاءة للقيم التي أكبر من 500 وات. متر$^{-2}$ من 30.34 إلى 30.20٪ نتيجة لتأثير مقاومة السلسلة العالية R_S.

تمت دراسة تأثير درجة الحرارة على الخلية المثلى، ووجد أنه كلما زادت درجة الحرارة من 300 إلى 400 كلفن، ينخفض جهد الدائرة المفتوحة V_{OC} من 0.768 إلى 0.516 فولت، مما يؤدي إلى انخفاض كفاءة الخلية من 30.27 إلى 18.10 ٪. تنخفض قيمة V_{OC} بشكل كبير بسبب انخفاض تيار التشبع I_0 الذي يقل بشكل مباشر مع زيادة درجة الحرارة.

تمت مناقشة النتائج بعد الحصول عليها وإعطاء الاستنتاجات وتقديم الاقتراحات المستقبلية لمزيد من العمل في هذا المجال.

جـامعـة نينوى
كلية هندسة الالكترونيات
قسم الالكترونيك

النمذجة والوصف الكهربائي للخلايا الشمسية المتراكبة

نور الهدى سعد عباس الجماس

رسالة في هندسة الالكترونيك

(الحالة الصلبة)

بإشراف

الدكتور قيس ذنون الجواري

1442 هـ 2020م

النمذجة والوصف الكهربائي للخلايا الشمسية المتراكبة

رسالة تقدمت بها

نور الهدى سعد عباس الجماس

إلى

مجلس كلية هندسة الالكترونيات -جامعة نينوى
وهي جزء من متطلبات نيل شهادة الماجستير
علوم في هندسة الالكترونيك
(الحالة الصلبة)

بإشراف

الدكتور قيس ذنون الجواري

1442هـ 2020م